The Gas System for the HERMES Transition Radiation Detector

by

Douglas Michael Thiessen

B.Sc., University of British Columbia, 1993

A THESIS SUBMITTED IN PARTIAL FULFILLMENT
OF THE REQUIREMENTS FOR THE DEGREE OF
MASTER OF SCIENCE
in the Department
of
Physics

SIMON FRASER UNIVERSITY
March 1996

APPROVAL

Name: Douglas Michael Thiessen

Degree: Master of Science

Title of thesis: The Gas System for the HERMES Transition Radiation Detector

Examining Committee: Prof. J.C. Irwin
Chair

Dr. Michel Vetterli
Senior Supervisor

Prof. Jeff Dahn
Dept. of Physics, S.F.U.

Prof. John D'Auria
Dept. of Chemistry, S.F.U.

Dr. Simon Watkins
Internal Examiner
Assistant Professor, Dept. of Physics, S.F.U.

Date Approved:

Abstract

The HERMES experiment measures deep inelastic scattering of polarised positrons from polarised nucleons to study the spin structure of the proton and the neutron. A unique feature of HERMES is the ability to measure hadrons (pions, protons, etc.) in coincidence with the scattered positron, allowing for analysis of different components of the spin structure. Due to the high level of hadronic background from photoproduction, particle identification is crucial to HERMES.

The transition radiation detector forms an integral component of the particle identification system. Positrons are identified using the fact that they are highly relativistic and produce transition radiation while the hadrons do not. In order for the detector to distinguish efficiently between the signals from both particles, its gain must remain stable. The gain is very sensitive to changes in the properties of the detector gas. If the differential pressure across the cathode foils changes by 10 μbar, or the composition of the gas mixture changes by 0.2%, the gain shifts by 1%. Therefore, a sophisticated control system was designed to minimize fluctuations in the gas characteristics. This system performs to its specifications, and the gain of the detector is stable enough to achieve the required particle identification.

Acknowledgements

First of all, I'd like to thank my supervisor, Mike Vetterli, for his patience and guidance during this thesis.

I would also like to extend my appreciation to Martin Kueckes, Robert Openshaw, Marielle Goyette, John Schaapman, and Len Wampler for building the gas system. In particular, I would like to thank Robert Openshaw for his assistance and advice throughout my work on this project.

I owe a great deal to Ralf Kaiser who has been both a friend and an advisor. He has helped me out in numerous areas as well as providing support to keep me on track.

I also want to thank my wife, Lori. She has provided the behind the scenes support that was necessary for my successful completion.

Contents

List of Tables

List of Figures

Chapter 1

Introduction

Since the beginning of this century, scattering experiments have provided information regarding the structure of matter. In 1911, Rutherford postulated the existence of the nucleus of the atom to explain the results of Geiger and Marsden's experiment in which 5 MeV α particles were scattered from a gold foil.[1] The seemingly anomalous angular distribution of the scattered α particles gave evidence of the substructure of the atom. With the development of particle accelerators, higher energy particles were employed to further probe the structure of matter. As the energy of the incoming particle increases, it can be used to probe more deeply. In 1969, experiments were conducted at SLAC using 20 GeV electrons scattered from protons.[2] Analogous to the gold foil experiment, the results indicated that there is a sub-structure to the proton. These subparticles were called partons. They were later identified to be the spin $\frac{1}{2}$ quarks postulated by Gell-Mann and Zweig.[3] The basic model, known as the quark parton model, of the proton and the neutron (collectively known as the nucleon) is that they are made up of three quarks. Because of the high energy of the incoming electrons, they interact directly with the quarks in the nucleon. The large momentum transferred to the struck quark causes the nucleon to break up. This type of scattering is known as deep inelastic scattering (DIS). The structure functions of the nucleon, F_1 and F_2 are a description of the quark momentum distributions in the nucleon. Both the quarks and the nucleons are spin $\frac{1}{2}$ particles. Because the nucleon is made up of quarks, one would assume that the spin of the quarks would combine to produce the spin of the nucleon. The spin structure functions g_1 and g_2 describe the distribution of the quark spins within the nucleon. The nucleon structure functions will be described in chapter 2.

Recent experiments have shown that the contribution of the quarks to the nucleon spin is only a small fraction of the total.[4−7] This surprising result showed a lack of understanding regarding the nature of the nucleon spin, and was labelled the 'spin-crisis'. Due to later improvements in both the theory and the data, this term has been dropped, but the spin structure is still not well understood. Interpretation of the unpolarized structure functions $F_{1,2}$ reveals that the structure of the nucleon consists not only of the 3 quarks, known as valence quarks, but also interacting gluons and quark-antiquark pairs. The $q\overline{q}$ pairs are spontaneously created and annihilated and are referred to as the quark sea. Given that the quarks contribute only a fraction of the nucleon spin, most of the spin must come from sea quarks at low x, gluons or orbital angular momentum.

The HERMES experiment is a deep inelastic scattering experiment of polarised positrons[1] from polarised nucleons which investigates the spin structure of the nucleon. The HERMES collaboration consists of about 200 physicists from 10 countries, and it utilizes the HERA electron storage ring at the DESY laboratory in Hamburg, Germany. The experiment involves scattering polarised 27.5 GeV positrons from polarised gas targets of hydrogen, deuterium, or ^{3}He. The scattered particles are measured by the large acceptance HERMES spectrometer which is also capable of identifying outgoing positrons and pions. The HERMES experiment provides an accurate measurement of the spin structure functions for both the proton and the neutron, and it provides semi-inclusive hadron measurements which are made by identifying outgoing hadrons in coincidence with the electrons. This enables HERMES

[1]At the energy used in HERMES, the cross sections for e^+p and e^-p are equal. HERA was originally designed to be an electron/proton collider, but to improve the beam lifetime, the electron beam was switched to positrons in 1995. For these reasons, electrons and positrons will be used interchangeably in this thesis.

to decompose the spin structure into contributions from the valence and sea quarks. HERMES is currently the only experiment that can make this distinction.

In order to measure the semi-inclusive events, HERMES must be able to identify efficiently the outgoing particles; also, due to a large hadronic background, it must strongly distinguish between the positrons and hadrons for all measurements. One of the main components in the particle identification system is the transition radiation detector (TRD). It was developed and built at TRIUMF by the Canadian part of the HERMES collaboration. Transition radiation is produced when an ultrarelativistic particle crosses the boundary between differing dielectric media and is dependent on the relativistic γ factor of the particle. Because of the sensitivity to $\gamma = E/mc^2$ instead of the velocity, β, this detector gives much more efficient particle identification at high energy than a Cerenkov detector which uses a β threshold. Since the β of a 5 GeV pion and electron are both virtually 1 (0.9996 and 0.999999995 respectively), the electron would be only slightly above the threshold of the Cerenkov detector, and it would produce very few photons per metre. Thus, the detector would have to be very long in order for the electron to produce an effective signal. With a TRD, because the γ of an electron is approximately 270 times greater than for a pion at the same energy, only the electron radiates at HERMES energies. However, in order to measure accurately the energy deposited in the TRD, the gain of the detector must remain constant. A number of factors can affect the gain of the TRD; these will be discussed in Chapter 4.

The characteristics of the gas in the detector have a very significant effect on the gain. The composition of the gas must be held extremely constant. This includes maintaining the gas at a constant mixture and keeping it free of even minute impurities. Also, the differential pressure at the cathode windows of the detector must be held constant to less than one part in 10^5 in order to keep the window position stable to within 0.01 mm which results in a 1% gain stability.[8] The primary gas used in the detector is Xe because the high Z gas absorbs X-rays well. However, because Xe is a very expensive gas, it has to be recirculated. This leads to the need for effective purification of the gas in the system. Because of these requirements, the gas control system for the HERMES TRD is very complicated.

Chapter 2 will discuss the physics of deep inelastic scattering and will present data that led to the spin crisis and the motivation for the HERMES experiment. In Chapter 3, the HERMES detector will be described; this will include details of the HERMES spectrometer and the particle identification system. Chapter 4 deals specifically with the TRD. It will discuss the physics of transition radiation detectors and give details on the specific requirements of the HERMES TRD. Chapter 5 is devoted to the gas system for the HERMES TRD. The technical details of the system are described in this chapter as well as the physics behind the operation of the sub-systems. Also presented in this chapter are the data from the commissioning of the system which demonstrate that the requirements for gain stability have been achieved.

Chapter 2

HERMES Physics

Deep inelastic scattering is a powerful tool for studying the structure of the nucleon. The de Broglie wavelength of the high energy incoming lepton is small enough to be sensitive to structures smaller than the nucleon, and the interaction is actually an elastic collision with its constituents, known as partons. The high momentum transfer in the collision causes the struck parton to exit the nucleon. Quark confinement results in the formation of new hadrons from the scattered parton and the nucleon remnant. By studying the scattered particles, much information about the structure of the nucleon is obtained.

2.1 Unpolarised Structure Functions

For a more thorough derivation of structure functions, refer to references [9–12]. Figure 2.1 shows a Feynman diagram of a DIS event. The measurable quantities in inclusive scattering are the initial and final 4-momentum of the electron, $k = (E, \vec{k})$

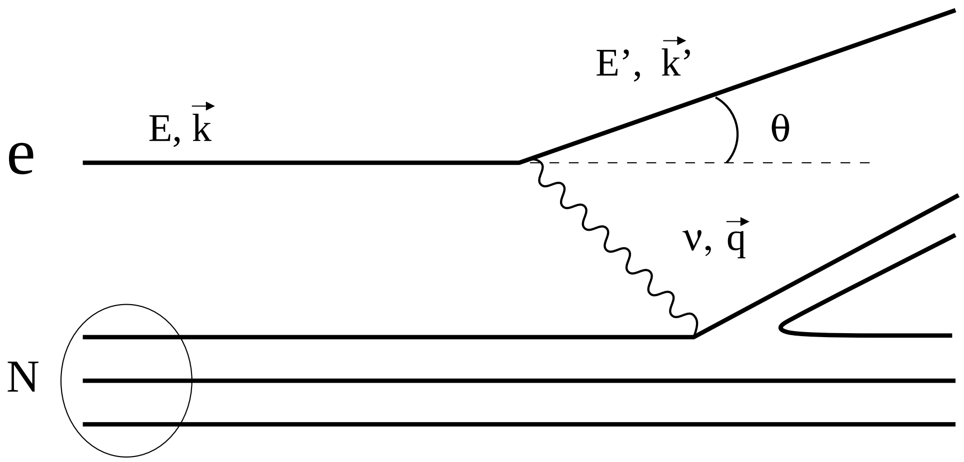

Figure 2.1: Feynman diagram of a deep inelastic scattering event.

and $k' = (E', \vec{k}')$ respectively. The 4-momentum transfer $q = (\nu, \vec{q})$ is obtained from

$$\nu = E - E' \tag{2.1}$$

$$\vec{q} = \vec{k} - \vec{k}' \tag{2.2}$$

$$Q^2 = -q^2 = 4EE' \sin\frac{\theta}{2}. \tag{2.3}$$

In the case of inelastic lepton-nucleon scattering where the internal components of the nucleon become excited, the cross section can be written in a general form without any knowledge of the internal structure of the nucleon. This is achieved by parameterizing the cross section with five unknown functions using combinations of the kinematic parameters. Of these five, one can be eliminated in electron scattering through parity conservation. The remaining four can be reduced to two independent functions of ν and Q^2 because of current conservation at the hadronic vertex. The DIS cross section, σ, in the lab frame is given by

$$\frac{d^2\sigma}{dE'\,d\Omega} = \left[\frac{2E'\alpha}{Q^2 \sin\frac{\theta}{2}}\right]^2 \left\{2W_1(\nu, Q^2)\sin^2\frac{\theta}{2} + W_2(\nu, Q^2)\cos^2\frac{\theta}{2}\right\} \tag{2.4}$$

where α is the fine structure constant, Ω is the solid angle, and W_1 and W_2 are called structure functions.

If the partons are simple, point-like, spin-$\frac{1}{2}$ particles (quarks), the cross section can be simplified at high Q^2. This is due to the fact that the inelastic lepton-nucleon scattering becomes an elastic collision of the lepton on a "free" quark within the nucleon. Because of this, the structure functions can be simplified such that the cross section becomes that of a collision between two free Dirac particles, and the structure functions do not depend on ν and Q^2 independently:

$$MW_1(\nu, Q^2) \implies F_1(x) \tag{2.5}$$

$$\nu W_2(\nu, Q^2) \implies F_2(x). \tag{2.6}$$

The new structure functions, F_1 and F_2 depend only on the single, dimensionless variable

$$x = \frac{Q^2}{2M\nu} \tag{2.7}$$

where M is the mass of the nucleon. This dependence only on x and not Q^2 and ν separately is known as Bjorken scaling. The two variables, x and

$$y = \frac{\nu}{E} \tag{2.8}$$

are referred to as the Bjorken scaling variables. Also stemming from the association of the partons with spin $\frac{1}{2}$ particles is the Callen-Gross relation:

$$F_2(x) = 2xF_1(x). \tag{2.9}$$

In the Breit, or infinite momentum frame, x is the same as the fraction of the nucleon momentum that is carried by the struck quark. This holds to good approximation in the lab frame and serves as a practical way of interpreting x. Introducing the function, $f_i(x)$, which is the probability that parton i carries momentum fraction x, the structure function $F_1(x)$ can be interpreted as the charge weighted probability of finding any parton with momentum fraction x. In F_2, this probability is further scaled by x:

$$F_1(x) = \frac{1}{2}\sum_i e_i^2[f_i(x) + \overline{f}_i(x)] \tag{2.10}$$

$$F_2(x) = x\sum_i e_i^2[f_i(x) + \overline{f}_i(x)] \tag{2.11}$$

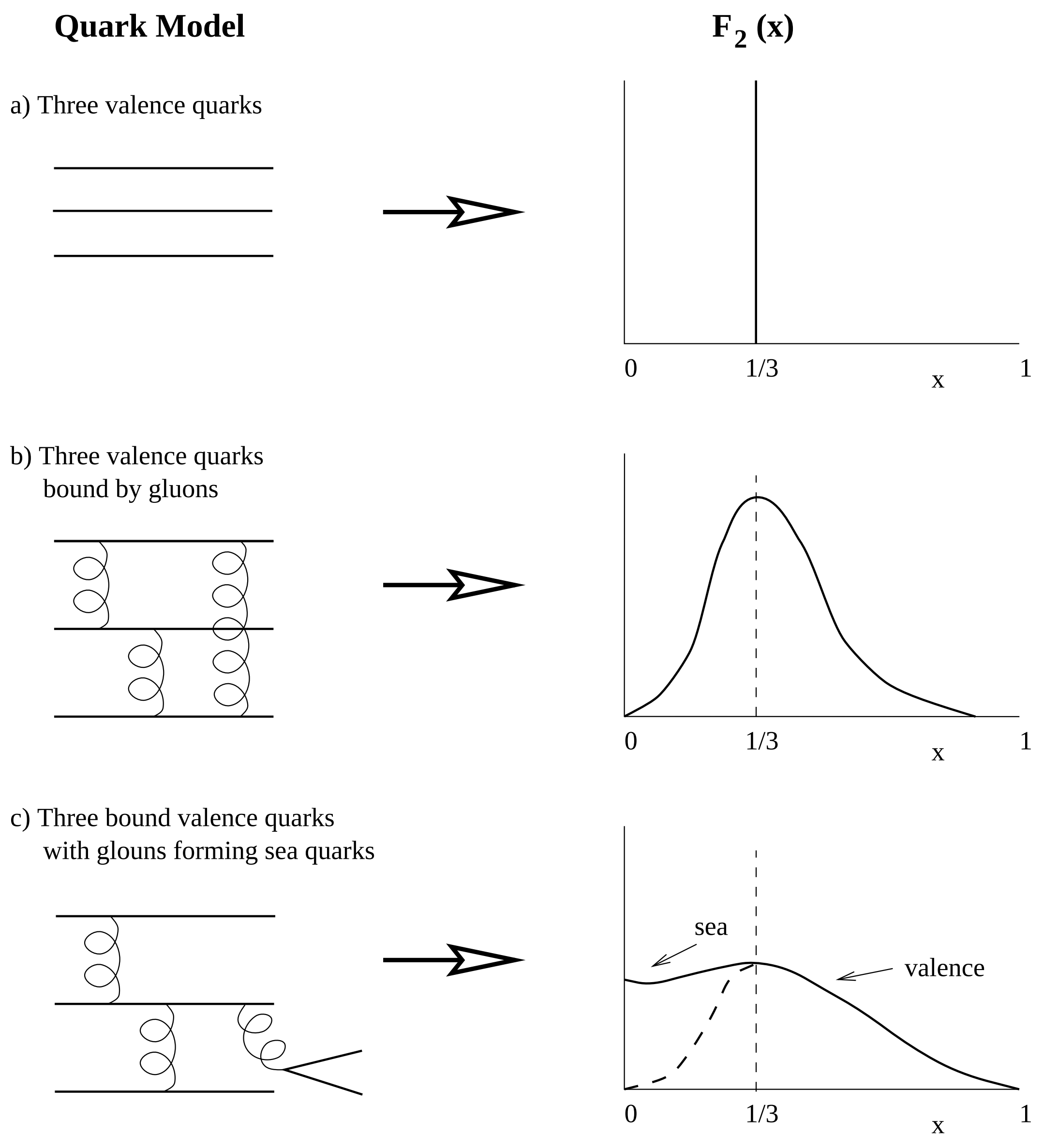

Figure 2.2: $F_2(x)$ distributions in the Quark Parton Model.[9]

where the sum is over quark flavours with $\overline{f}$ representing the anti-quark, and e_i is the charge of quark flavour i.

Figure 2.2 shows $F_2(x)$ distributions for different quark models. If the nucleon was made up of three non-interacting quarks of equal mass, each would carry $\frac{1}{3}$ of the nucleon momentum, and the structure function F_2 would be a delta function: $F_2(x) = \delta(x - \frac{1}{3})$. With interaction through the exchange of gluons, that distribution would spread to a broad function peaked at $x = \frac{1}{3}$. Fig. 2.2c is a result of sea quark formation. These quark-antiquark pairs tend to have a low momentum fraction and thus shift the momentum distribution to the low x range. While this is a simple argument for the shape of F_2, it is borne out by experiment.

If F_2 is integrated over all x, one would expect the result to be the momentum of the nucleon. However, the measured value of this integral shows that only half of the momentum is carried by the quarks.[13] The interpretation of this result is that the gluons carry the other half of the nucleon momentum.

Bjorken scaling and the Callen-Gross relation are based on the treatment of the quarks as free Dirac particles. However, this approximation is only good to first order. Experimental evidence[14] has shown that for $x \lesssim 0.1$, $F_2(x)$ increases with Q^2, and for $x \gtrsim 0.25$, $F_2(x)$ decreases with increasing Q^2. This additional dependence on Q^2 is known as scaling violation and arises from QCD radiative corrections such as internal gluon Bremsstrahlung. It then becomes more appropriate to write $F_{1,2}$ in terms of both x and Q^2. The Callen-Gross relation can be rewritten to include the scaling violations:

$$F_2(x, Q^2) = 2xF_1(x, Q^2)\left[\frac{1 + R(x, Q^2)}{1 + \frac{Q^2}{\nu^2}}\right]. \tag{2.12}$$

The parameter $R(x, Q^2)$ is the measure of the deviation from the Callen-Gross relation.[12]

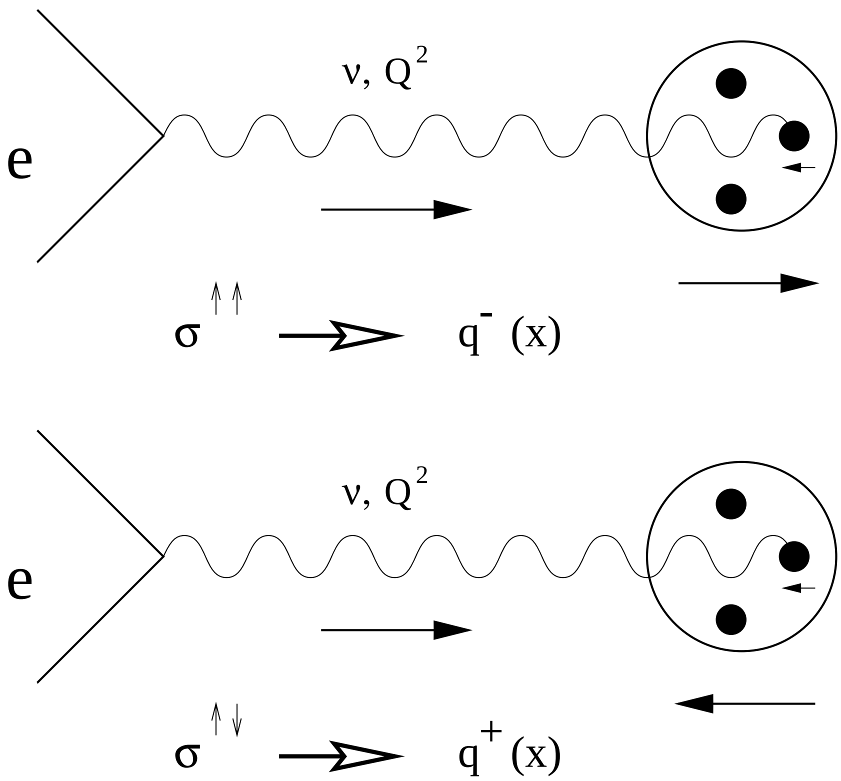

Figure 2.3: Polarised deep inelastic scattering. The arrows represent the polarisation direction of the particles.

2.2 Polarised Structure Functions

If the incoming lepton and the target are polarised, the cross section becomes a function of the spin structure of the nucleon. Polarised DIS is shown schematically in fig. 2.3. The polarised incoming lepton emits a polarised virtual photon absorbed by the quark. Since the final state is a quark which is a spin $\frac{1}{2}$ particle, the spin projections of the photon and the quark must add to $\frac{1}{2}$. Thus, the photon will only be absorbed by a quark whose spin is aligned oppositely to the virtual photon. If the lepton and the nucleon are polarised in the same (opposite) direction, the virtual photon is sensitive to collisions with quarks which have their spin opposite (parallel) to the nucleon spin. The spin structure function $g_1(x)$ is obtained from the relative probability of finding the quarks with their spins parallel and anti-parallel to the nucleon spin:

$$g_1 = \frac{1}{2}\sum_f e_f^2[q_f^+(x) - q_f^-(x) + \overline{q}_f^{\,+}(x) - \overline{q}_f^{\,-}(x)] = \frac{1}{2}\sum_f e_f^2 \Delta q_f(x). \tag{2.13}$$

Where the sum is over the quark flavours. Thus, this equation is the polarised equivalent to eq. (2.10).

In order to obtain g_1, one can measure the asymmetry

$$A_{||} = \frac{\sigma^{\uparrow\downarrow} - \sigma^{\uparrow\uparrow}}{\sigma^{\uparrow\downarrow} + \sigma^{\uparrow\uparrow}} \tag{2.14}$$

from the scattering of longitudinally polarised leptons on longitudinally polarised nucleons. There are two facts which complicate the matter. Given that a *virtual* photon is exchanged, it can have transverse and longitudinal components. Also, the quarks can have transverse momentum which couples to the longitudinal photon polarisation and gives rise to a second spin structure function, g_2. Given that g_2 is expected to be small, previous experiments have assumed it is zero and included it as a systematic error. HERMES is measuring g_2 since it will yield information on higher order perturbations.[15] To increase the sensitivity to g_2, the target is transversely polarised. The transverse asymmetry can then be measured:

$$A_{\perp} = \frac{\Sigma^{\uparrow\downarrow} - \Sigma^{\uparrow\uparrow}}{\Sigma^{\uparrow\downarrow} + \Sigma^{\uparrow\uparrow}} \tag{2.15}$$

where

$$\Sigma = \int cos^{-1}\phi \, \frac{d\sigma}{d\phi} \, d\phi \tag{2.16}$$

and ϕ is the azimuthal scattering angle between the polarisation plane and the scattering plane.

The measured asymmetries, $A_{||}$ and $A_{\perp}$, can be related to the virtual photon asymmetries, A_1 and A_2 by[8]

$$A_{||} = D \cdot (A_1 + \eta A_2) \tag{2.17}$$

$$A_{\perp} = d \cdot (A_2 - \xi A_1). \tag{2.18}$$

D, d, η, and ξ are kinematic factors defined by

$$D = \frac{y(2-y)}{y^2+2(1-y)(1+R)} \tag{2.19}$$

$$\eta = \frac{2\gamma(1-y)}{2-y} \tag{2.20}$$

$$d = D\sqrt{\frac{2\epsilon}{1+\epsilon}} \tag{2.21}$$

$$\xi = \eta\frac{1+\epsilon}{2\epsilon} \tag{2.22}$$

$$\epsilon = \frac{1-y}{1-y+y^2/2} \tag{2.23}$$

with $\gamma = \frac{\sqrt{Q^2}}{\nu}$; ϵ is the degree of transverse polarisation of the virtual photon, and D and d are depolarisation factors of the virtual photon. R is the factor defined in eq (2.12) and is the ratio of cross sections for longitudinally and transversely polarised photons. The virtual photon asymmetries are directly related to the photon absorption cross section of the nucleon at a given x and Q^2:

$$A_1 = \frac{\sigma_{1/2}-\sigma_{3/2}}{\sigma_{1/2}+\sigma_{3/2}} \tag{2.24}$$

$$A_2 = \frac{\sigma_{TL}}{\sigma_T} \tag{2.25}$$

where $\sigma_{1/2(3/2)}$ is the virtual photoabsorption cross section when the total angular momentum of the photon-nucleon system projected along the incident lepton direction is 1/2 (3/2), $\sigma_T = \frac{1}{2}(\sigma_{1/2}+\sigma_{3/2})$ is the total transverse photoabsorption cross section, and σ_{TL} is an interference term between the transverse and longitudinal amplitudes.

$A_{1,2}$ can also be expressed in terms of the structure functions which will allow a direct interpretation in terms of the quark distributions:

$$A_1 = \frac{g_1-\gamma^2 g_2}{F_1} \tag{2.26}$$

$$A_2 = \frac{\gamma(g_1+g_2)}{F_1}. \tag{2.27}$$

2.3 Sum Rules

Another approach to interpreting the structure functions is to integrate them over all x. In this way, one can examine the total contribution of the quarks to the momentum and the spin of the nucleon. There are several theoretical predictions of the value of these integrals for polarised DIS, known as *sum rules*. Among these are the Bjorken[16] sum rule and the Ellis-Jaffe[17] sum rules.

2.3.1 Bjorken Sum Rule

Using the definition of the spin structure function from equation (2.13), integration for the proton and neutron yields

$$I_1^p = \int_0^1 g_1^p(x)\,dx = \frac{1}{2}\left(\frac{4}{9}\Delta u + \frac{1}{9}\Delta d + \frac{1}{9}\Delta s\right) \tag{2.28}$$

$$I_1^n = \int_0^1 g_1^n(x)\,dx = \frac{1}{2}\left(\frac{4}{9}\Delta d + \frac{1}{9}\Delta u + \frac{1}{9}\Delta s\right). \tag{2.29}$$

The Δu, Δd, Δs refer to the integrated polarised quark distributions of the up, down, and strange quarks in the proton, and we have used the quark charges $e_u = 2/3$, $e_d = -1/3$, and $e_s = -1/3$. From isospin symmetry, the Δu and Δd which refer to distributions in the proton are interchanged for the proton and the neutron. The charm, bottom, and top quarks are neglected because they would contribute negligibly to the wave function due to their large masses.

Taking the difference of eqs. (2.28) and (2.29) gives

$$I_1^p - I_1^n = \frac{1}{6}(\Delta u - \Delta d). \tag{2.30}$$

This is related[16] to the neutron β decay coupling constants, g_A and g_V to produce

$$I_1^p - I_1^n = \frac{1}{6}\frac{g_A}{g_V}\left[1 - \frac{\alpha_s(Q^2)}{\pi}\right] \tag{2.31}$$

where α_s is the coupling constant of the strong interaction. The bracketed term comes from first order QCD corrections. This equation is the Bjorken sum rule. It is model independent and is a fundamental equation of QCD.

2.3.2 Ellis-Jaffe Sum Rules

In order to test the Bjorken sum rule, data on g_1 for both the proton and the neutron are required. Data from the neutron were obtained much later than the proton data; therefore, Ellis and Jaffe developed sum rules for g_1^p and g_1^n separately. In order to accomplish this, they had to assume exact $\mathrm{SU}(3)_F$ symmetry and zero strange quark polarisation, ie $\Delta s = 0$. This yields the sum rules

$$I_1^p = \frac{1}{12}\frac{g_A}{g_V}\left[1 + \frac{5}{3}\frac{3F - D}{F + D}\right] \times \text{QCD corrections} \tag{2.32}$$

$$I_1^n = \frac{1}{12}\frac{g_A}{g_V}\left[-1 + \frac{5}{3}\frac{3F - D}{F + D}\right] \times \text{QCD corrections} \tag{2.33}$$

where F and D are $\mathrm{SU}(3)_F$ coupling constants determined from hyperon β decay data.[18] These expressions satisfy the Bjorken sum rule.

Given that the Ellis-Jaffe sum rules are model dependent, their violation likely indicates a failure in the model. Since $\mathrm{SU}(3)_F$ is not an exact symmetry, this result would not be unexpected.

2.3.3 Measured Values

Recent experiments have provided measurements of the value of the sum rules. The EMC experiment[4] at CERN scattered polarised muons on polarised protons using an ammonia target. These data were combined with previous SLAC data[19] to obtain a value for I_1^p. The result violated the Ellis-Jaffe sum rule and indicated that the quarks contribute only a small fraction of the nucleon spin. This spawned what became known as the 'spin crisis' and led to the development of several other experiments.

The SMC experiment at CERN used a polarised muon beam scattered on butanol targets containing polarised protons[20] or deuterons[5] to provide measurements of both I_1^p and I_1^n in order to test the Bjorken sum rule. While the results agreed with the Bjorken sum rule, they were more than 2 standard deviations below the theoretical

Table 2.1: Summary of current data on polarised DIS sum rules and the anticipated uncertainty for HERMES[28]

Experiment (target)	Result	Theory	$< Q^2 >$ [GeV^2]
Ellis – Jaffe(proton) :			
EMC(NH_3)	$0.126 \pm .010 \pm .015$	0.189 ± 0.005	10
SMC(C_4H_9OH)	$0.136 \pm .011 \pm .011$	$0.176 \pm .006$	10
E143(NH_3)	$0.127 \pm .004 \pm .010$	$0.160 \pm .006$	3
HERMES(H)	$\pm .004 \pm .007$		
Ellis – Jaffe(neutron) :			
SMC(C_4D_9OD) & EMC(NH_3)	$-0.08 \pm .04 \pm .04$	$0.002 \pm .005$	4.6
E142(^3He)	$-0.022 \pm .007 \pm .009$	$-0.021 \pm .018$	2
E143(ND_3 & NH_3)	$-0.037 \pm .008 \pm .011$	$-0.021 \pm .018$	2
HERMES(H & D)	$\pm .007 \pm .004$		
HERMES(^3He)	$\pm .006 \pm .003$		
Bjorken :			
SMC(C_4D_9OD) & EMC(NH_3)	$0.20 \pm .05 \pm .04$	$0.191 \pm .002$	4.6
SMC(C_4D_9OD & C_4H_9OH) & E142(^3He)	$0.163 \pm .017$	$0.185 \pm .004$	5
E142(^3He) & EMC(NH_3)	$0.146 \pm .021$	$0.183 \pm .007$	2
E143(NH_3) & E142(^3He)	$0.149 \pm .014$	$0.171 \pm .008$	3
E143(ND_3) & E143(NH_3)	$0.163 \pm .010 \pm 016$	$0.171 \pm .008$	3
HERMES(H & D)	$\pm .010 \pm .011$		
HERMES(H & ^3He)	$\pm .008 \pm .007$		

value for the Ellis-Jaffe sum rule. The E142[6] experiment at SLAC scattered polarised electrons on a polarised ^{3}He target to study polarised neutrons. These data agreed with the Ellis-Jaffe sum rule, but when combined with the EMC data, yielded a value for the Bjorken sum rule which was two standard deviations below the predicted value. A further experiment at SLAC (E143) used ammonia targets to obtain g_1^p[7] and g_1^d.[21] These data are again well below the Ellis-Jaffe sum rule and in agreement with the Bjorken sum rule. The data from these experiments including statistical and systematic uncertainties are summarized in table 2.1.[28] Also included are expected uncertainties from the HERMES experiment.

A number of items still limit the interpretation of the results. The earlier data, particularly the EMC and SMC data, have fairly large uncertainties. The precision of the predicted values for sum rules is limited by the uncertainties in F and D and by the limitations on predicting higher order QCD corrections. Also, in order to obtain a value for the Bjorken sum rule, data from different experiments must be combined. This can lead to problems with scaling violations because the different data were measured at different Q^2. This clearly shows the need to have an experiment which will produce a complete set of high precision measurements.

The HERMES experiment represents a major advance in polarised DIS experiments. Not only is it making precise measurements of $g_{1,2}$ for both the proton and the neutron, it is also making measurements of several other structure functions.[8] Using separate H, D, and ^{3}He targets, HERMES measures both g_1^p and g_1^n using the same experimental apparatus. In addition, HERMES obtains two independent measurements of g_1^n from the ^{3}He data and from the D-H data. This will provide a consistency check. The large acceptance of the HERMES spectrometer allows measurement over a range of Q^2 which provides data on scaling violations. HERMES is measuring g_2^p and g_2^n which will allow for verification of the assumption that they are small. It will also provide a test of the validity of the Burkhardt-Cottingham sum rule:[24]

$$\int_0^1 dx\, g_2(x, Q^2) = 0. \tag{2.34}$$

Also, determining g_2 could allow the measurement of higher order QCD operators: the so-called twist 3 effects.[15] In addition, HERMES is the first experiment to measure the structure functions $b_1(x)$, $\Delta(x)$, $h_1(x)$. Δ[22] and b_1[23] are related to the spin 1 nature of the deuteron and contain information about quark-gluon correlations. h_1 is a chiral odd structure function related to the transverse spin asymmetries in the nucleon.

Given that the current data indicate that the total quark contribution to the spin is less than half of the total, it leads to the question of where is the rest of the spin. In order to fully understand the nucleon spin, it is necessary to examine the individual contributions of the spin response:

$$< S_z >= \frac{1}{2} = \frac{1}{2}(\Delta V + \Delta S) + \Delta G + L_z \tag{2.35}$$

where S_z is the nucleon spin, ΔV and ΔS are the valence and sea quark contributions, ΔG is from gluons, and L_z is the orbital angular momentum contribution. By identifying outgoing pions or kaons, HERMES will be able to make semi-inclusive measurements of hadrons in coincidence with the positron and yield information about the ΔV and ΔS components of the spin. Only qualitative data exist on semi-inclusive processes, and this is an area where HERMES can make a unique contribution.

2.4 Semi-Inclusive Physics

The semi-inclusive DIS reaction studied by HERMES is

$$e^+ + N \longrightarrow e^+ + h + X \tag{2.36}$$

where h is the leading, or highest energy hadron which would likely contain the struck quark, and X represents the fragments of the struck nucleon. Using the ratio of the hadron energy vs. the virtual photon energy:

$$z = E_h/\nu\,, \tag{2.37}$$

it is estimated from unpolarised DIS[25] that for an outgoing hadron with $z > 0.5$, the probability is greater than 70% that it will contain the struck quark. New Monte Carlo simulations of HERMES show that the leading hadron virtually always contains the struck quark.

Measurement of $N^{\pi^\pm}$, the number of $\pi^\pm$ particles produced for different beam and target polarisations yields information on the spin distribution of the valence quarks, Δu^v and Δd^v. This is given by:

$$\begin{aligned} N^{\pi^+}_{\uparrow\downarrow} \sim \frac{4}{9}u_+(x)D^{\pi^+}_u(z) + \frac{4}{9}\overline{u}_+(x)D^{\pi^+}_{\overline{u}}(z) + \frac{1}{9}d_+(x)D^{\pi^+}_d(z) \\ + \frac{1}{9}\overline{d}_+(x)D^{\pi^+}_{\overline{d}}(z) + \frac{1}{9}s_+(x)D^{\pi^+}_s(z) + \frac{1}{9}\overline{s}_+(x)D^{\pi^+}_{\overline{s}}(z) \end{aligned} \tag{2.38a}$$

$$N_{\uparrow\downarrow}^{\pi^-} \sim \frac{4}{9}u_+(x)D_u^{\pi^-}(z) + \frac{4}{9}\overline{u}_+(x)D_{\overline{u}}^{\pi^-}(z) + \frac{1}{9}d_+(x)D_d^{\pi^-}(z) + \frac{1}{9}\overline{d}_+(x)D_{\overline{d}}^{\pi^-}(z) + \frac{1}{9}s_+(x)D_s^{\pi^-}(z) + \frac{1}{9}\overline{s}_+(x)D_{\overline{s}}^{\pi^-}(z) \tag{2.38b}$$

$$N_{\uparrow\uparrow}^{\pi^+} \sim \frac{4}{9}u_-(x)D_u^{\pi^+}(z) + \frac{4}{9}\overline{u}_-(x)D_{\overline{u}}^{\pi^+}(z) + \frac{1}{9}d_-(x)D_d^{\pi^+}(z) + \frac{1}{9}\overline{d}_-(x)D_{\overline{d}}^{\pi^+}(z) + \frac{1}{9}s_-(x)D_s^{\pi^+}(z) + \frac{1}{9}\overline{s}_-(x)D_{\overline{s}}^{\pi^+}(z) \tag{2.38c}$$

$$N_{\uparrow\uparrow}^{\pi^-} \sim \frac{4}{9}u_-(x)D_u^{\pi^-}(z) + \frac{4}{9}\overline{u}_-(x)D_{\overline{u}}^{\pi^-}(z) + \frac{1}{9}d_-(x)D_d^{\pi^-}(z) + \frac{1}{9}\overline{d}_-(x)D_{\overline{d}}^{\pi^-}(z) + \frac{1}{9}s_-(x)D_s^{\pi^-}(z) + \frac{1}{9}\overline{s}_-(x)D_{\overline{s}}^{\pi^-}(z) \tag{2.38d}$$

where $\uparrow\uparrow$ ($\uparrow\downarrow$) refers to the relative polarisations of the target nucleon and the virtual photon. $D_q^{\pi^+(\pi^-)}(z)$ is the probability that a quark q will form a $\pi^+(\pi^-)$ with energy z, and is called the fragmentation function. By using isospin and charge conjugation symmetry to relate the fragmentation functions,[26] three independent fragmentation functions for the pion are obtained:

$$D_1(z) \equiv D_u^{\pi^+}(z) = D_{\overline{u}}^{\pi^-}(z) = D_d^{\pi^-}(z) = D_{\overline{d}}^{\pi^+}(z) \tag{2.39a}$$

$$D_2(z) \equiv D_d^{\pi^+}(z) = D_{\overline{d}}^{\pi^-}(z) = D_u^{\pi^-}(z) = D_{\overline{u}}^{\pi^+}(z) \tag{2.39b}$$

$$D_3(z) \equiv D_s^{\pi^+}(z) = D_{\overline{s}}^{\pi^+}(z) = D_s^{\pi^-}(z) = D_{\overline{s}}^{\pi^-}(z). \tag{2.39c}$$

These are referred to as the favoured, unfavoured, and strange quark fragmentation functions. The suppression factor, $1/\eta$ between the favoured and unfavoured fragmentation functions is given by[27]

$$D_2(z) = \frac{1}{\eta}D_1(z) = \frac{1-z}{1+z}D_1(z). \tag{2.40}$$

Subtracting eqs. (2.38a) from (2.38b) and (2.38c) from (2.38d) yields equations in which the sea quark contribution cancels:

$$N_{\uparrow\downarrow}^{\pi^+-\pi^-} \sim [\frac{4}{9}u_+^v(x) - \frac{1}{9}d_+^v(x)][D_1(z) - D_2(z)] \tag{2.41a}$$

$$N_{\uparrow\uparrow}^{\pi^+-\pi^-} \sim [\frac{4}{9}u_-^v(x) - \frac{1}{9}d_-^v(x)][D_1(z) - D_2(z)] \tag{2.41b}$$

where $q^v_\pm \equiv q_\pm - \overline{q}_\pm$ is the valence quark distribution.

Defining the double pion asymmetry for the proton

$$A^p_\pi = \frac{N^{\pi^+-\pi^-}_{\uparrow\downarrow} - N^{\pi^+-\pi^-}_{\uparrow\uparrow}}{N^{\pi^+-\pi^-}_{\uparrow\downarrow} + N^{\pi^+-\pi^-}_{\uparrow\uparrow}} \tag{2.42}$$

the fragmentation functions cancel, and one obtains the relatively simple function:

$$A^p_\pi = \frac{4\Delta u^v(x) - \Delta d^v(x)}{4u^v(x) - d^v(x)} \tag{2.43}$$

where $q^v(\Delta q^v)$ are the unpolarised (polarised) valence quark distributions. Similarly, the pion asymmetries for the deuteron and ^{3}He targets are

$$A^d_\pi = \frac{\Delta u^v(x) - \Delta d^v(x)}{u^v(x) - d^v(x)} \tag{2.44}$$

$$A^{^3He}_\pi = \frac{\Delta u^v(x) - 4\Delta d^v(x)}{7u^v(x) - 2d^v(x)}. \tag{2.45}$$

Since the unpolarized distributions are known, the pion asymmetry can be used to determine the polarised valence quark distributions. Comparison of the pion asymmetries from two different targets allows one to solve for Δu^v and Δd^v individually.

The non-strange sea quark contribution, Δq^s can be measured by examining leading π^- at high z and low x.[29] The pion spin asymmetry in this case is

$$A_{\pi^-}(x) = \frac{N^{\pi^-}_{\uparrow\downarrow} - N^{\pi^-}_{\uparrow\uparrow}}{N^{\pi^-}_{\uparrow\downarrow} + N^{\pi^-}_{\uparrow\uparrow}}. \tag{2.46}$$

For the proton, using the assumption that $D_s \approx D_2$, this yields

$$A^p_{\pi^-} = \frac{4\Delta u^v + \eta\Delta d^v + 5(1+\eta)\Delta q^s + 2\Delta s}{4u^v + \eta d^v + 5(1+\eta)q^s + 2s}. \tag{2.47}$$

Kaons are more sensitive for the study of the strange sea quark contribution. In particular, K^- consists of $(s\overline{u})$ quarks which exist only in the sea. The K^+ mesons would be dominated by fragmentation from valence u quarks and would not prove to be highly useful. As with the analysis of the pions, K^- with high z and low x should be examined in order to make sure that the kaon resulted from fragmentation of the struck quark and not from the target fragmentation. This restriction is referred to as Berger's criterion.[30] The resulting K^- spin asymmetry for the proton is[27]

$$A^p_{K^-} = \frac{4\Delta u^v + \Delta d^v + (6+4\eta)\Delta q^s + (\frac{\eta}{\lambda}+1)\Delta s}{4u^v + d^v + (6+4\eta)q^s + (\frac{\eta}{\lambda}+1)s} \tag{2.48}$$

with $\lambda \approx 0.3$ being the suppression factor for generating an s quark during fragmentation compared to the production of a u or d quark:

$$D^{K^-}_{\overline{u}} = \lambda D^{K^-}_{s}. \tag{2.49}$$

It is due to the mass of the s quark compared to u and d.

Thus, with the ability to identify the leading hadrons, HERMES is able to measure the polarisation of the valence and sea quarks. The anticipated precision of the valence quark polarisation is about 15%.[8]

Chapter 3

The HERMES Experiment

The HERMES experiment is being done at the DESY laboratory in Hamburg, Germany, and utilizes the electron storage ring of the HERA accelerator. HERA is a high energy collider which produces an 820 GeV proton beam and a 27.5 GeV electron/positron beam. The proton beam is not used in the HERMES experiment. Longitudinally polarised positrons are scattered from an internal gas target consisting of pure samples of hydrogen, deuterium or ^{3}He. The scattered particles are measured by the HERMES spectrometer. A schematic view of HERMES is shown in fig. 3.1. This chapter will give a description of the target, spectrometer and particle identification systems.

3.1 The HERMES Target

The requirements for HERMES are a pure target with a high degree of polarisation. Currently, this can only be achieved using a gaseous target. Previous experiments have used solid targets consisting of ammonia or butanol in which only the hydrogen atoms were polarised. This allowed for a high atomic density, but also produced a high dilution factor, which is the ratio of polarisable nucleons to the total number of nucleons in the target. Also, a solid target cannot be used in a storage ring because

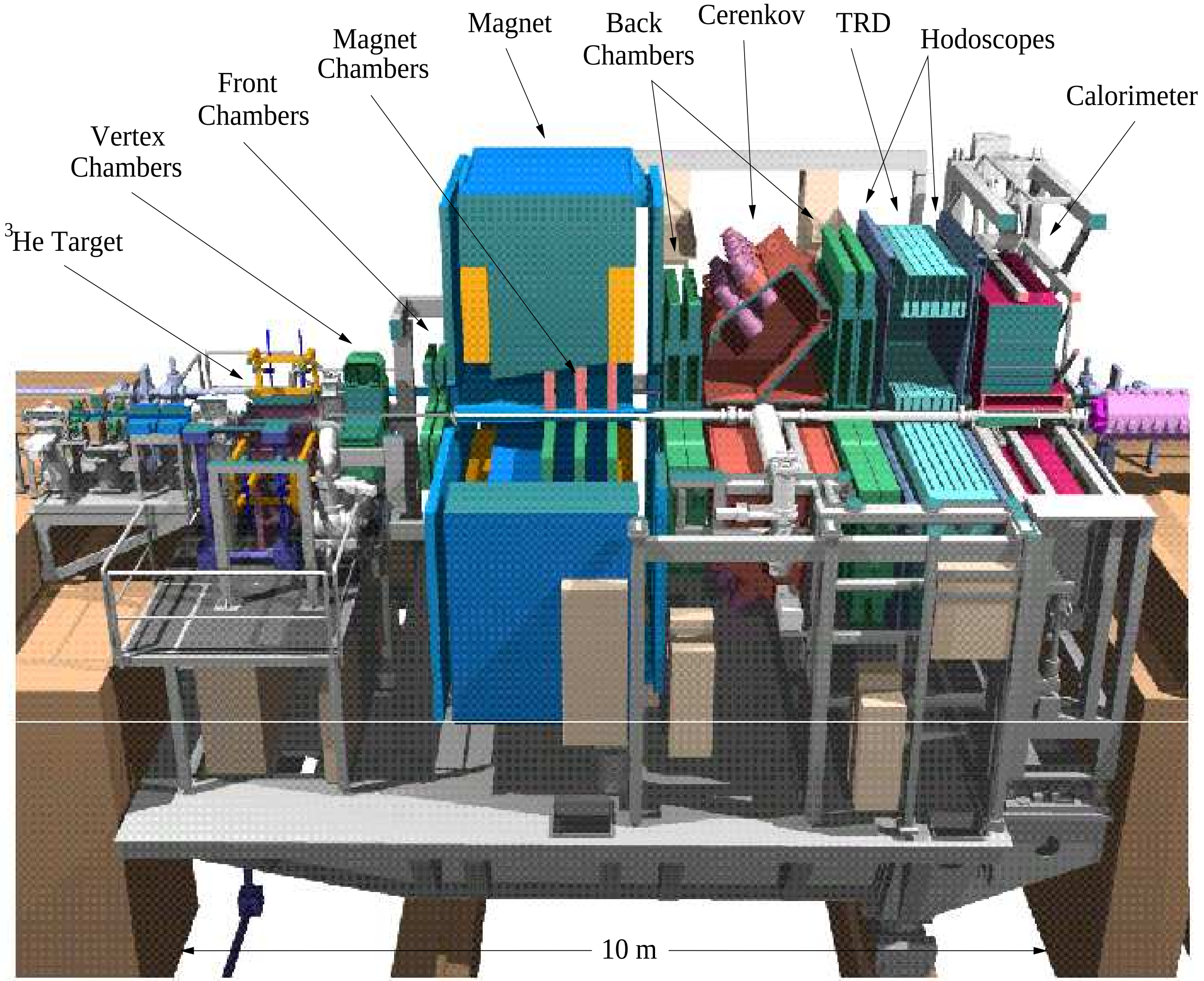

Figure 3.1: Schematic drawing of HERMES

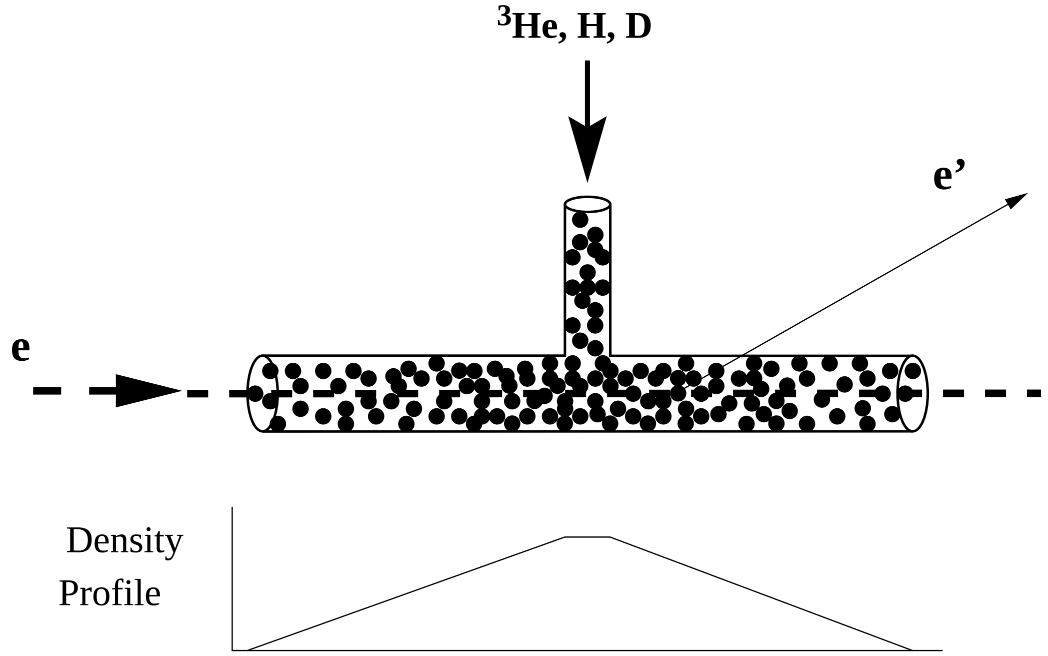

Figure 3.2: Schematic drawing of the storage cell

it would destroy the beam. There is no dilution for pure H and D, and it is only $\frac{1}{3}$ for ^{3}He. However, the disadvantage of the gaseous target is a loss in density.

The reaction rate is greatly improved by placing the target into an accelerator storage ring and by using a windowless storage cell. The storage ring provides a beam of higher current than an external beam. The storage cell shown in fig. 3.2 produces a much greater target density than a free gas jet. The gas is injected into the T-shaped tube which is positioned in the positron beam. The gas molecules in the cell collide frequently with the walls which increases the dwell time and provides an increased probability of interaction with the beam passing through the center. The target atoms are removed from the beam pipe by vacuum pumps located at each end of the storage cell. The positrons interact with the target atoms without a large background signal due to collisions with the cell wall.

The gas is polarised externally before entering the storage cell. The polarisation can be flipped quickly (seconds for ^{3}He and milliseconds for H, D) which reduces the systematic errors in the asymmetry. The current HERMES ^{3}He source delivers $1.2 \cdot 10^{17}$ atoms/s with a polarisation of 45%.[8] For the H/D source, the intensity is $6 \cdot 10^{16}$ atoms/s with better than 90% polarisation.[28]

3.2 The HERMES Spectrometer

The scattered particles are measured by the HERMES spectrometer which has an angular acceptance of $40 < \theta < 220$ mrad, where θ is the positron scattering angle. The kinematic plane covered by the spectrometer is shown in fig. 3.3 including the

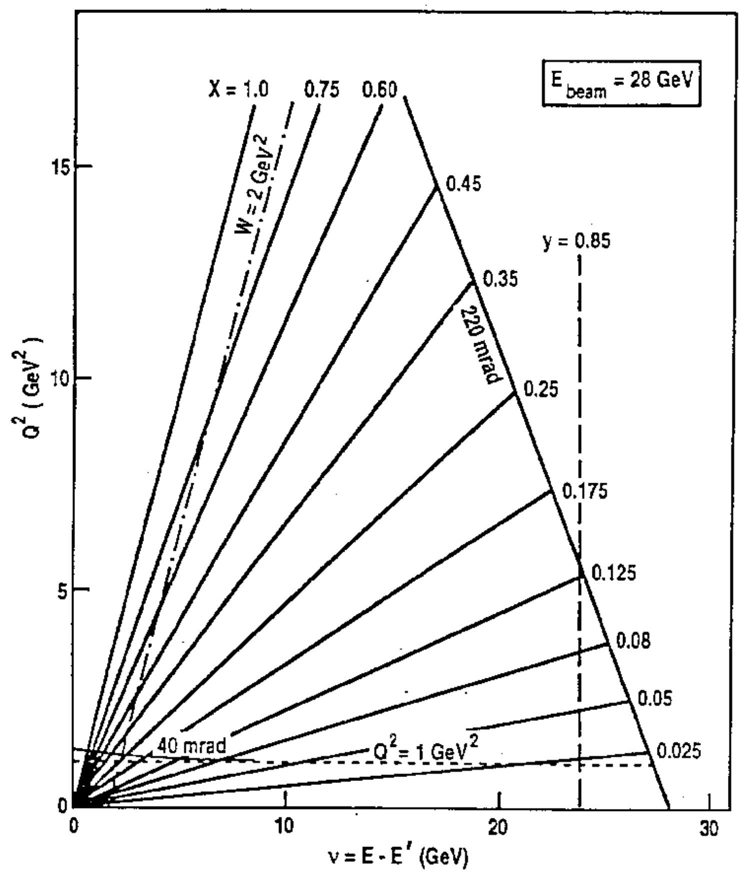

Figure 3.3: Kinematic plane for a positron beam of 28 GeV[28]

applied cuts on the data. The cuts required for the analysis are that Q^2 must be greater than 1 $(\mathrm{GeV/c})^2$ in order to allow the data to be interpreted in the quark parton model, and that the invariant mass $W > 2$ GeV to eliminate the nucleon resonance region. The energy of the scattered positron is cut at $y = 0.85$ in order to avoid the region of large radiative corrections and large hadronic background. Thus, the x range of the experiment is $0.02 < x < 0.8$ with an anticipated resolution which varies from 1% to 8%.[8]

The tracks of the scattered particles entering the main magnet of the spectrometer are obtained using data from a series of detectors located between the target and the magnet. This allows a determination of the vertex position and the scattering angle for the event. The first detectors are a pair of micro-strip gas counters known as the 'vertex chambers' (VC1 and VC2). These are followed by a pair of drift chambers ('front chambers' FC1 and FC2). The momentum of the particles and the sign of the charge is determined by the deflection of the particle in the magnetic field of the spectrometer dipole magnet. The track of the deflected particle is determined by two pairs of drift chambers ('back chambers' BC1-4) downstream of the magnet. In the magnet are three proportional chambers (MC1-3) which help to resolve ambiguities in matching front and back tracks. The energy of the particles is also measured by a lead glass calorimeter (CAL) at the downstream end of HERMES. Due to the presence of a septum plate in the beam plane of the magnet, all detectors are divided into components above and below the beamline. This septum plate shields the HERA beam from the magnetic field of the spectrometer.

3.3 Particle Identification

Due to the large, charged hadronic background from photoproduction, the anticipated ratio of pions to electrons is as high as 400:1 at 4.5 GeV and angles of 7-8 degrees as shown in fig. 3.4.[8] Several types of detectors are utilized for particle identification. The calorimeter provides a rejection factor greater than 300:1 for charged pions whose

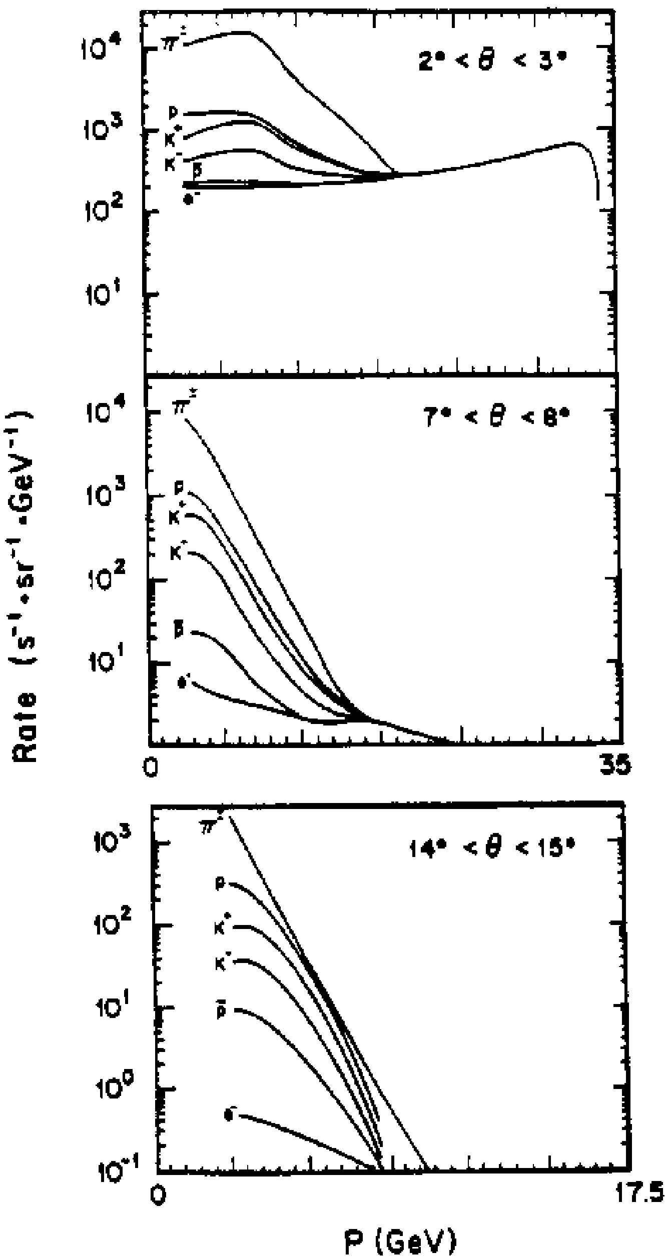

Figure 3.4: Cumulative charged particle rates for a luminosity of $3 \cdot 10^{32}$ cm^{-2}s^{-1} (^{3}He) for a) $2° < \theta < 3°$, b) $7° < \theta < 8°$, and c) $14° < \theta < 15°$.[8]

momenta have been measured by the spectrometer. To reduce the pion contamination to a negligible level, the pion rejection must be increased by at least a factor of 100.

A Čerenkov detector could in principle provide adequate hadron rejection. However, due to the fact that β for both the hadrons and the positrons is essentially 1, the number of photoelectrons produced would be low. In order to produce a sufficient number of photoelectrons for the required pion rejection, the detector would need to be prohibitively long. However, HERMES uses a Čerenkov detector located between BC1/2 and BC3/4 in order to distinguish between pions and other hadrons.

In order to achieve the desired pion rejection, a detector which is sensitive to γ instead of β is preferable. This is the role of the transition radiation detector. When an ultrarelativistic particle ($\gamma \gtrsim 1000$) traverses the boundary between two dielectrics, radiation is produced. Given that a 5 GeV electron has $\gamma \approx 10000$ while a pion of the same energy has $\gamma \approx 35$, only the electron radiates. Thus, the transition radiation will allow for identification of the electron. The HERMES TRD is located behind BC3/4. It consists of two stacks of 6 modules each consisting of a layer of radiator material and a proportional counter. With this configuration, a pion rejection factor of 100:1 has been achieved.

Chapter 4

The Transition Radiation Detector

The phenomenon of transition radiation (TR) was first predicted in 1946.[31] Practical interest in this phenomenon was limited due to the inherently low intensity of the radiation in the optical regime.[32] Interest became renewed when Garibian showed that TR was also produced as X-rays,[33] and it was first demonstrated to be useful in identifying ultrarelativistic particles in the early 1970's.[34] The transition radiation detector is still a relatively new type of detector which has become an important addition to modern high energy physics experiments. The ability to distinguish between ultrarelativistic particles using the Lorentz factor $\gamma = E/mc^2$ allows for efficient particle identification at high energy. This chapter will detail the theory behind the production and detection of TR. It will also describe the HERMES TRD and criteria which must be met in order to achieve the 100:1 pion rejection factor.

4.1 Transition Radiation

A charged particle moving uniformly through a vacuum does not radiate, but in the case of a highly relativistic particle moving through a medium, Cerenkov radiation will be produced if its velocity exceeds the local speed of light. The particle will also produce radiation when it crosses the boundary into a medium with a different dielectric constant. This is due to the reorganizing of the Coulomb fields around the particle as it enters the new medium.[35] A good analogy to Bremsstrahlung can be drawn for this phenomenon.[36] In the case of Bremsstrahlung, a particle emits radiation due to its non-uniform motion in a constant dielectric, while TR is emitted by a charge moving uniformly through a changing dielectric. In both cases radiation is produced when there is a change in the relationship between the velocity of the particle and the phase velocity of the electromagnetic waves in the medium. A more thorough analysis of TR can be found in references [35–38].

For a particle at high γ entering a medium, the TR energy will be in the form of visible light and X-rays. In the X-ray case, the medium can be considered as an electron gas, with a dielectric constant of:

$$\epsilon(\omega) = 1 - \omega_p^2/\omega^2 = 1 - \xi^2 \tag{4.1}$$

where ω is the frequency of the X-ray, and ω_p is the plasma frequency of the medium:

$$\omega_p^2 = 4\pi\alpha n_e/m_e \tag{4.2}$$

with n_e = electron density and $\alpha = \frac{1}{137}$. The TR energy produced per unit solid angle Ω, per unit frequency ω is given by:

$$\frac{d^2W}{d\omega d\Omega} = \frac{\alpha}{\pi^2}\left[\frac{\theta}{\gamma^{-2}+\theta^2+\xi_g^2} - \frac{\theta}{\gamma^{-2}+\theta^2+\xi_f^2}\right]^2 \tag{4.3}$$

where θ is the angle of emission, and subscripts g, f refer to *gas* and *foil*, representing the two dielectric media. This is an approximation subject to the following conditions:

$$\xi_g^2, \xi_f^2 \ll 1\,; \quad \theta \approx \frac{1}{\gamma} \ll 1. \tag{4.4}$$

Notice that the angle of emission is extremely small, and therefore the transition radiation is coincident with the particle. As can be seen from eq. (4.3), the yield is proportional to the electromagnetic coupling constant α. Thus, the probability for a particle to produce a TR photon at the boundary is $\sim \frac{1}{137}$. In order to produce enough TR photons to obtain a detectable signal, many layers of the dielectric radiator must be used. This is generally achieved through the use of a stack of thin dielectric foils separated by a gap of air or more ideally, vacuum.

The total integrated yield for a single transition is then:

$$W = \frac{2}{3}\alpha\gamma\omega_p. \tag{4.5}$$

Thus, the energy radiated is proportional to γ. However, the use of a multi-layer radiator can introduce effects which will cause saturation and reduce the proportionality to γ.

The TR is caused by a reorganization of the fields around the particle when it enters a new medium. This process occurs over a finite distance. The minimum distance, z, that a particle has to travel in the new medium for the fields to reach a new equilibrium is known as the formation zone:

$$z \approx \frac{2c}{\omega(\gamma^{-2} + \theta^2 + \xi^2)}. \tag{4.6}$$

If the thickness of the medium is much less than the formation zone, then the yield is strongly reduced by interference effects.

The formation zone also affects the TR energy for γ greater than the quantity:

$$\gamma_1 = \omega_1/\omega_{Pf} \tag{4.7}$$

where

$$\omega_1 = l_f\omega_{Pf}^2/2\ , \tag{4.8}$$

and l_f and ω_{Pf} are the thickness and plasma freqeuncy respectively of the radiator foil. For $\gamma > \gamma_1$ the mean radiated energy W increases only logarithmically with γ instead of linearly. The coefficient of the logarithm is of the order of $\alpha\omega_1$. A graph of the TR yield as a function of ω and γ is shown in fig. 4.1. The function $G(\nu, \Gamma)$ is given by:

$$\frac{dW}{d\omega} = \frac{2\alpha}{\pi}G(\nu, \Gamma) \tag{4.9}$$

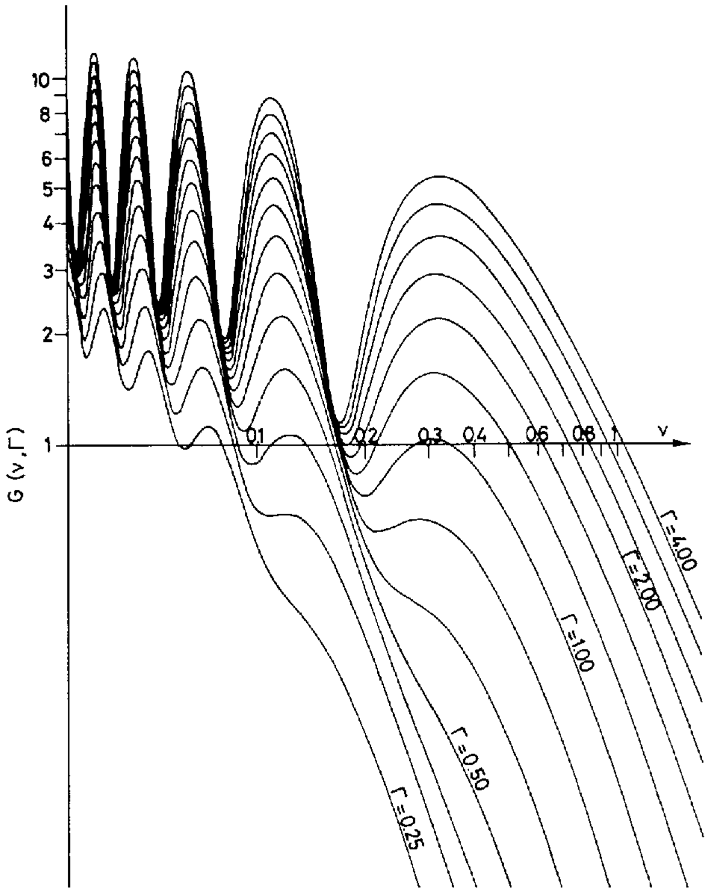

Figure 4.1: Transition radiation energy spectrum.[37] The value $\nu = 1$ corresponds to an energy of 17 keV for the HERMES TRD.

where ν and Γ are the dimensionless quantities:

$$\Gamma = \gamma/\gamma_1 \ , \tag{4.10}$$

$$\nu = \omega/\omega_1 . \tag{4.11}$$

The radiators used in the HERMES TRD are 17 μm polypropylene (CH_2). This results in $\omega_1 \approx 17$ keV. Only the TR at energies higher than a few keV (ie the highest node in fig. 4.1) are detected. The rest are absorbed in the radiator.

In eq. (4.3), the frequencies and the Lorentz factor are coupled together as $\gamma^{-2}+\xi_f^2$ and $\gamma^{-2}+\xi_g^2$. By making the transformations

$$\omega'_{p_f} = (\omega^2_{p_f} - \omega^2_{p_g})^{1/2}\,, \quad \omega'_{p_g} = 0 \;\; \text{(vacuum)} \tag{4.12}$$

$$\gamma' = (\gamma^{-2} + \xi_g^2)^{-1/2}\,, \tag{4.13}$$

they can be related to the condition of a vacuum gap between the foils. It can be seen that $\gamma' \leq \gamma$ and $\omega'_{p_f} \leq \omega_{p_f}$. Thus, the yield in gas will be smaller than the yield in vacuum. Furthermore, for $\omega_{p_g} \neq 0$ the yield saturates when

$$\gamma \gtrsim \xi_g^2 = \omega/\omega_{p_g}. \tag{4.14}$$

Using air, which has $\omega_p = 0.7$ eV, saturation occurs above $\gamma \sim 10^4$ for 10 keV X-rays.

The production of a strong TR signal is also restricted by the fact that the radiator material will absorb the X-ray photons. Thus, adding extra layers of radiator will only produce a limited increase in the number of photons. A solution to this problem is to use an alternating structure of radiators and detectors. In this way, the total amount of radiator in the system can be made much thicker, but the TR photons will reach a detector before they are reabsorbed by the radiator.

4.2 Detection

The difficulty in detecting the TR is that the incident particle is traveling in coincidence with the X-ray photons; both of which can produce a signal in the detector. The signal is obtained from the TR and the charged particles through the production of secondary electrons in a gas which are collected at an anode wire. These electrons are produced differently by photons and charged particles, but their collection at the anode is the same.

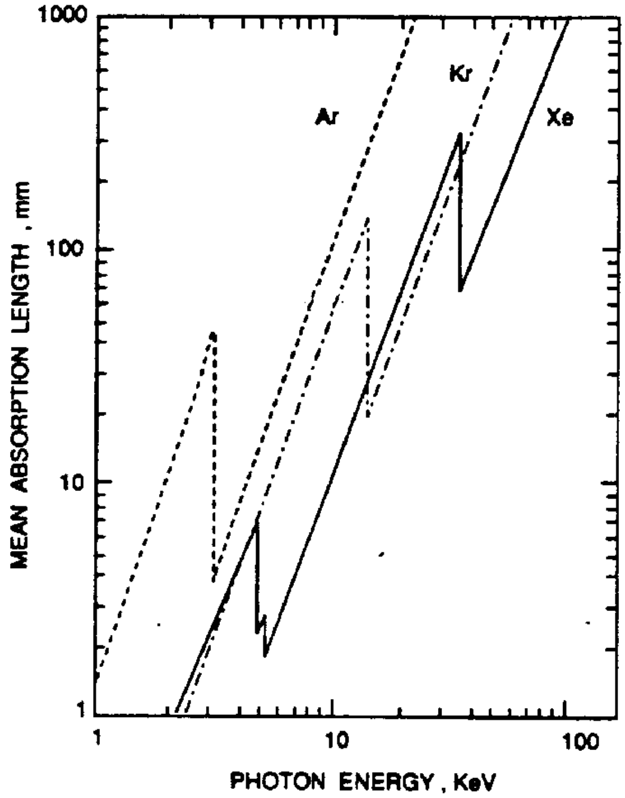

Figure 4.2: Mean absorption length of Ar, Kr, and Xe[36]

4.2.1 X-rays

There are three main processes for the detection of photons in a gas. For low photon energies of several keV, photoelectric absorption is the main process. For higher energies, up to a few hundred keV, Compton scattering becomes dominant, and for high energy photons, the most probable process is electron-positron pair production. Thus, given that the TR X-rays have an energy of a few keV, the dominant process for detecting them is photoelectric absorption.

The photon flux absorbed in a thickness l of the gas is given by

$$F = 1 - e^{-l/\lambda} \tag{4.15}$$

where λ is the mean absorption length which is a function of the photon energy and the gas. A graph of λ vs photon energy is given in fig. 4.2.[36] It is generally the case that a higher Z atom will have a shorter absorption length. Photoelectric absorption is a quantum mechanical process involving transitions in the electron shells of an atom or molecule. An X-ray photon of energy E_γ can only be absorbed in shell j if the shell binding energy $E_j \leq E_\gamma$. Absorption of the photon results in the emission of a photoelectron with energy $E_e = E_\gamma - E_j$.[39]

The excited atom/molecule can return to its ground state mainly through two mechanisms: fluorescence and the Auger effect. In fluorescence, an electron from a shell with binding energy $E_i < E_j$ drops into the j shell with the emission of a photon of energy $E_j - E_i$. In this case, the absorption length of this photon is much longer because its energy is below E_j, and this energy could escape detection leading to an error in the determination of the energy of the incident particle. The Auger effect is a radiationless transition which involves internal rearrangement of several electrons from higher energy shells with the release of an electron of energy slightly less then E_j. Thus, almost all of the X-ray photon's energy is converted into electrons which can be detected.

4.2.2 Charged Particles

A fast charged particle loses energy in a gas primarily through Coulomb interactions which cause excitation and ionization of the atoms in the gas. The energy loss per unit length is given by the Bethe-Block formula:

$$\frac{dE}{dX} = -K\frac{Z\rho}{A\beta^2}\left[\ln\frac{2mc^2\beta^2E_M}{I^2(1-\beta^2)} - 2\beta^2\right] \tag{4.16}$$

with Z, A, ρ and I being the atomic number, mass, density, and ionization potential of the medium respectively. K is given by

$$K = \frac{2\pi Nz^2e^4}{mc^2} = 0.154 MeV cm^2/g \tag{4.17}$$

where N is the Avogadro number, m and e are the electron mass and charge, and z is the charge of the particle. E_M is the maximum energy transfer allowed per interaction:

$$E_M = \frac{2mc^2\beta^2}{1-\beta^2}. \tag{4.18}$$

From eq. (4.16) it can be seen that the energy loss falls quickly due to the β^{-2} term. Above $\beta \approx 0.97$, the energy loss reaches a constant value which is known as the minimum ionizing region. It can be seen from fig. 4.3[39] that above a few hundred MeV, all particles are at the minimum ionizing region and have approximately the same energy loss per unit length. However, as $\beta \to 1$, the energy loss begins to increase; this phenomenon is referred to as the relativistic rise and is shown in fig. 4.4. These ionizing events occur throughout the gas and are referred to as dE/dX events.

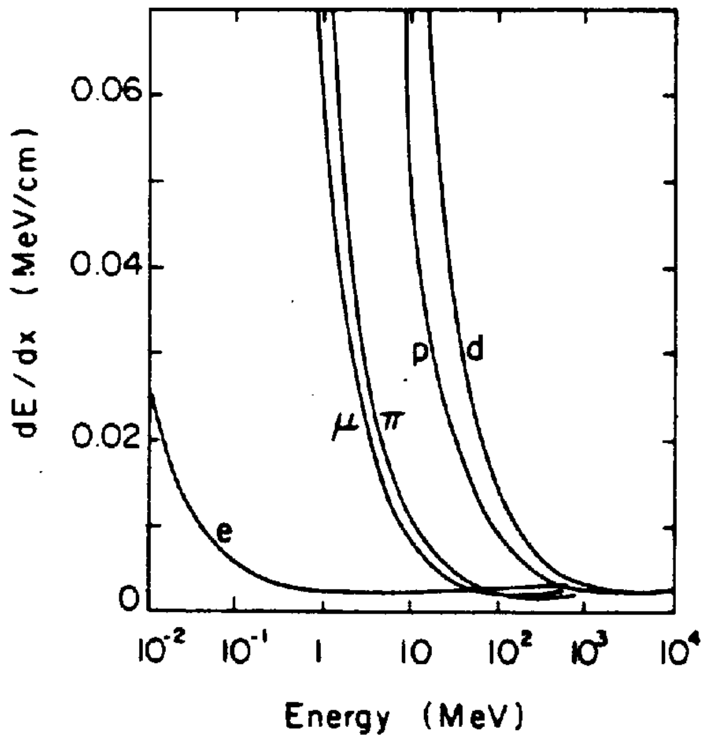

Figure 4.3: Energy loss per unit length in air.[39]

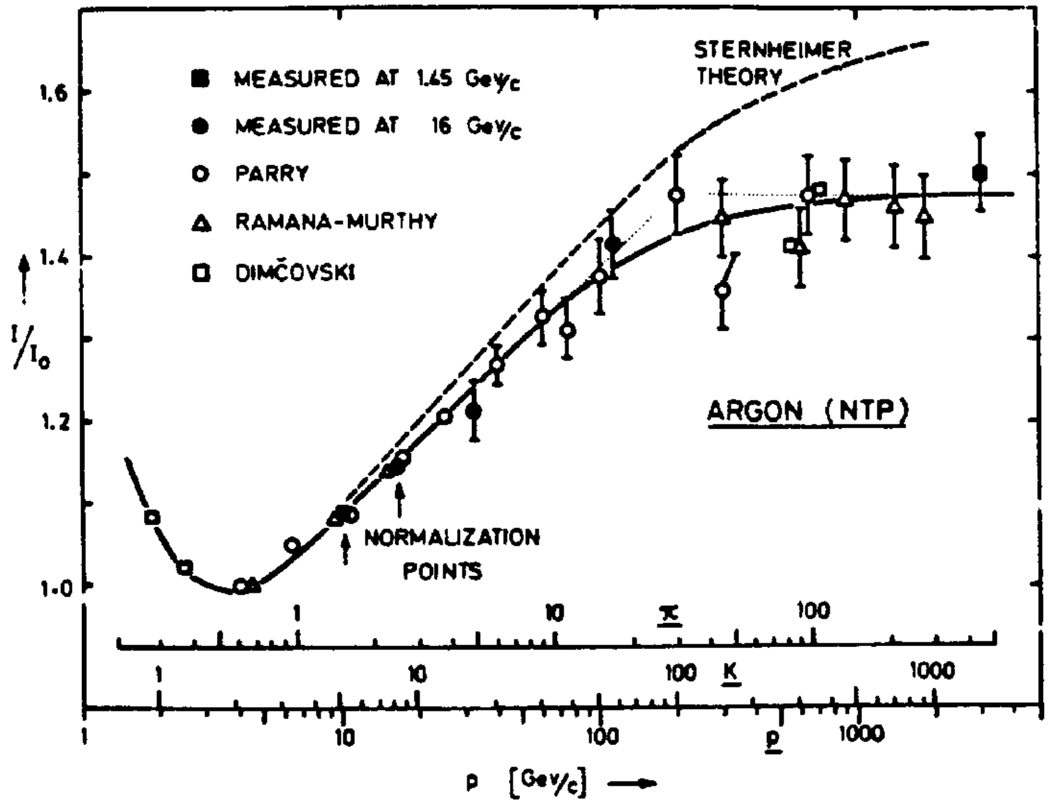

Figure 4.4: Relativistic rise of the dE/dx energy loss.[39]

4.2.3 Detection of Secondary Electrons

If the released electrons have an energy greater than the ionization energy of the gas, they will cause further ionization. In an applied electric field E, the electrons will drift with speed given by

$$w = \frac{e}{2m} E\tau \tag{4.19}$$

where τ is the mean time between collisions. With a sufficiently large electric field, the electrons will gain enough energy between collisions to further ionize the gas. This process creates an avalanche multiplication because each electron will produce a new pair on the next collision. The number of electrons n produced at a given position x is

$$n = n_0 e^{\alpha x} \tag{4.20}$$

where α is the number of ion pairs per unit length of drift and is known as the Townsend coefficient; it is the reciprocal of the mean free path of the electron. Given that the collisions occur randomly, the actual number of electrons produced is relatively random. Thus, there is a range of energies deposited in a detector from this process.

The multiplication factor is the increase in ion pairs produced by the avalanche:

$$M = \frac{n}{n_0} = e^{\alpha x}. \tag{4.21}$$

In the general case of a non-uniform electric field, $\alpha = \alpha(x)$ and the multiplication factor becomes

$$M = \exp\left[\int_{x_1}^{x_2} \alpha(x)dx\right]. \tag{4.22}$$

An effective way to produce a large multiplication factor is to use a very thin anode wire running down the center of a tube with the walls acting as the cathode. A voltage V_0 is applied to the anode such that its polarity is positive with respect to the walls. The electric field is maximum at the anode wire and rapidly decreases proportional to r^{-1}:

$$E(r) = \frac{CV_0}{2\pi\epsilon_o}\frac{1}{r} \tag{4.23}$$

where ϵ_o is the dielectric constant and C is the capacitance per unit length. For thin wires, very high field values can be achieved. The charge is collected at the anode which produces the signal in the detector. This design is known as a proportional counter since the signal size depends on the applied voltage and the energy deposited by the passing particle. The multiplication factor for a given voltage V_0 is

$$M = Ke^{CV_0} \tag{4.24}$$

where K is defined by eq. (4.17).

The multiwire proportional chamber developed by Charpak et al,[40] is an extension of the simple proportional counter. It consists of an evenly spaced row of anode wires at equal voltage between two cathode foils. The fields from the wires interact to provide a parallel, uniform field perpendicular to the row of wires except in the region very close to them. In this region, where the avalanche takes place, the fields become roughly that of eq. (4.23). The capacitance per unit length of the system is given by

$$C = \frac{2\pi\epsilon_o}{(\pi l/s) - ln(2\pi a/s)} \tag{4.25}$$

where l is the distance between anode and cathode, s is the wire spacing and a is the radius of the anode wire. Using this capacitance, the gain of the chamber is given by eq. (4.24).

4.2.4 Discrimination

In a proportional counter, both the photoelectrons from TR absorption and the dE/dx secondary electrons are detected. In order to determine the source of the signal, one must consider the properties of the two sources. By carefully exploiting the differences in the signal production, it is possible to identify effectively the TR X-rays.

One method is to apply a magnetic field to the system between the radiator and the detector. The charged particles will be bent in the field, and the TR can be separated from the incident particle. There are two main problems with this method. First, as the charged particles are bent away from the detector, they will produce synchrotron radiation which can cause erroneous readings. Also, in most experiments, there is a very limited space in which to build the detectors, and a magnet capable of producing a sufficient field to bend the high energy particles would be extremely difficult to incorporate into the system.

The standard type of TRD involves a multiwire proportional chamber which will detect the signal from both sources. There are two main methods of signal processing which can determine whether a TR signal was detected: cluster counting and total energy deposition. The essential difference between these methods is that the latter uses the total energy of the signal, while the former analyzes the distribution of the energy in the chamber.

As can be seen in Fig. 4.2, a 5-10 keV X-ray is absorbed in Xe within a few mm. Also, essentially all of the energy from the X-ray is deposited at the point of absorption. By contrast, the dE/dX energy loss of the particle occurs evenly throughout the length of the detector and produces a more distributed signal. In this way, the signal from the TR produces a burst of higher energy compared to the relatively smooth dE/dX signal. By triggering on the signal clusters above an energy threshold related to the fluctuation in the dE/dX energy, the TR signal can be discriminated. However, this result is contaminated by δ-rays. These are high energy fluctuations in the dE/dX signal due to high momentum transfer interactions with the ionizing particle. By analyzing the probability of δ-ray production, this contamination can be taken into account, and a reliable measurement of the TR signal can be obtained. The main drawback of the cluster counting method is that it requires very fast electronics in order to process the distribution of the signal. The detector must have a time resolution of 10 ns in order to discriminate the TR signal. This can be extremely expensive.

The total energy deposition method makes use of the fact that the energy deposited in the detector is higher when transition radiation is produced. This is due to the fact that all energetic charged particles deposit energy due to dE/dx, and only highly relativistic particles produce TR photons which deposit energy from photoelectric absorption. The total energy deposited in the detector is the sum of the energies from the two types of signals. Since only electrons (positrons) radiate TR at HERMES energies, they will have a higher total energy deposit in the detectors. The discrimination is based on a cut on the total energy. This is the method employed by the HERMES TRD. It has the advantage that much cheaper readout electronics can be used. Unfortunately, as can be seen in fig. 4.5, the energy distribution for dE/dX has a long Landau tail. This tail comes from a close encounter between the incident particle and a gas atom in which a large momentum is transferred to the electron ejected from the atom. This results in a much higher energy deposit in the detector

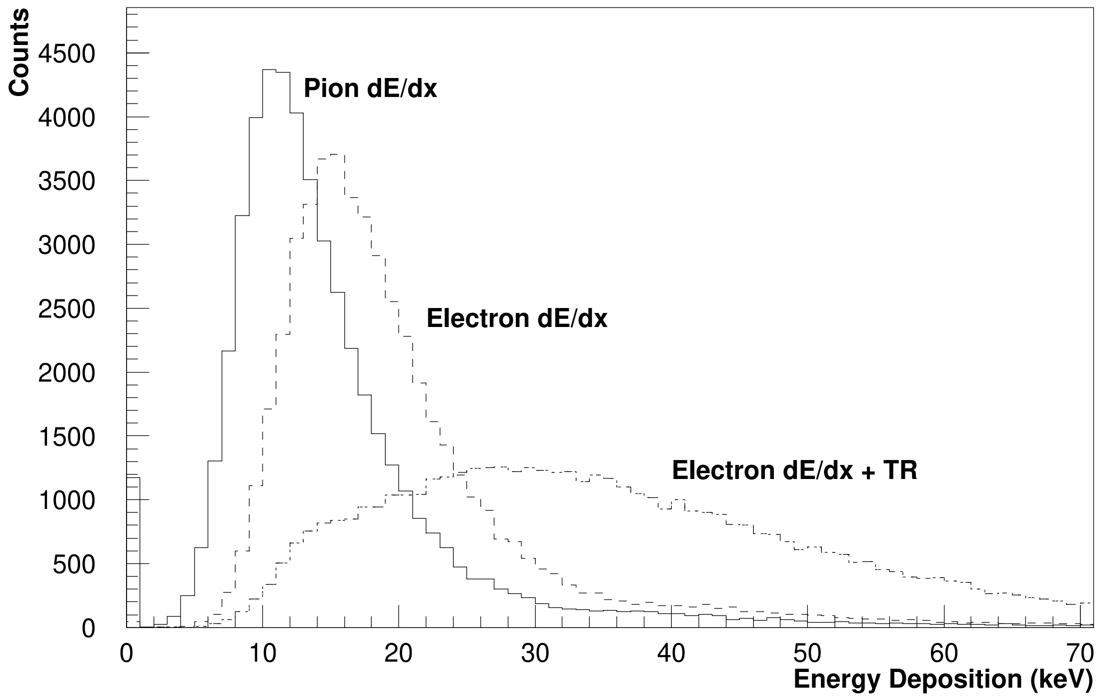

Figure 4.5: Typical TRD energy distribution from dE/dx and TR.[41] The dE/dx for the electrons is obtained by removing the radiator from the simulation. The mean of this distribution is higher than the mean for pions because of the relativistic rise in the energy loss.

and causes the detected energies from a non-radiating particle to extend well into the region of energy deposition of a TR radiating particle. However, by using multiple modules, and by analysing with the truncated mean method which is described in section 4.3.3, the radiating ($e^{\pm}$) and non-radiating ($\pi^{\pm}, K^{\pm}, \dots$) particles can be distinguished.

4.3 The HERMES TRD Design

4.3.1 Radiator

The ideal type of radiator would be a set of evenly spaced dielectric layers separated by vacuum at a distance given by the formation zone. The radiator material would need to have a high electron density and a low X-ray absorption. However, this is not practically achievable. It is extremely difficult to stretch the thin foils over a large area such that a narrow, uniform separation can be maintained. Also, the vacuum is replaced by a low density gas such as helium or nitrogen. A number of non-ideal radiator designs have been developed which still produce practical results.

One design, utilized by the Saclay D0 group,[42] is a set of polypropylene foils which are separated by a pattern of indentations embossed on them. The average gap between the foils is controlled by external pressure applied to the stack. A different design being developed uses a radiator foam. In this design, N_2 bubbles are produced in a material such as polyethylene. The bubbles act as the air gap, while the thin walls act as the radiator material. The spacing and orientation of the radiators is essentially random in this case, but the average can be arranged such that it conforms to the necessary formation zones. The advantage in this system is that the structure is rigid and self-supporting.

The HERMES TRD uses a loosely packed, pseudo-random arrangement of polypropylene/polyethylene fibers. The cylindrical fibers locally approximate the foil layers, and the material can be compressed such that the density produces an appropriate average spacing between the fibers. Tests were conducted at CERN on the various types of radiator designs using a prototype TRD. It was found that the performance of the fibers was competitive with the more ideal designs.[8] The cost and convenience of using the fiber material made it the most appropriate design.

The characteristics of the radiator were optimized for 5 GeV where the pion contamination is expected to be the most severe. The fibers have a diameter of 17–20

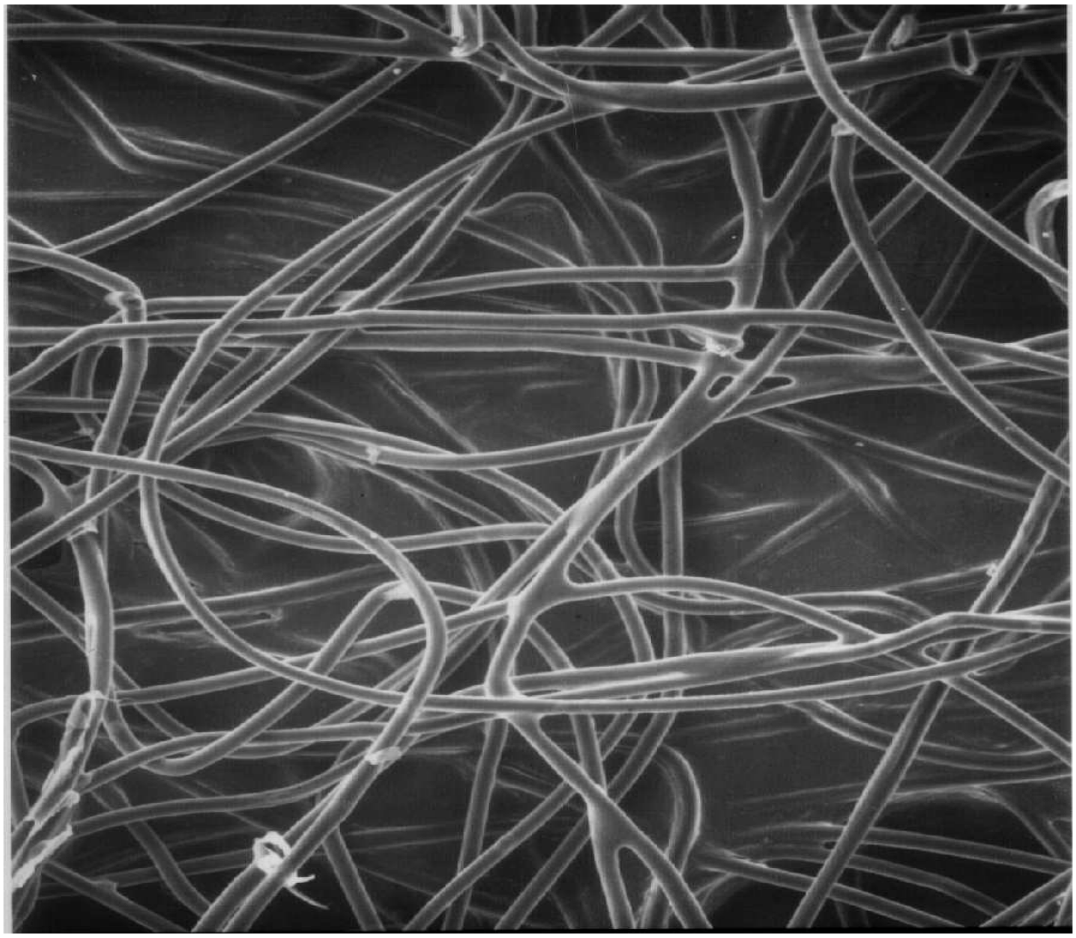

Figure 4.6: Scanning electron microscope picture of radiator fibers used in HERMES TRD. The diameter of the fibers is 17-20 μm.

microns. The fibre material is held in place with an aluminum frame and stitched together to maintain the proper density of 0.059 g/cm^3. The radiators are 6.35 cm thick by 3.4 m wide by 0.8 m high. This thickness corresponds to approximately 267 dielectric layers for each module. The optimum thickness of the radiator was limited by the X-ray self-absorption.[8] Also, hadronic showers would begin to occur with a thicker radiator.

4.3.2 Detector Gas

The choice of gas is particularly important in a TRD because the detector serves a dual role: both an X-ray and particle detector. For the detection of both types, the basic requirement is that the detector achieve significant avalanche multiplication that a detectable signal is produced. In order to efficiently detect TR, the absorption length must be small for the X-ray photons so that the probability of capturing them in the detector is high.

Avalanche multiplication occurs in noble gases at much lower fields than in more complex molecules.[39] This is due to the many non-ionizing energy dissipation modes available in polyatomic molecules. However, a detector made from a pure noble gas would have a gain of only 10^3–10^4 before entering permanent discharge operation. This is due to the fact that atoms excited during the avalanche can only return to the ground state through radiative processes. The emitted photons have energy above the ionization potential of any metal in the cathode. Also, noble gas ions which have migrated to the cathode are neutralized through the extraction of an electron. The de-excitation of the atom occurs through the radiation of a photon or by the emission of a secondary electron from the metal surface. In each case, this can produce a secondary avalanche shortly after the initial one. At even moderate gains, this can produce a continuous discharge.

The solution to this problem is to add a small amount of a polyatomic gas into the detector. Becuase of rotational and vibrational states added to the electron excited states, the molecular absorption spectrum appears as qausi-continuous bands instead of the discrete lines found in an atomic spectrum.[43] Thus, polyatomic molecules can absorb photons over a range of energy. For example, methane is very efficient at absorbing photons of energy in the range 7.9 to 14.5 eV.[39] Transitions to lower excited states can occur without radiation of a photon. Also, interaction with the noble gas ions tends to cause the charge to transfer to the molecule which has a lower ionization potential. De-excitation and neutralization of the molecules usually occurs without secondary emission. The radicals tend to dissociate into simpler molecules or polymerize into larger complexes, and excess energy is dissipated through collisions or dissociation. Thus, the good absorption of photons coupled with the suppression of the secondary emission allows for gains of up to 10^6.[39] The polyatomic gas is referred to as the quench gas. Most organic gases such as hydrocarbons and alcohols, and some nonorganic compounds like freons or CO_2 make good quench gases.

The choice of which noble gas to use in the detector was determined by the X-ray absorption properties. While cost considerations favour the use of argon over krypton or xenon as the standard gas for detecting charged particles, the properties of these gases for photoabsorption are quite different. As can be seen in fig. 4.2, the absorption length of a 10 keV photon is about 10 mm in Xe. However, it increases to approximately 60 mm in Kr and 100 mm in Ar. Given that the optimum thickness of gas in the detector is one absorption length, an X-ray detector using Ar or even Kr would be very long. Also, the fluorescence photons from the K-shell of Kr have a very good chance of escaping a 10 mm layer of gas while the L-fluorescence X-rays of Xe have only a 20% chance of escaping. Thus, the evidence leans heavily in favour of a Xe detector.

Various tests were conducted at TRIUMF to determine the optimal gas mixture for the HERMES TRD. Methane was found to be the best quench gas for the detector. Although a gas mixture containing hydrocarbons tends to be flammable, the only available non-flammable quench gas is carbon dioxide. However, CO_2 produces a detector response which is too slow to be practical. The addition of CF_4 to the mixture improves the speed of the detector, but it degrades the resolution. The use of CF_4 was left as an option in the design of the gas system, but the gas mixture being used in the HERMES TRD is 90% Xe and 10% CH_4.

4.3.3 Overall design

The HERMES TRD consists of 2 stacks of 6 modules each – one set above the beam and one set below – each consisting of a radiator and a proportional chamber. Surrounding the chamber on each module are flush gaps which reduce the amount of

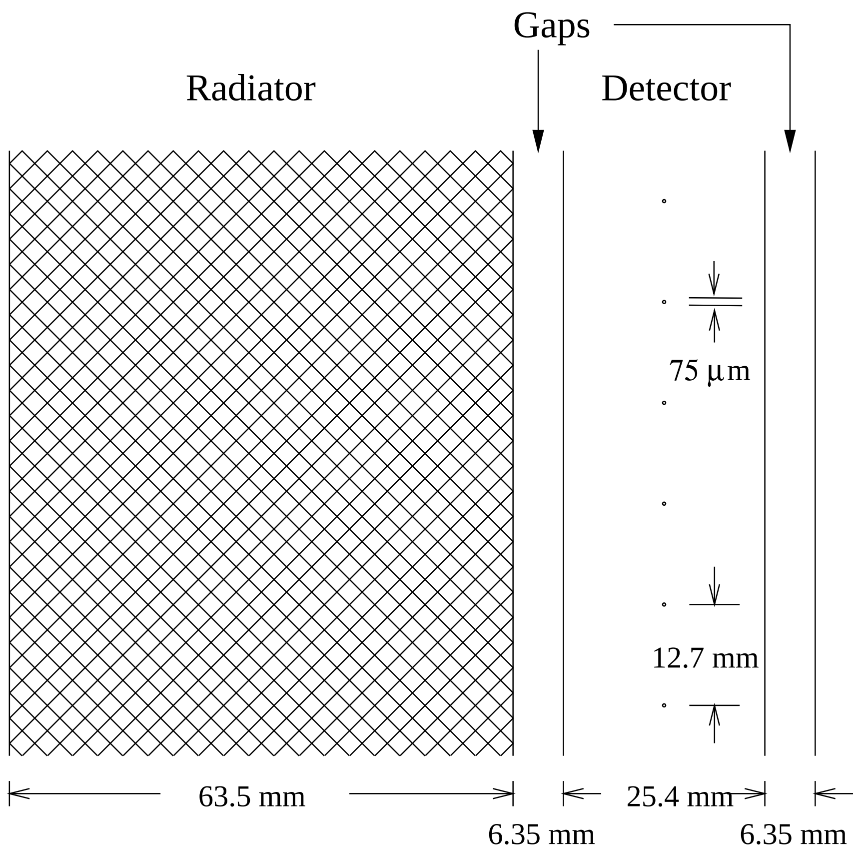

Figure 4.7: Schematic drawing of one TRD module (top view). The effective area of each module is 325×72 cm^2. The original dimensions were in inches. This module is repeated six times in each stack of the TRD.

impurities diffusing into it. The walls of the chamber and gaps are aluminized mylar foils; these are also the cathodes for the proportional chamber. A schematic drawing of one module is shown in fig. 4.7.

The energy distributions of pions and electrons from one module alone are not suitable for discrimination through the use of a cut on energy. One can see from fig. 4.8 that the Landau tail of the pion signal extends across most of the electron energy region. By increasing the number of modules to 6, one obtains multiple samples of the TRD response which can be combined into total energy distributions where e^+ and π are distinguishable. However, the Landau tail still reduces the effectiveness of an energy cut in yielding an adequate pion rejection factor (PRF).

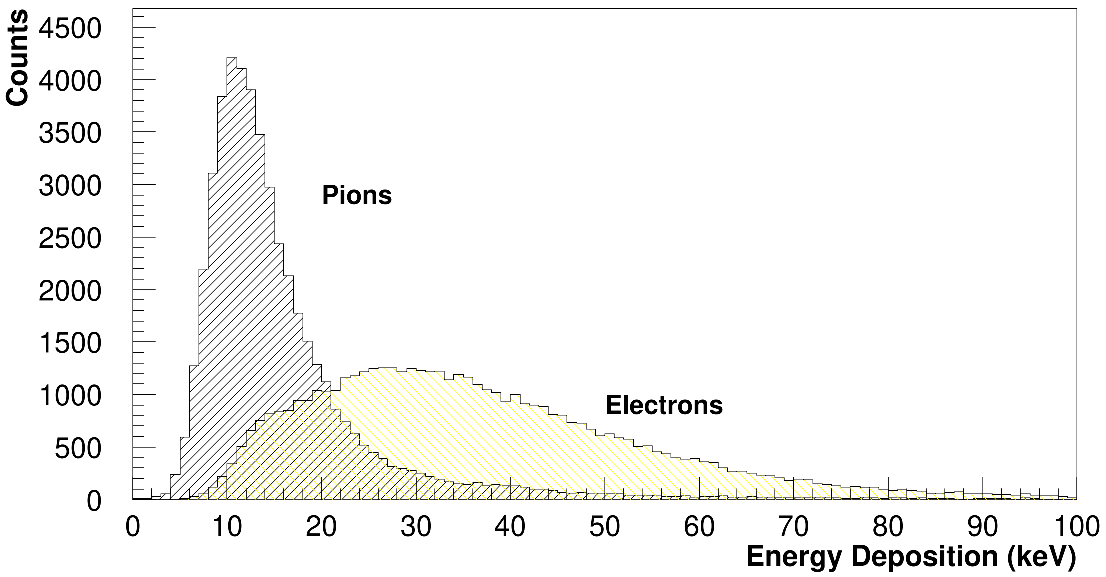

Figure 4.8: Energy distributions for pions and electrons in one TRD module. The spectra are obtained from Monte Carlo simulations for a single module of the HERMES TRD.[41]

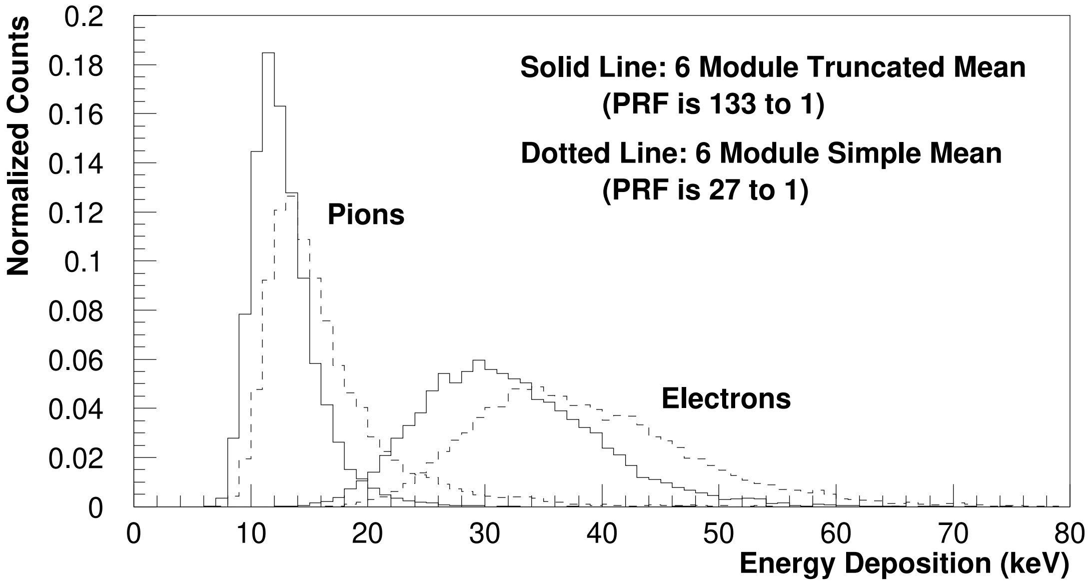

Figure 4.9: Energy distributions for pions and electrons in 6 TRD modules using both simple and truncated mean. The spectra are obtained using data from the TRD prototype tests at CERN.[41]

The method of analysis used to reduce the Landau tail is the *truncated mean*. In this method, the highest signal from the 6 modules is dropped from the sum. While this method decreases the mean energy of the signal for both $e^{\pm}$ and hadrons, the largest effect is on the high energy tail of the dE/dx signal, effectively removing events with large momentum transfer. This greatly reduces the overlap of the responses to $e^{\pm}$ and hadrons providing very good particle discrimination. As is shown in fig. 4.9 the pion rejection factor is increased from 27:1 to greater than 100:1 through the use of the truncated mean.

4.3.4 Gain stability

The required pion rejection factor can be achieved in the 6 module TRD using a cut on the total energy deposited. However, in order to maintain this PRF, the gain must be held constant. If it changes by more than a few percent, the distributions of pion and electron energies will be significantly shifted, and particle discrimination will not be effective.

The gain M for a proportional chamber is given approximately by eq. (4.24). Taking the derivative of this equation and of eq. (4.25) one obtains an expression for the relative change in gain with respect to changes in the distance between the cathodes:

$$\frac{\Delta M}{M} = \ln M \frac{\Delta Q}{Q} \tag{4.26}$$

$$\frac{\Delta Q}{Q} = \frac{Cl}{2\epsilon_o s}\frac{\Delta l}{l}. \tag{4.27}$$

Using the dimensions given in fig. 4.7 and a gain of 10^5, the relative gain change in the detector is

$$\frac{\Delta M}{M} = 0.4\ \Delta l \quad (l \text{ in mm}). \tag{4.28}$$

This corresponds to a 20% change in the gain when the distance between the cathode walls shifts by 1 mm. This value was obtained through some approximation, and actual numerical simulations of the HERMES TRD show that a change in cathode distance of 0.01 mm produces a 1% change in the gain.[44]

Other factors such as the spacing and diameter of the anode wires can also seriously affect the gain of the system. However, once the wires are installed, those factors are constant. The gain can be measured for individual wires and differences can be accounted for in the calibration. In the case of the cathode planes, the distance between them is not a constant. Changes in the differential pressure across the cathodes can cause them to shift significantly. In order to try to improve their rigidity, the cathode foils have been stretched to a high tension before gluing them to the frame. However, this does not eliminate the problem. Only by precisely controlling the pressure in the detectors can the cathode foils be held within tolerable limits.

The gas system for the HERMES TRD is very sophisticated due to the tight requirements on gain stability. The pressure must be controlled to one part in 10^5 in order to maintain the cathode separation stable to within 0.01 mm. The gas mixture must also be held constant and at high purity in order to prevent further fluctuations in the gain. The gas system is described in detail in the next chapter.

Chapter 5

The HERMES TRD Gas System

In a normal proportional detector, the signal is used to indicate the passage of a particle and its position. The exact size of the signal is not critical, only that it exceed a certain threshold. In this case, the specific value of the gain of the detector need only be constant to within 20–30%. However, in the case of a TRD, particle identification is based on the energy deposited and hence on the size of the signal. In order to identify the particle efficiently, this measurement must be accurate and requires a constant gain in the detector.

Control of the gas composition and pressure in the TRD is critical to maintaining a stable gain. Due to these requirements, the system for controlling the gas in the detector has a much more sophisticated design than for an average proportional chamber. The system must be able to control the various properties of the gas simultaneously in order to maintain the stable operation of the detector.

This chapter describes the gas system and its function in detail. The first two sections describe the requirements of the system and the strategy for fulfilling them. The next section describes the overall gas system, showing the route gas takes through it. The sections following that describe the main components of the gas system in detail and show data to demonstrate that they are satisfying the requirements.

5.1 System Requirements

One of the main considerations in the design of the gas system is the high expense of using xenon gas which costs over \$5/L. This requires that the gas be recycled in order to prevent the operational expenses from becoming astronomically high. In order to minimize the loss of Xe, all parts of the gas system and the detector were helium leak checked prior to operation. He leak checking is unusual for wire chambers because the gas is generally exhausted and losses or contamination due to small leaks are less important.

The pressure stability of the gas system is extremely important. Numerical simulations show that the differential pressure between the chamber and the gaps must be held constant to one part in 10^5 in order to maintain a 1% stability in the gain. A computer model of the chamber foils showed that their maximum deflection varies linearly with differential pressure between 0 and 2 mbar, with a 1 mbar pressure difference producing a 4.76 mm shift.[44] This indicates that a differential pressure of 10 μbar produces a foil shift of 0.05 mm. From eq. (4.28), this causes a gain change of 1%. While pressure control systems can achieve this level of stability, the system must also respond to atmospheric pressure. If the differential pressure with respect to atmosphere becomes too great, damage to the outer foils can result from the stress. Thus the differential pressure must remain constant while the total pressure tracks atmospheric pressure.

Unfortunately, the gain also depends on the absolute pressure in the detector.[39] Thus, the gain tracks atmospheric pressure as shown in fig. 5.1. While absolute pressure can be held constant in the chambers in principle, the foils would be damaged due to large values of the differential pressure between the detector and atmosphere. Therefore, it is necessary to record the system pressure so that this pressure dependence can be corrected in the analysis.

The constituents of the gas mixture can also strongly affect the gain. The chosen gas mixture is Xe/CH_4 with a ratio of 90:10. The gain is quite sensitive to changes

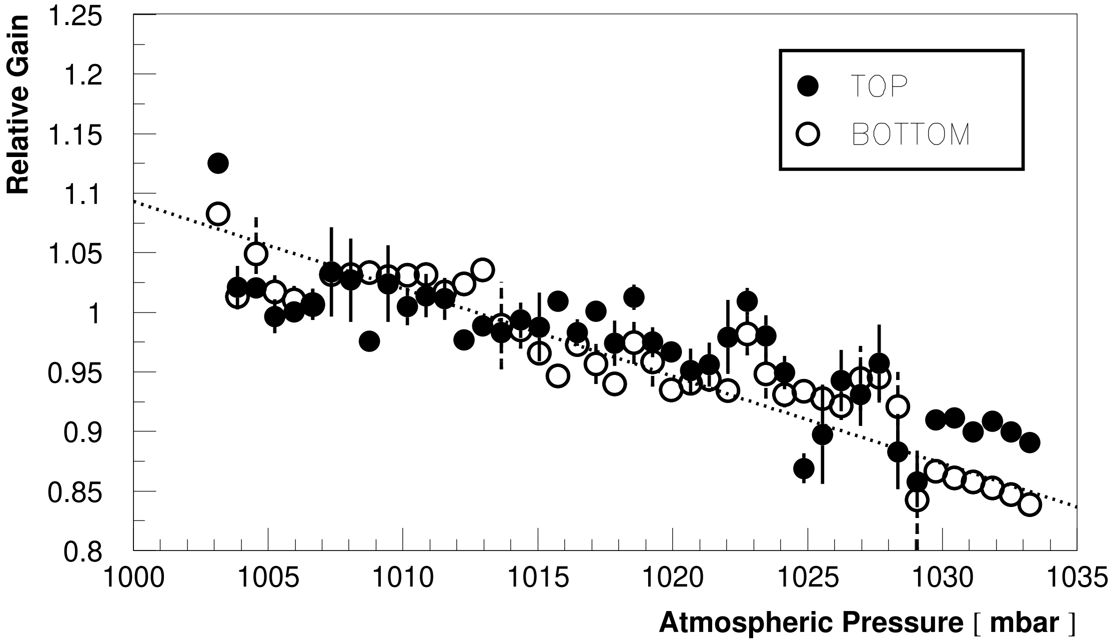

Figure 5.1: Variation of gain with atmospheric pressure.[45]

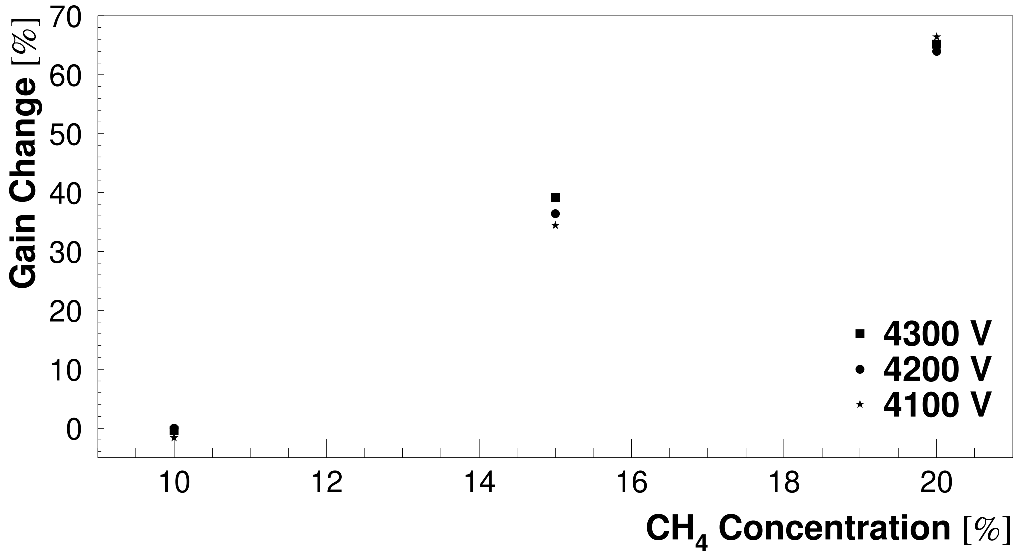

Figure 5.2: Variation of gain with fraction of CH_4 present.

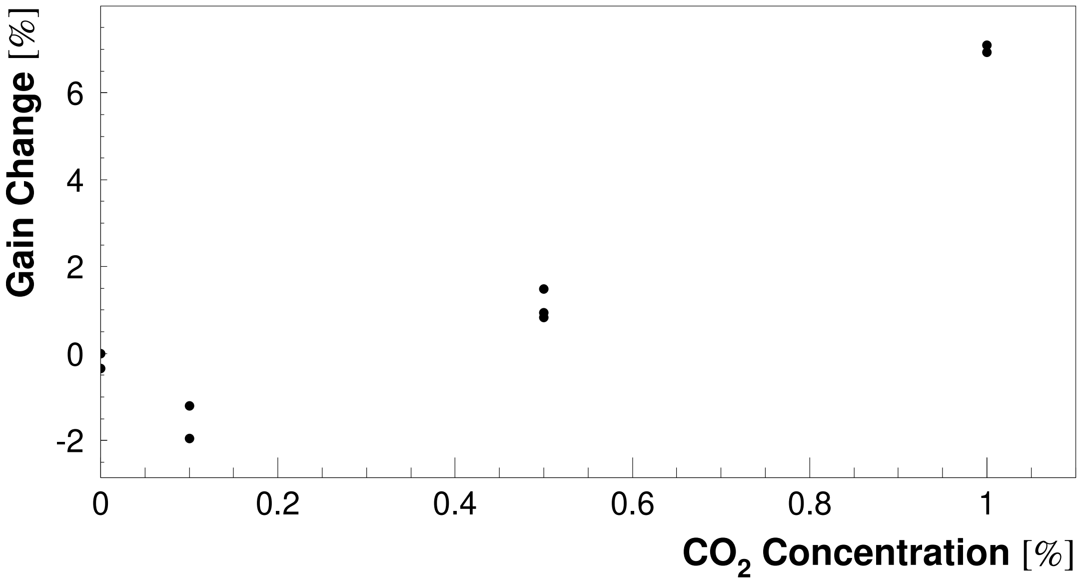

Figure 5.3: Variation of gain with fraction of CO_2 present.

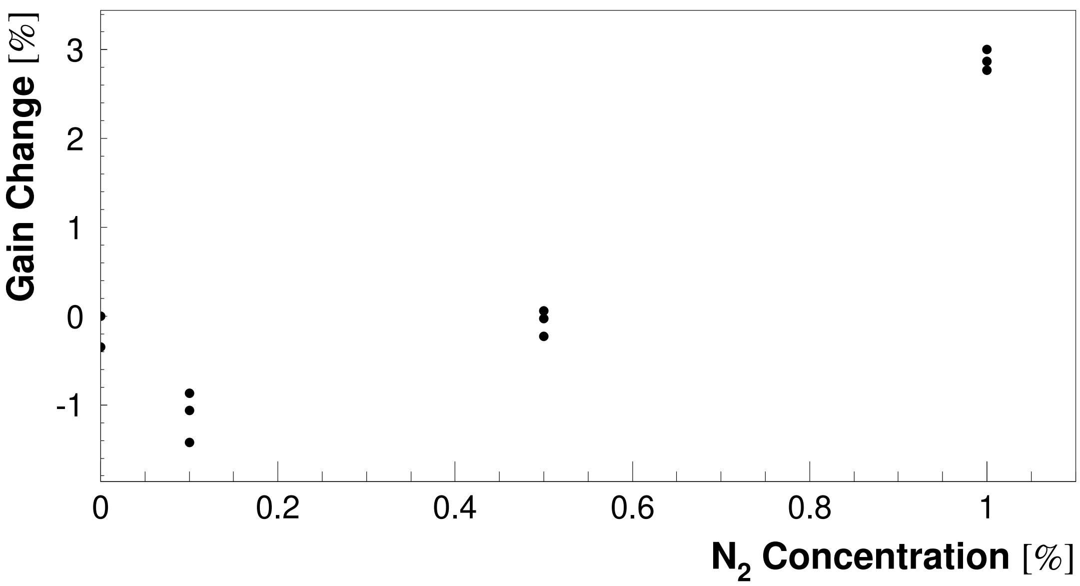

Figure 5.4: Variation of gain with fraction of N_2 present.

in this mixture as can be seen in fig. 5.2 which was obtained from tests conducted at TRIUMF.[46] For gain stability at the 1% level, the system must be able to maintain the ratio of Xe to CH_4 to within approximately 0.15%.

Air can diffuse through the foils of the chamber; thus impurities in the gas mixture can develop from gases such as N_2, O_2, H_2O, Ar and CO_2. Given that the gas in the system is recycled, there must be an efficient purification system in order to reduce the amount of impurities to a tolerable level. Any of these impurities has a significant effect on the gain. They can change the behavior of the quench gas, and an electronegative gas such as water vapour or oxygen will absorb the secondary electrons as they drift toward the anode which greatly reduces the signal produced. Figs. 5.3 and 5.4 show data from the TRIUMF gas tests which demonstrate that contamination of 0.1-0.2% changes the gain by 1%. Also, given that the impurities enter by diffusion through the cathode foils, the gas must be continuously flowed through the system. In this way, impurities cannot build up in the chamber; they will be flushed out and removed by the purifiers.

Thus, there are three major requirements that must be fulfilled by the gas system to stabilize the gain at a 1% level:

- Differential pressure stability to better than 10 μbar,
- Maintaining the Xe/CH_4 ratio to within approximately 0.1–0.2%,
- Control of impurities to 0.1–0.2%.

5.2 General Strategies

This section will give the details on the strategy used to fulfill the requirements. It will outline the type of components used and explain their function in the overall system.

On each side of the proportional chambers are 6.35 mm gaps which contain a continuous flow of carbon dioxide. These gaps play an important role in reducing impurities in the detector. By surrounding the detector with these gaps, air that might diffuse through the outside foils of the TRD module is swept away in them. The choice of CO_2 as the flush gas is due to the fact that it does not significantly absorb X-rays and can be easily removed from the Xe/CH_4. Also, it is cheap, so it can be exhausted without producing an unreasonable operating cost. Thus, although the CO_2 will diffuse into the chamber, it's effect can be easily minimized. Also, to reduce the amount of diffusion, the aluminized mylar foils are twice as thick as those in a standard detector. The drawback of the gaps is that the pressure control is complicated by the additional gas volume between the proportional chamber and atmosphere.

The gas system is divided into two major components: detector and gap. The 'detector' in this case refers to the proportional chamber in each TRD module. The designs of the two parts are very similar. The major difference is that the detector system recycles the gas while the gaps exhaust it; thus, there are no purification units in the gap system. Also, since the gas in the gaps is pure CO_2 there are no facilities for mixing gases. However, control of pressure and flow are essentially the same.

Differential pressure is held constant at the foils between the detector and the gap and between the gap and atmosphere. The pressure is regulated by a proportional-integral-differential (PID) controller which can efficiently maintain the system at the setpoint and quickly correct any deviations that might occur. A separate controller is used for the detector/gap (D/G) and the gap/atmosphere (G/A) differential pressures. The pressure inside the gap is controlled to track changes in atmospheric pressure, and the pressure in the detector follows the changes in the gap. The detector is set to respond quickly to any changes in gap pressure. Thus the deviation in differential pressure is quickly reduced. On the other hand, the gap responds slowly to atmospheric changes. This allows the detector to correct easily for gap changes with minimal overshoot of the setpoint.

The system has a continuous flow of gas in order to flush out impurities. The pressure in the detector and the gap is controlled by changing the flow rate into the chambers. The flow out of the chambers is set to a constant rate, and the input is controlled by the PID's. By changing the input flow relative to the output, the pressure in the chamber is adjusted to produce the correct differential pressure. The continuous flow through the system is produced by pumps located at the output of the detectors and the gaps.

Because Xe is a very dense gas, the pressure in the chamber changes significantly with height. The density of Xe is 5.89 g/L which produces a 570 μbar change in pressure per metre. Given that the chambers have a height of 72 cm, there is a large shift in differential pressure between the top and bottom of the chambers. This causes the cathode foils to be pushed outward on the bottom resulting in the cross section of the detector becoming roughly pear shaped. In order to reduce this effect, the foils were stretched to a tension of 1.8 kg/cm before gluing to the detector frames. This tension was used in the computer modeling of the chamber mentioned in the previous section. Given that the foils are fixed at their outer edges, the maximum deflection will occur at the centre of the foil. A good approximation for the shape of the foil under a uniform pressure difference is a parabola:[47]

$$x = (4.76\frac{mm}{mbar})P\left[\frac{(y-36cm)^2}{1296cm^2}-1\right] \tag{5.1}$$

where P is the differential pressure. The static pressure produced by the density ρ is given by

$$P = \rho g y \tag{5.2}$$

where y is the height in cm of the gas column, and g is the Earth's gravitational acceleration. The change in differential pressure between the detector and the gap is found by subtracting the pressure produced by the static column of CO_2:

$$P = (\rho_{Xe} - \rho_{CO_2})gy. \tag{5.3}$$

Substituting eq. (5.3) into eq. (5.1) yields an equation to describe the shape of the foils:

$$x = (1.82 \cdot 10^{-3})(y - y_0)\left[\frac{(y-36)^2}{1296} - 1\right] \tag{5.4}$$

where y_0 is the point along the foil at which the differential pressure is zero.

Depending on the location of y_0, the shape of the foil can vary considerably. If the differential pressure across the foil is zero at the top of the chamber, it will have a maximum deflection of 0.8 mm, 48 cm from the top. If the pressure in the detector is set such that the differential pressure with respect to the gaps is zero at the halfway point of the detector, the maximum deflection is reduced to 0.25 mm at points 15 cm away from each edge. These calculations are based on an approximate model of the detector, and thus are not entirely reflected in the real TRD. In order to correct the data for the y-dependence of the gain, it is necessary to use a fifth order polynomial.[45]

The TRD is divided into two halves: above and below the beamline. Correspondingly, the pressure control is split into top and bottom components. This allows the pressure in each half of the detector to have separate setpoints in order to correct for the static pressure difference resulting from the difference in vertical position of the two halves. The setpoints for the detectors account for the fact that the pressure transducers are not at the same height as the centre of the detectors, and are calculated to produce a differential pressure of zero at centre.

In order to have sufficient gas available to increase the pressure in 12 separate chambers, a large buffer tank is installed before the flow controllers at the input to the chambers. Given that atmospheric pressure can fluctuate by up to 10%, the buffer volume must be able to contain enough gas to compensate for this. The volume of the detectors and related pipes is roughly 800 L. To lower the pressure in the chambers by 50 mbar at atmospheric pressure, approximately 40 L of gas must be removed. The large buffer allows the extra gas to be stored without having a large overpressure in the pipes. This reduces any potential problem of leakage at high pressure. Also, by positioning the buffer by the input to the chambers, extra gas can be added quickly when the pressure needs to be raised.

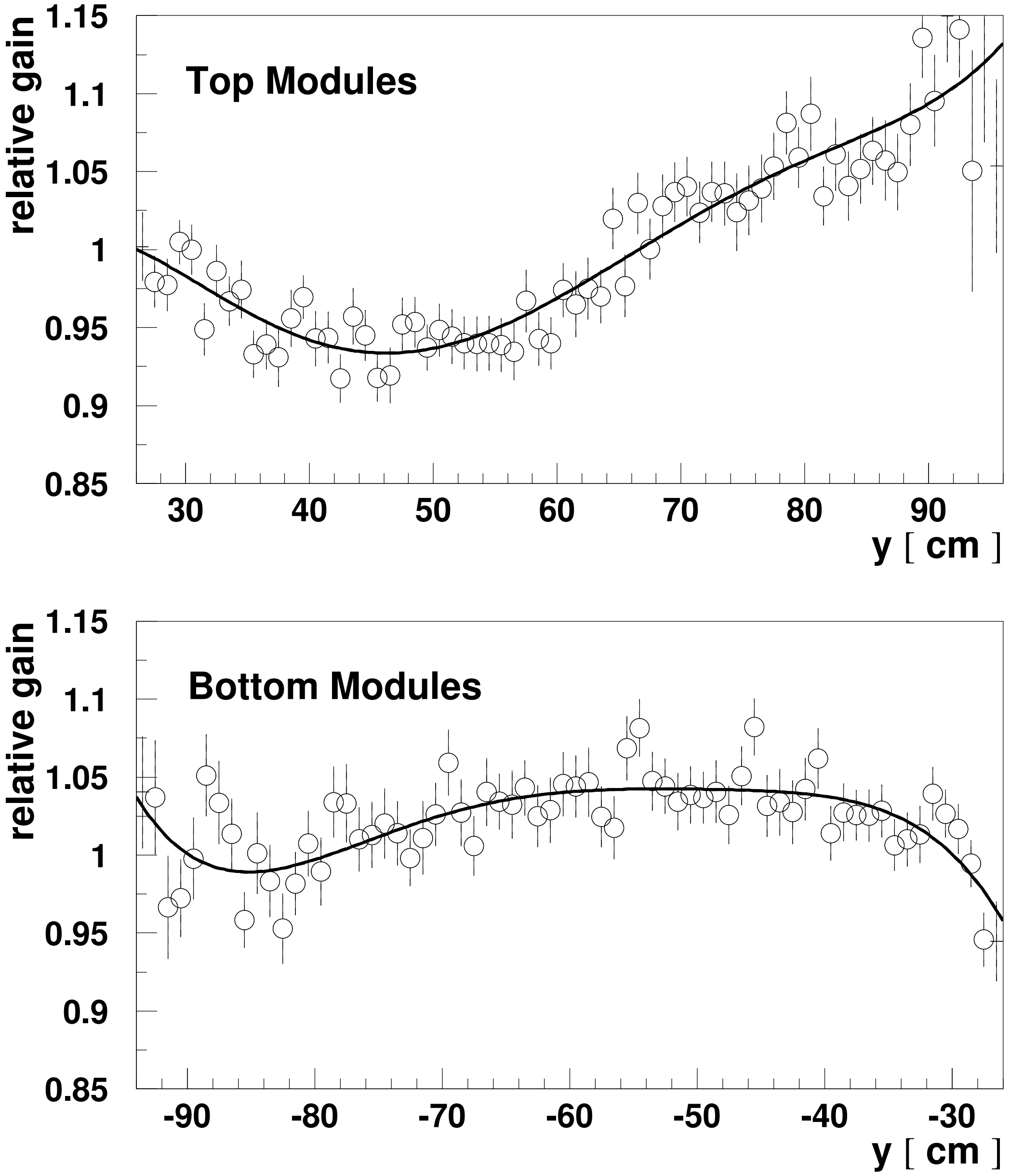

Figure 5.5: The gain of the TRD vs. height for the top and bottom chambers. The top chamber shows the pear shape characteristic of having the zero differential pressure point significantly off-center. The bottom detector shows far less deviation from the average gain which indicates proper centering of the zero ΔP point. This plot is obtained from actual HERMES data during the 1995 run.[45]

The composition of the gas mixture is analyzed by a quadrupole mass spectrometer (QMS). This shows the level of impurities as well as the ratio of xenon to methane. If the ratio has shifted, small flow controllers on the pure gas supply lines can be opened to restore the proper mixture. The QMS readings also show when the impurity level rises significantly. This would indicate that the purifiers have become saturated and need changing or that a leak has developed.

There are two main types of purification units in the system: a membrane gas separator (MGS) and molecular sieves. The MGS operates by creating a vacuum outside of the thin walled tubing through which the gas is flowing. Due to the differences in permeabilities of various gases, they pass through the membrane at different rates and some separation of the gas mixture occurs. The sieves are small pellets of specialized material which readily absorb certain gases; two types are used in the gas system. The first consists of a material which efficiently absorbs small molecules such as H_2O and CO_2. The other absorbs O_2 through an oxidation reaction. The sieves become saturated over time and need to be regularly regenerated.

Virtually all units in the gas system are controlled electronically. All analog data from the various readouts and digital data on the status of valves, etc are sent to a programmable logic controller. The program in this unit evaluates the data and adjusts the various controllers to maintain the proper operating conditions.

During the initial fill of the detectors, the gas in the complete system, including the detectors had to be changed from air to Xe/CH_4. This was accomplished by first purging the entire system with CO_2. As the Xe/CH_4 was added, the system was set in closed loop operation to prevent any Xe losses. The MGS was used to remove the large quantity of CO_2 as the Xe/CH_4 was added to the system. The MGS is useful for reducing the CO_2 level to a few percent over several days. After that, the sieves are added into the system to pull out the remaining CO_2. The gas mixture is then virtually pure Xe/CH_4, and the system operates under standard conditions.

5.3 System Overview

Due to the layout of the experimental area, and for safety reasons, the gas system is divided into two main sections. Beside the HERMES detector, located outside of the concrete which shields radiation from the beamline, is a large trailer containing the electronics and readout units for the entire HERMES spectrometer. This room is referred to as the 'electronics trailer.' The systems for controlling the gas to the various detector components are on the roof of the trailer which is located approximately 5 stories underground at the level of the HERA beamline. At ground level is the gas supply area referred to as the 'gas house.' This area contains the main gas supply bottles for the HERMES detectors. Given that the bottles are at high pressure and can contain flammable gases, they are housed in specially shielded and grounded rooms to prevent accidents. The gas mixing components of the system are located in the gas house.

5.3.1 Detector

Gas House

The pure gases are supplied in standard, commercially available high pressure bottles. The gas enters the system through mass flow controllers which allow up to 10 L/min. The ratio of gases in the mixture is set by slaving the CH_4 mass flow controller to that of the Xe such that the flow rates are the correct percentage of the total flow. The system provides the means for producing a mixture of $Xe/CH_4/CF_4$ also. This mixture with a ratio of 90/5/5 was being considered during the design of the TRD. It produces a faster response of the detector, but the energy resolution is poorer. The flow controllers are opened when the pressure in the main buffer drops below its lower setpoint. There are also small mass flow controllers on the main input lines which allow only 20 mL/min. These are used to add small amounts of Xe or CH_4 in order to adjust the mixture.

Gas exiting the flow controllers enters the main line of the gas system. This line leads down to the electronics trailer and the detectors and is part of the recirculation loop. Immediately after the input flow controllers is a gas mixing tube. It contains multiple baffles along its length to ensure a turbulent flow which fully mixes the gas inside the tube. The membrane gas separator is located on the return line from the detectors in the gas house. Returning gas can pass through the MGS for purification. The return line can be exhausted to atmosphere or it can be set in the recirculation system by changing a couple of valves. When recirculated, the returning gas passes through the mixing tube.

The QMS is also located in the gas house. The gas system is configured such that the QMS can be placed into the line in three different locations. It can be located on the input lines to analyze the gas being supplied to the detector or in the return line to examine the impurities. It can also be placed immediately after the MGS to analyze its effect on the gas mixture. Given that the MGS draws out Xe or CH_4 as well as impurities, it is necessary for the QMS to analyze the gas exiting the MGS to determine whether the mixture needs to be adjusted. In the closed loop system when the membrane separator is off and no gas is being added, the three positions of the QMS are essentially equivalent.

Electronics Trailer

Gas leaving the gas house system travels down approximately five stories to the electronics trailer gas racks. The first component here is the 200 L buffer. Upon exiting the buffer, the gas flows through the sieves which are held in 2 L cylindrical containers with a diameter of approximately 10 cm. Given that they can become saturated, there are two containers of sieve material installed. The gas can be separately routed through either of them. This allows for one to be removed and regenerated while the other remains operational. There is also a bypass which allows the gas to pass without purification if the need arises. An oxygen analyzer is located at the output of the sieves to monitor its removal.

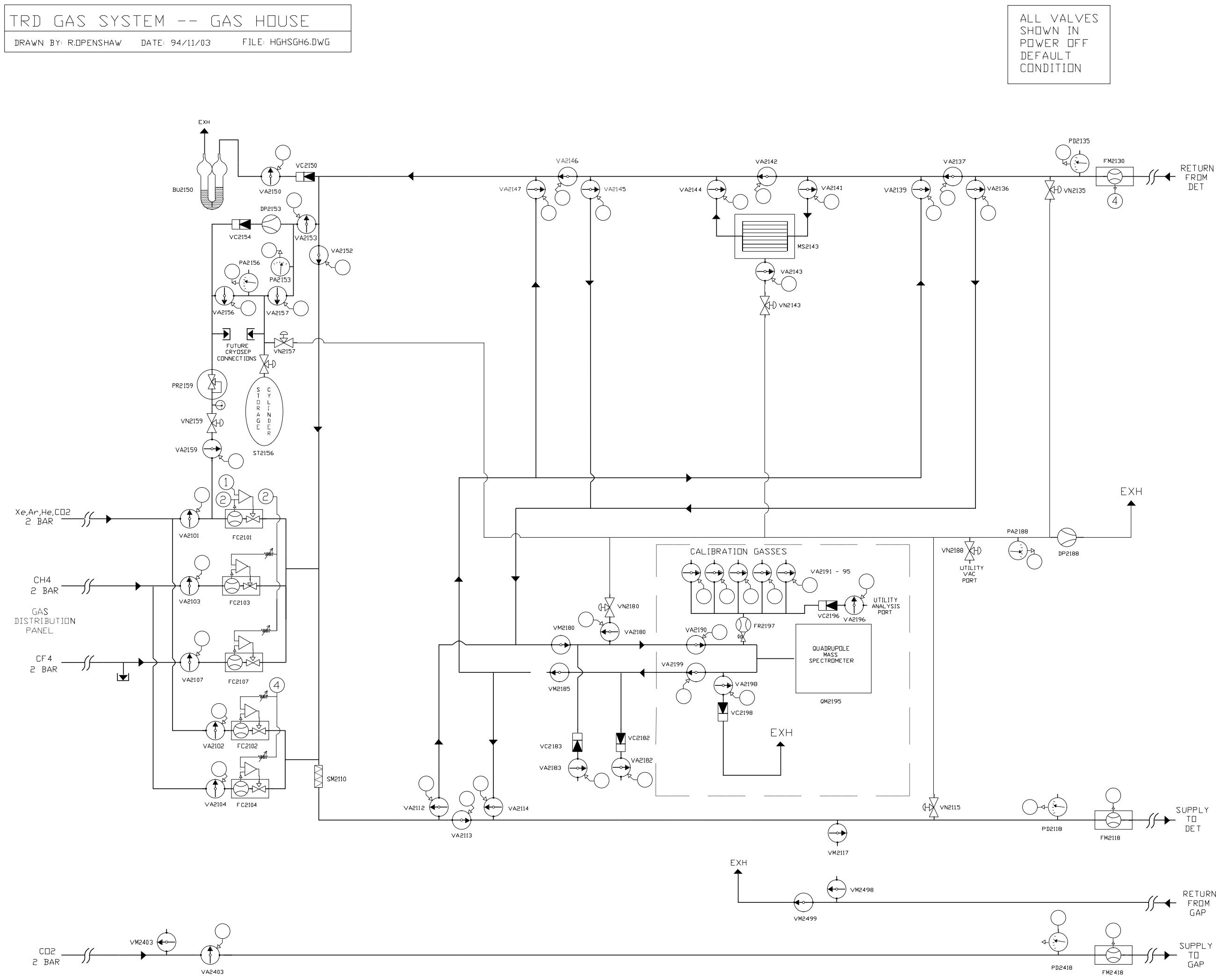

Figure 5.6: Schematic drawing of the gas house section of the gas system. A list of the part names is provided in appendix A.

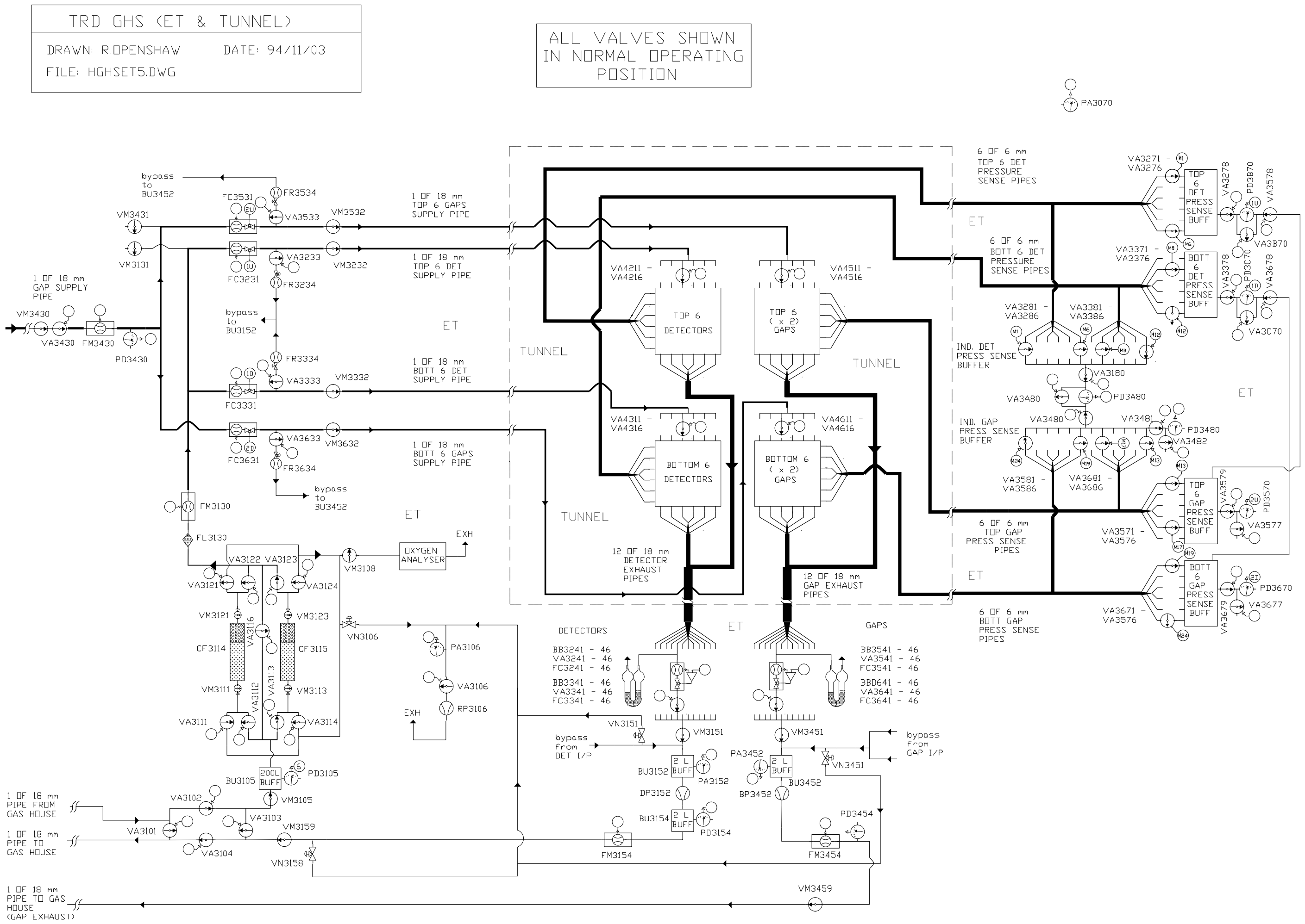

Figure 5.7: Schematic drawing of the electronics trailer section of the gas system. A list of the part names is provided in appendix A.

After passing through the sieves, the gas is split into components leading to the top and bottom modules. The components on both gas lines are exactly the same, but it is necessary to have separate control of top and bottom pressures to compensate for the static pressure column of Xe. The supply to each half is through one large pipe. At the detector, the gas flows into a manifold with six exit tubes to distribute the gases to the six detector modules.

The flow to the detectors is controlled by a single, common mass flow controller. This in turn is controlled by the PID controller. Readings of the average differential pressure between detector and gap are sent to the PID which adjusts the input flow to control the pressure in the detector.

The flow of gas out of the detector modules is controlled through an individual mass flow controller for each module. This output flow remains constant during the operation of the gas system. Changing the flow rate affects the pressure control of the system since increasing the output flow will require that gas be added at a faster rate in order to raise the pressure in the chamber. The output flow on each module is individually controlled in order to correct for minor differences in the impedance of each chamber. Given that the gas is input to the 6 modules at the same rate, adjusting the output flow rate for one will change the total pressure in that module. In this way, one can assure that the differential pressure is the same in all 6 modules.

Connected to each of the 12 return lines from the TRD is a bubbler which is a U-shaped glass tube filled with a small amount of oil. These provide a release in case of serious overpressure in any of the chambers. One side of the bubbler is connected to the return line, and the other is open to air. Thus, the bubbler acts as a manometer. As pressure increases in the lines, the oil gets pushed up the far side of the tube. If the pressure exceeds a certain value which is determined by the quantity of oil in the bubbler, the gas will bubble through the oil and be released to the atmosphere. In order to prevent the flowing gas from drawing the oil into the return lines because of the Venturi effect, an extra volume is introduced into the lines through which the bubblers are connected. This reduces the speed at which the gas travels past the opening to the bubbler and diminishes the drop in pressure due to the flowing gas. The bubblers are provided as a simple, hardware protection in case there is a problem which the control system fails to correct.

There is also a bypass for each half of the detector which allows the gas to move through the system without entering the detectors. A separate bypass is provided for the top and bottom halves. This allows one set to be shunted for service or testing while the other half remains unaffected. Rotameter style flow controllers control the flow rate through the bypasses.

The 12 gas lines are recombined with the bypass into a single pipe and sent to a compressor which can produce over 3 bars of pressure at the output, and maintains the flow of gas around the system. It produces a lot of vibration which can affect the readings in the system. To reduce this effect, the pumps rest on vibration dampers. The pipes connecting to the pumps are plastic in order to absorb the vibration in the plumbing. Gas exiting the pump flows back up to the gas house to be recycled.

5.3.2 Gaps

The design of the gaps is very similar to that of the detector. The main difference is that there are fewer components on the gap system because of the reduced requirements in performance. Only pure CO_2 is flowed through the gaps, so there is no need for any mixing units. Given that all the gas is exhausted, there are no recycling loops or purifiers. Also, given that CO_2 is cheap and non-flammable, there is much less significance on any leaks in the system.

CO_2 is supplied by a high pressure bottle in the gas house and enters the system through a mass flow controller. From there, the gas flows directly to the electronics trailer. There is no buffer in the gap system. The strategy of having extra gas in the lines in case of rises in atmospheric pressure is still used for the gaps; however, the extra pressure is simply stored in the gas lines. There are two main reasons why the buffer is not necessary in the gap system. First, because leaks out of the system are not of major significance, the gas lines can be kept at a higher pressure without concern. Second, because the gas is exhausted, any extra gas dumped out of the chambers due to a drop in atmospheric pressure need not be stored in the system. The pressure is maintained in the input lines by opening the flow controller at the supply bottle when it drops below the given setpoint. The supply flow is shut off when the pressure has been restored to the upper setpoint.

The gas flow into the chambers is split into top and bottom. There is only one input gas pipe to each half of the TRD, and the gas is split six ways when it reaches the chambers. Given that there is a gap on each side of the detector, the gas line to the gaps in each module is split in two just before entering the chambers. It is also recombined immediately after leaving them. In all aspects, the pair of gaps on each module is treated as a single unit.

The pressure is controlled by PID's exactly the same way as in the detectors. The differential pressure between the gaps and atmosphere is measured and the flow into the gaps is adjusted to maintain a constant pressure difference. A separate PID is used for control of the top and bottom halves of the TRD. The value of the gap-atmosphere differential pressure in each half is set such that the absolute pressure in the top and bottom detectors is equal.

The flow of gas returning from each module is controlled by a separate mass flow controller. There is also a bubbler on the return line from each module. This protects the outer windows of the gap as well as the cathode foils. As with the detector bubblers, they are between the return lines and the atmosphere. After the flow controllers, the 12 return lines are recombined.

The gas flow can also be made to bypass either top or bottom modules. The flow rate is controlled by rotameter flow controllers. After the bypass, the gas line is recombined with those returning from the modules. The gas is then input to a compression pump which maintains the flow through the gap system. The pump pushes the gas back up to the gas house where it is exhausted to atmosphere.

5.4 Pressure Measurement and Control

5.4.1 Pressure Measurement

The pressure in the detectors and the gaps is measured through a pressure sense line from each gas volume. These lines have essentially no flow and are present only for the purpose of the pressure measurement. The right side of fig. 5.7 shows the schematic of the pressure readout. The six sense lines from a set of chambers all lead into a single manifold in which the pressure is measured. The top detector and top gap manifolds are connected across a high accuracy pressure transducer where the differential pressure is measured. The differential pressure between the bottom detector and gap is measured by a second high accuracy transducer in the same manner. Each gap manifold is also connected to a pressure transducer measuring the gap/atmosphere differential pressure. These transducers are significantly less accurate than the ones used to measure the detector/gap pressure. The readings for differential pressure obtained in this manner are average pressures from the 6 chambers which are sufficient for detector operation. These values are input to the PID's as well as read by the slow control system.

The differential pressure from each individual module is also measured by a third set of pressure transducers. For this purpose, all 12 detector sense lines are connected to a single manifold as well as to the two separate manifolds for the top and bottom described above. The gaps are connected in the same fashion. The input of each sense line to either manifold is controlled by a solenoid valve. The slow control program controls the valves such that the sense line from only one detector at a time is open to the common manifold. At the same time, the gap sense line from the same module is open to its common manifold. These two are connected across the pressure transducers in the same manner as above. Thus, the pressure reading from the third set of manifolds measures only the differential pressures from a single module. The slow control program cycles through all 12 modules one at a time to provide readings for each one. At the time that the pressure is being read for a particular module, it is removed from the average pressure measurement. This is to prevent gas from flowing from one manifold into the other and causing inaccurate pressure readings. The individual pressure readings are only sent to the slow control system and not used in the pressure control loop. They are used to double-check that all 6 chambers on the top or bottom are behaving in a similar way. If one was found to be slightly out, then the output flow to that chamber could be adjusted to bring it back in line.

This pressure multiplexing system works quite well to measure the individual pressures of the modules. However, the cycling of modules must be done at a slow rate in order to allow the transients to disappear between each pressure change. The rate of change from one module to the next can be adjusted by the computer, and is set to 10 seconds per module. Thus, the pressures for the entire system are read over a two minute period. The data displayed in fig. 5.8 show the pressure in the first top and bottom detector modules. The pressure in the manifold is not the same for these two modules due to the different differential pressures in the top and bottom. Except for the occasional spikes on each graph, the data show that this system of pressure multiplexing is effective. The spikes are related to the subroutine which writes the measurements to disk and are not an indication of a problem with the actual pressure. The data logging routine merely saves the current readings at a set frequency. Given that the pressure takes a few seconds to change between the two values, if the transducer reading is saved during this period, the reading will be incorrect. More detail on this subject will be given in a later section.

The pressure and flow rate of the gas are also measured at several other points throughout the system. They are measured at the input and output to the gas house and electronics trailer to monitor the flow through the loop. The pressure of the main buffer is also monitored to assure that there is sufficient gas in the system. The pressure is measured at the input and output of the compression pumps. Given the vibration of the pumps, the pressure readings close to them can be badly affected. To reduce this problem, the pressure transducers close to the pumps are placed on 2 L buffer volumes. These buffers greatly reduce the fluctuations in pressure.

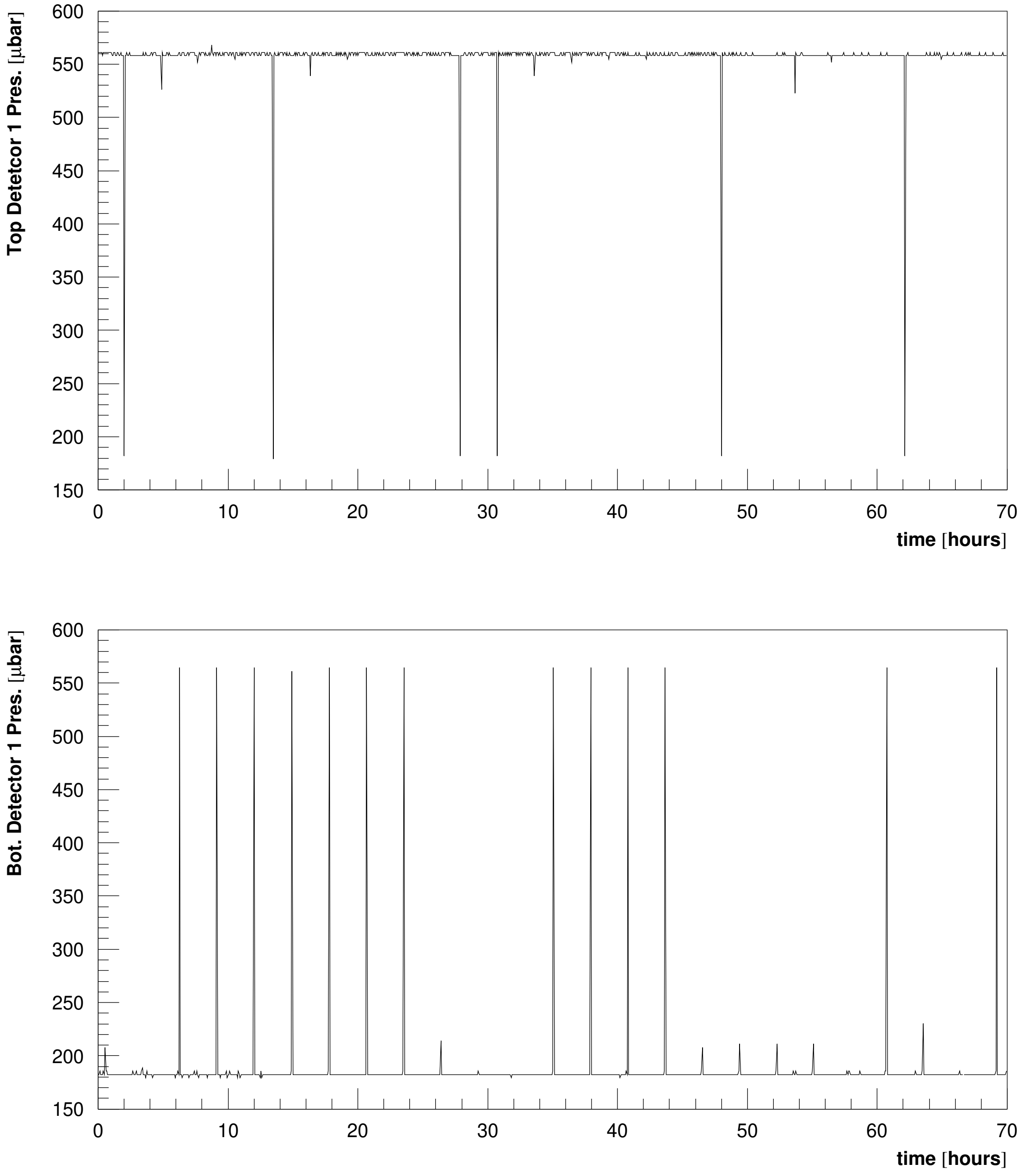

Figure 5.8: Individual pressure readings from the first top and bottom detector modules; both of which are measured by the same pressure transducer. The spikes are a result of the timing of the data logging program which occasionally saves a data point while the pressure in the transducer is changing.

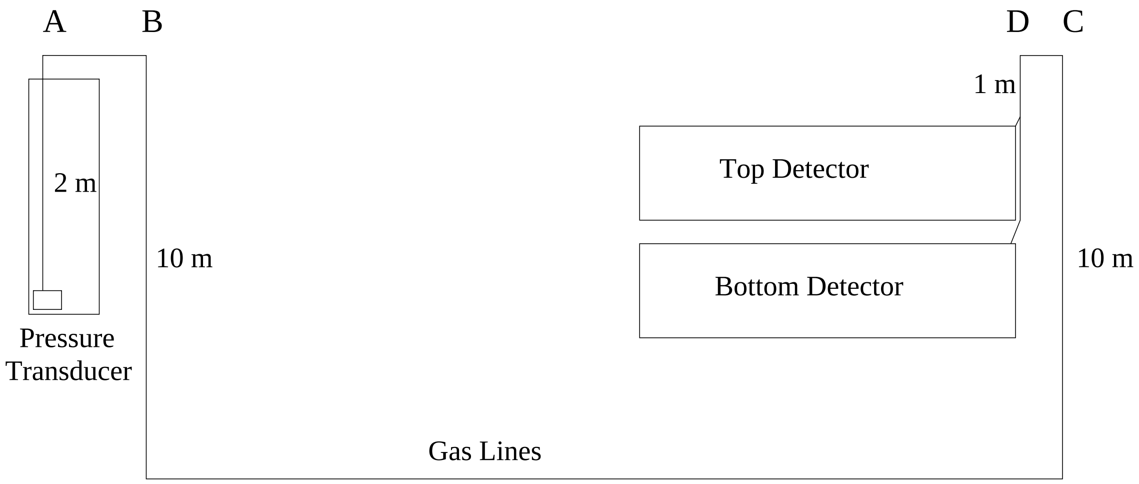

Figure 5.9: Sketch of the gas lines between the TRD and the gas system. The labels A-D correspond to the vertical sections of pipe. This drawing is not to scale.

Because the gas in the pressure sense lines is static, the lines must be purged out when the gas is changed. In order to have an accurate reading of the differential pressure, the sense lines must contain the gas currently in the system. Due to large changes in height along the sense lines, gravitational effects are very significant. If the gas in the lines is uniform, the effects cancel out. However, if the gas at one end is different, the pressure can change dramatically. For example, if the last 2 m at the gas racks – section A in fig. 5.9 – contains CO_2 while the rest of the line contains Xe, the measured pressure would be affected by:

$$P = \rho_{CO_2} g h_A - \rho_{Xe} g (h_B - h_C + h_D) = -378 \mu bar. \tag{5.5}$$

The purging of the sense lines is done by connecting a vacuum pump at the pressure transducer. The old gas in the sense line will be drawn out and replaced by fresh gas coming from the chamber. A bypass valve across the transducer has been installed to prevent damage and to allow the removal of gas from both sides.

5.4.2 PID Controllers

The pressure control for both the detectors and the gaps is done by PID controllers. These provide a smooth steady-sate control as well as fast response to deviations. They are able to restore the system to its setpoint quickly and with a minimal overshoot. An analogy is that of a critically damped oscillator. As the oscillator deviates from its equilibrium position, a restoring force is produced. Without damping, the system will oscillate. If the damping is too great, the system will take too long to reach equilibrium. Unlike the oscillator, the setpoint for the pressure is not an equilibrium point. The system will not remain at the setpoint unless stability is maintained by the controller. Given that the differential pressure across the foils is potentially the most unstable aspect of the system, the accurate and fast control of the pressure is very important.

PID stands for proportional-integral-differential. This represents the aspects of the error signal which are included in the control function:

$$C(t) = K_P E(t) + K_I \int_0^t E(\tau)\, d\tau - K_D \frac{dE(t)}{dt}. \tag{5.6}$$

The error function E is the difference between the reading and the given setpoint, and C is the output signal to eliminate the error. The proportional response represents the restoring force. When the pressure is away from the setpoint, the error signal is nonzero. The controller adjusts the input flow to quickly reduce the error in the pressure to zero. However, when the pressure is rising quickly, the system is likely to overshoot the setpoint. The differential response monitors the rate of change of the error and reduces the flow if the rate is too high as the pressure approaches the setpoint. In this way, the overshoot can be minimized. The integral response includes the integral of the error over a given time period. This factor produces a resistance to change. Without the integral response, the system would not remain stable at the setpoint. When the pressure reaches the setpoint, the proportional response would be to shut off the input flow because there is no restoring force. However, this would cause the pressure to drop slowly. The integral response causes the system to flow enough gas to maintain the given pressure. The PID control unit is a microprocessor based system. The constants $K_{P,I,D}$ are tunable values which are used to optimize the control function for the characteristics of the particular system. For a system with a slower response, K_P and K_I would decrease while K_D rises.

After the system was filled with Xe/CH_4 and had run for several days to reach a steady state, the performance of the PID's was tested. Shortly before the tests were conducted, the compression pump for the detectors broke down. The time for repairs or replacement was several weeks. In order to continue operating the system, the gap pump was moved into the detector line, and the pump from the gas house was used in the gap line. Both of these pumps caused the system to operate at much lower flow rates, and therefore poorer response to pressure changes. However, the data in figs. 5.10 and 5.11 show that the system could still operate within the required parameters as is described below.

The main test of the PID response was simply to alter the setpoint and examine the behavior of the differential pressure as the system changed to the new value. The tests were conducted on the top 6 modules, and it was assumed that the behavior of the bottom modules would be much the same. Figure 5.10 shows the response to several changes in the setpoints of both detector and gap PID's. At point #1, the D/G setpoint was raised by 67 μbar (50 mtorr) which is a large perturbation. The differential pressure overshoots the setpoint, but stabilizes within approximately 10 - 15 minutes. The gaps were strongly driven by the large change in the detectors both at the change in setpoint, and when the system corrected the overshoot. This is because as the differential pressure between the detector and the gaps changes, there will be a corresponding change in the position of the foils. This causes a change in the volume and therefore pressure of the gaps. Given that the atmospheric pressure remains constant over this period, the net result is a shift in the differential pressure between gap and atmosphere as the pressure in the detectors is varied. The gaps recovered approximately 15 minutes after the detectors settled. At point #2, the G/A setpoint was raised by 67 μbar. Again, the gaps stabilized in 15 min, whereas the detectors remained steady during that time. Similar results were achieved when the D/G ΔP was lowered by 67 μbar at point #3, except that the recovery time was

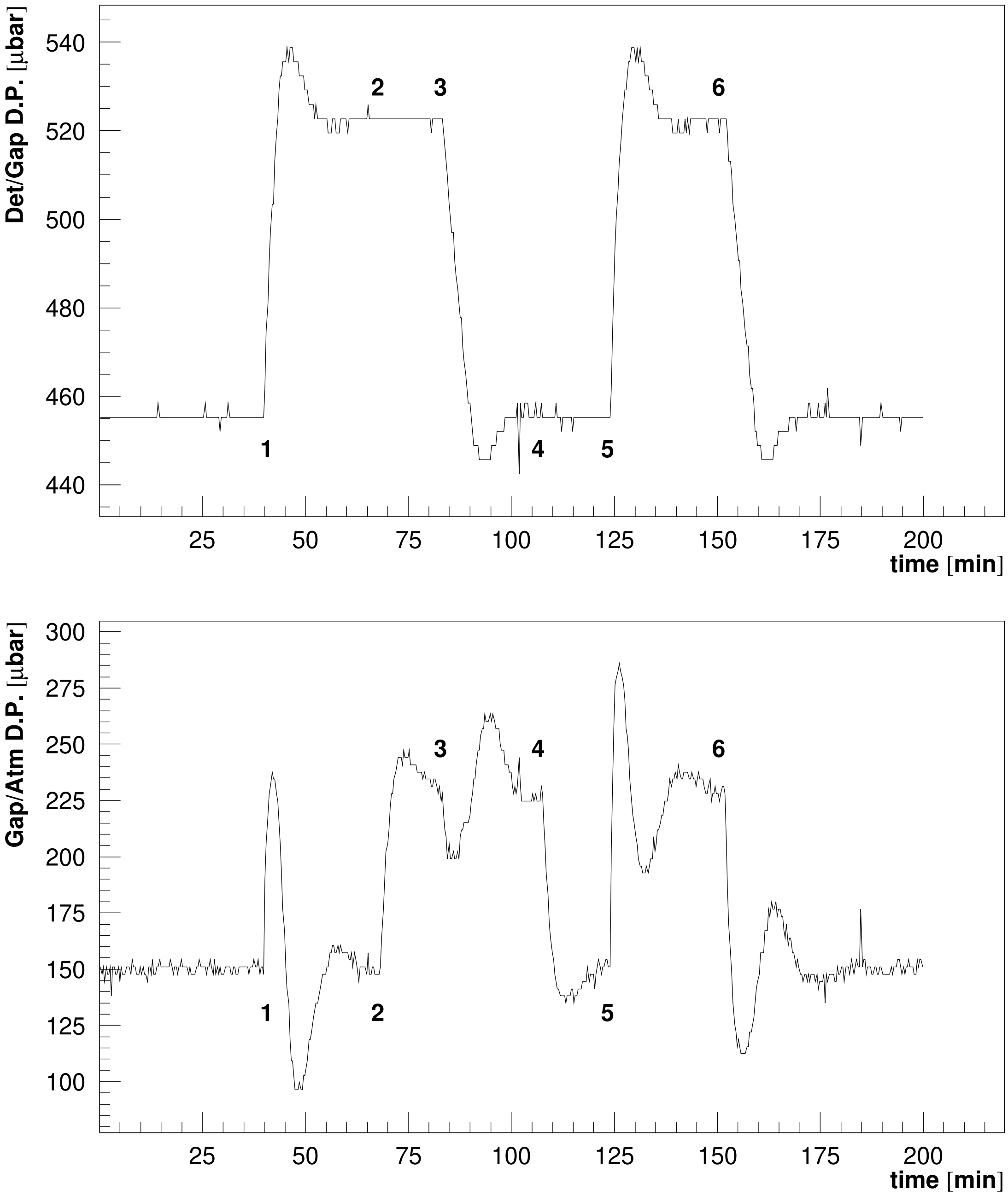

Figure 5.10: PID response to changes in the setpoint for both detector and gap. The numbered points on the graphs represent times at which PID setpoints were changed and are described in the text.

15-20 minutes. The G/A ΔP was lowered by the same amount at point #4. Again, the detectors showed virtually no reaction to the large change in the gaps. A more complex test was performed at point#5 where both the detector and gap setpoints were raised by 67 μbar. The detectors show virtually the same response as when they were raised alone. The gaps were driven by both the detector response and the G/A ΔP and stabilized only after the detectors had reached their setpoint. This was repeated at point #6 except that the setpoints were both lowered. The behavior in this case was much the same as in earlier trials. The time taken for both components to return to their setpoints was very similar to the sum of the time taken by the individual components. Once they had reached the setpoint after the last test, the gaps were left until the small fluctuations reached a similar level to that before the tests. This took another 15-20 minutes.

Given that the changes introduced were very large and sudden compared to the normal atmospheric fluctuations, the data look quite good. The overshoot seen in the detectors was not too large, and there were no further oscillations about the setpoint. Thus, while there is some overshoot when responding to a large error, virtually none occurred in correcting the overshoot. The response time, although long, was again not characteristic of the normal performance. Under normal conditions, the error function would be continuous instead of having the step introduced by changing the setpoint. This would allow the PID's to respond to the error as soon as it started to grow. The data do show that the system can correct large errors in both the detector and the gap without producing significant oscillation about the steady state. Also, they show that the detectors are not driven significantly by large changes in the gap pressure. The detector PID is able to maintain the constant differential pressure even though the total pressure in the gaps is varying significantly. The fact that the gaps followed changes in the detector is not a concern since the gain is not affected by the G/A differential pressure.

Another test was conducted to determine the ability of the system to equalize the pressures in six modules. Given that the six modules on top or bottom are controlled by the same PID, and the input gas is divided into each, they should all have the same

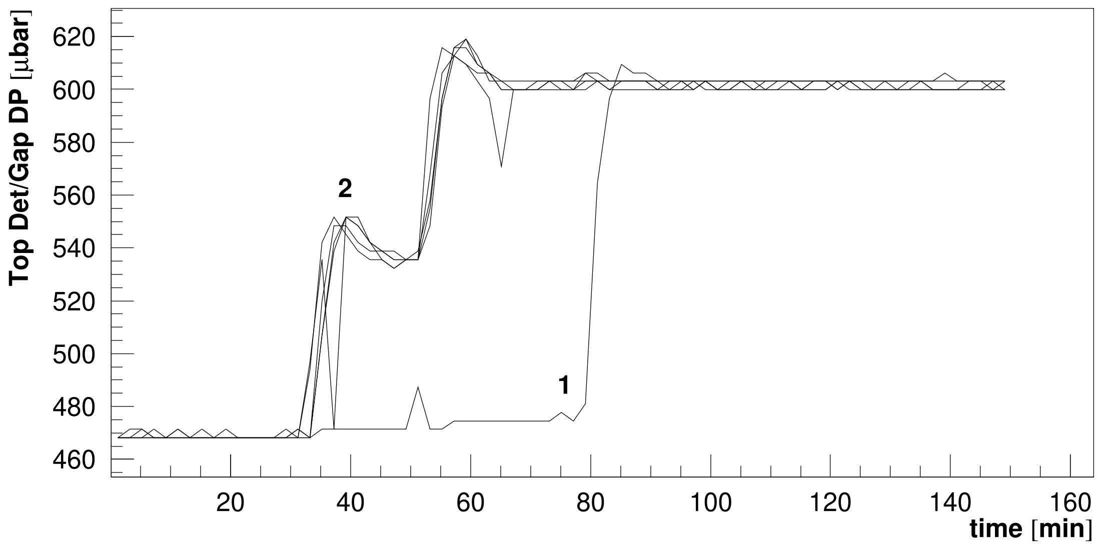

Figure 5.11: System response when one detector module out of six was set much lower than the rest.

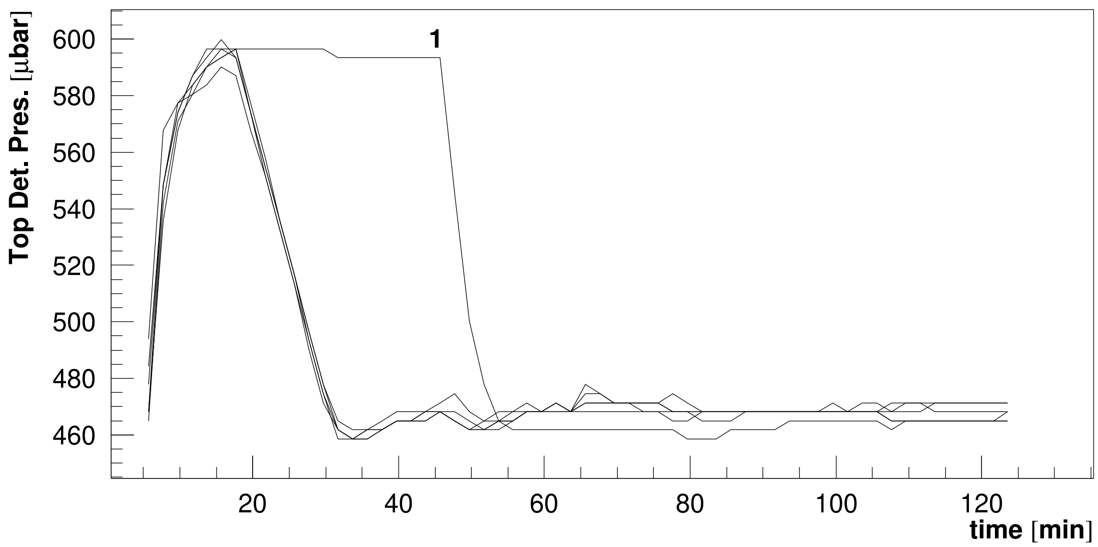

Figure 5.12: System response when one detector module out of six was set much higher than the rest.

differential pressures. In order to test this, one chamber was isolated while the others were raised by 133 μbar. After the other five chambers reached a steady pressure, the sixth was added back into the system. The results are shown in fig. 5.11. At point #1 on the graph, the valves to the one module were opened, adding it back into the control system. The pressure in that chamber quickly rose to the level of the others taking only 10-15 minutes to reach the proper pressure. The dip in the differential pressure at point #2 is due to a change in the setpoint as the five modules were changing pressure and is not relevant to this test. At first, the separation was only set to 67 μbar, but this was doubled as the system was approaching the new setpoint in order to test the response to a larger deviation. The test was repeated with one module much higher to begin with, and the results are shown in fig. 5.12. In this case, the pressure of all six modules were raised together. When they reached the higher pressure, one was isolated and the rest were dropped back down in pressure. The one module was added back into the system at point #1 on the graph. Again the one module returned to the approximate level of the others in about 10 minutes; however, it took a further hour for the differential pressure in that module to be indistinguishable from the rest. From these results, it can be seen that the system readily corrects significant pressure differences in a single module. Thus, the probability of one module deviating by a large degree is very slim, and all six modules can be assumed to have the same pressure.

As a true test of the pressure control system under normal conditions, one must observe the activity of the system during a storm when the atmospheric pressure changes dramatically. Fig. 5.13 shows that the differential pressures across the cathodes for both the top and bottom detectors remained extremely steady during the entire period.

A detailed look at the individual differential pressures in all six bottom detector modules is given in fig. 5.14. Apart from the first module, they behave essentially identically. The differential pressure for the first module appears to be about 3 μbar higher on average. However, this is the resolution of the ADC's and well within the tolerances of the system. The resolution is also the reason for the dual value of the pressure.

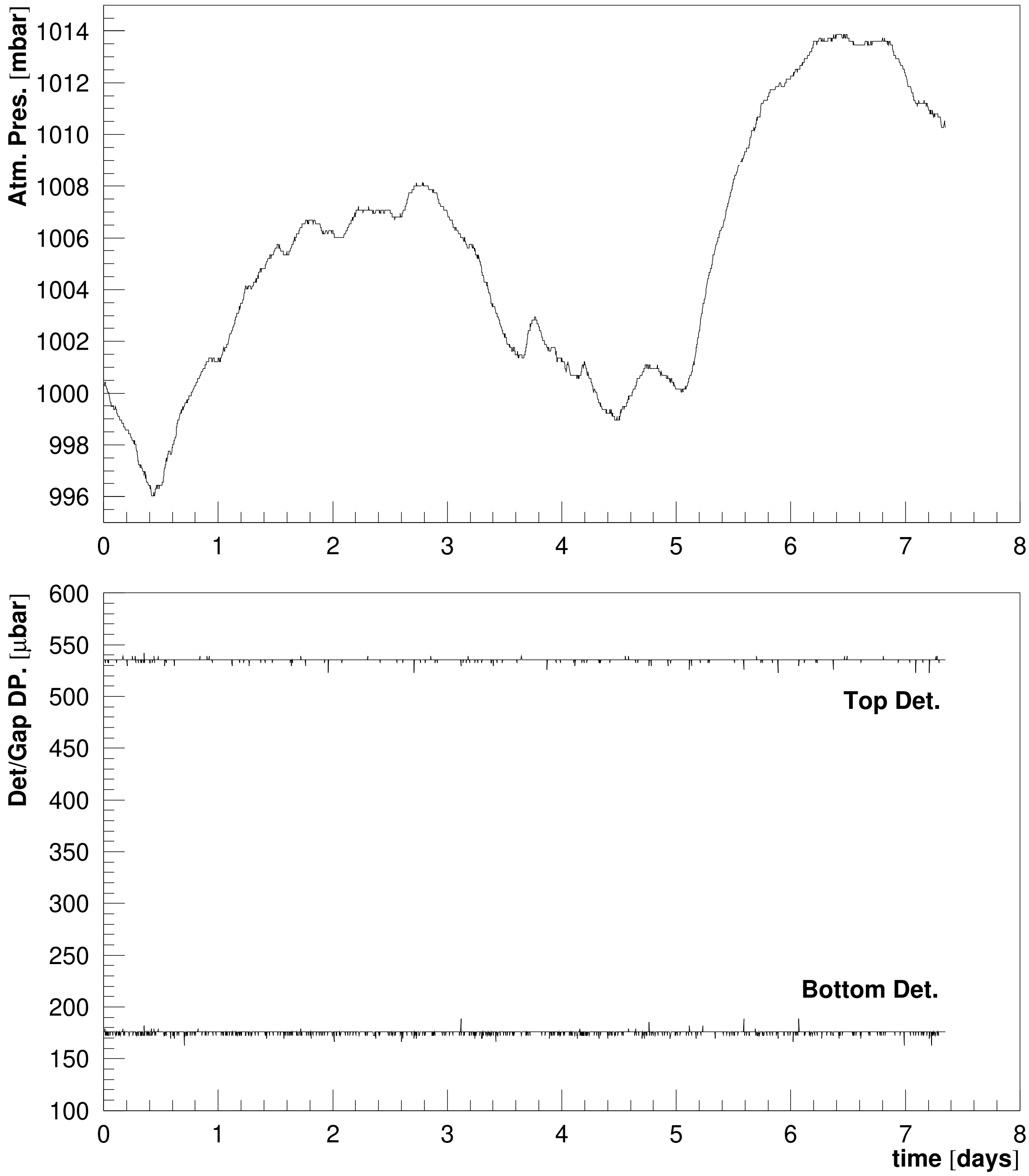

Figure 5.13: System pressure during a week of high atmospheric activity. The top graph shows the atmospheric pressure in the experimental hall. The bottom graph shows the average differential pressure across the top and bottom detector/gaps.

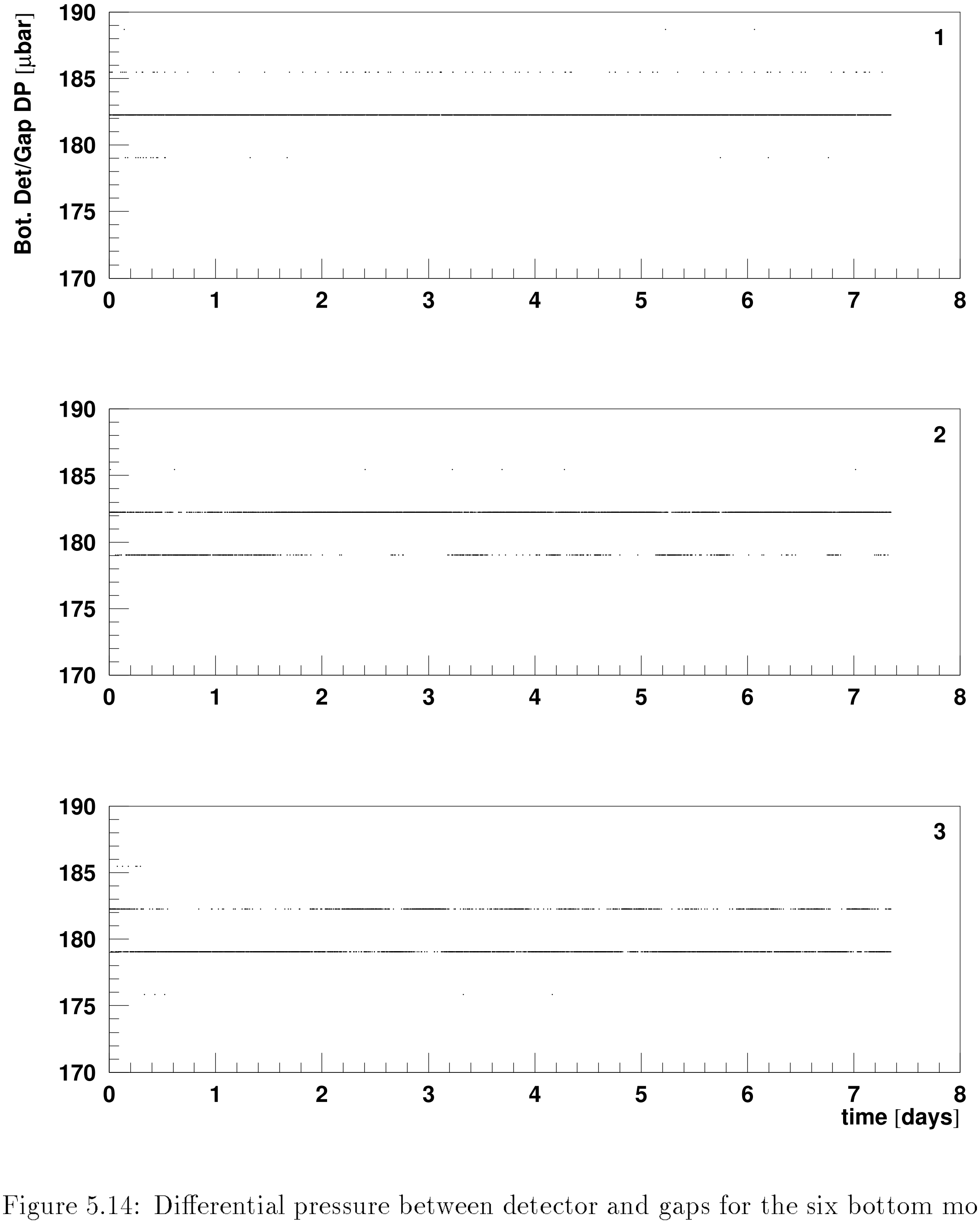

Figure 5.14: Differential pressure between detector and gaps for the six bottom modules. The dual value of the pressure is related to the resolution of the ADC's which is approximately 3 μbar.

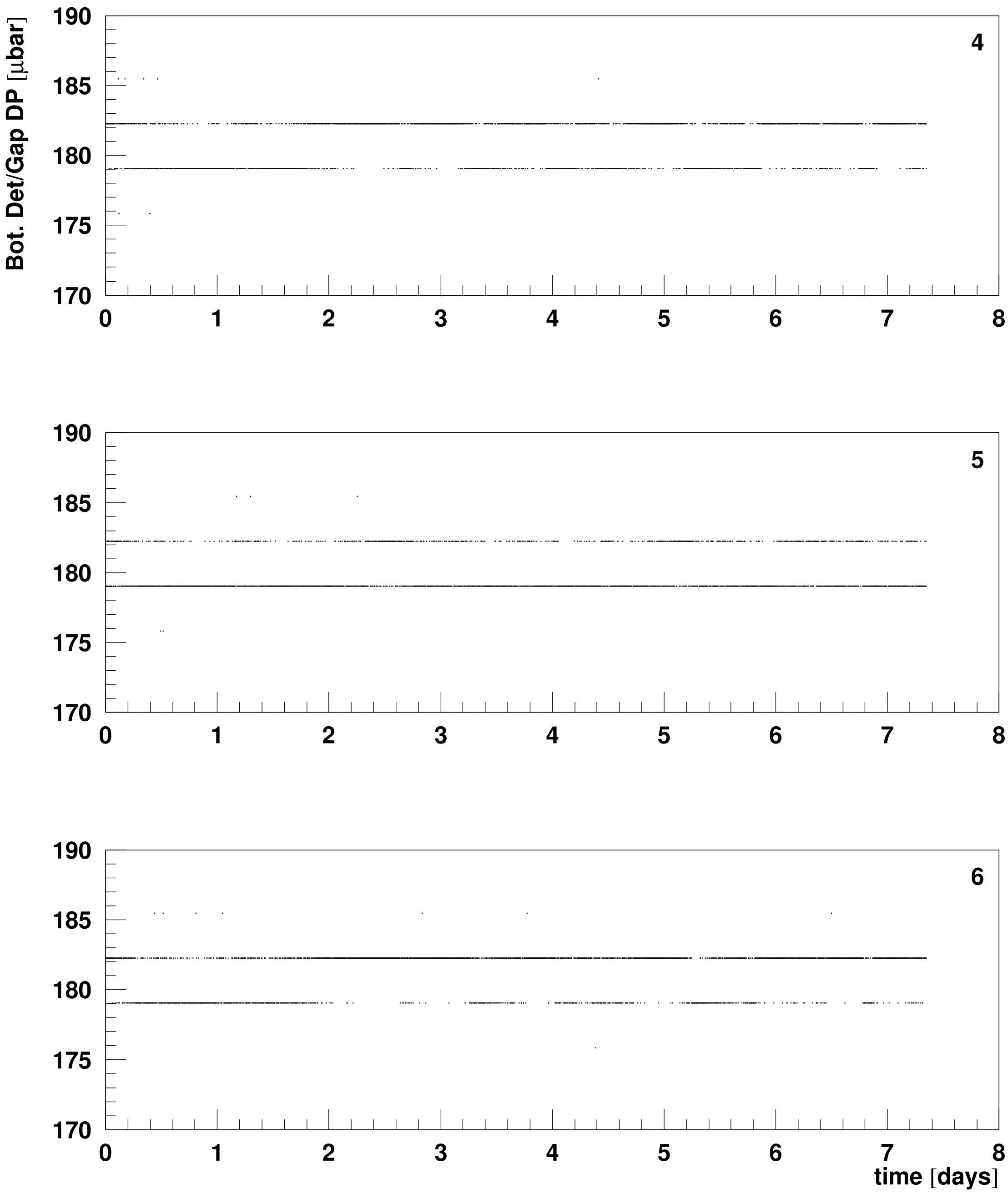

Figure 5.14: Differential pressure between detector and gaps for the six bottom modules.

The pressure control for the gas system performs to its specifications. It is able to maintain the differential pressure to better than 10 μbar. During the entire run period in 1995, the differential pressure remained as steady as shown in fig. 5.14.

5.5 Quadrupole Mass Spectrometer

The other main requirement of the gas system is a stable gas mixture. The gain is affected by small changes in the concentration of CH_4 or small amounts of impurities. Thus, it is critical to know the gas mixture accurately. This task is accomplished by the quadrupole mass spectrometer.

Gas is drawn through a turbo pump into the analyzing chamber where it is ionized by electron bombardment. The positive ions are accelerated and enter the quadrupole mass filter. The quadrupole consists of four cylindrical electrodes symmetric about the axis of the system. An alternating electric field causes the ions to oscillate, and they will strike the poles unless they have a specific mass/charge (M/e) ratio. Ions that pass through the quadrupole are collected by a Faraday cup where the signal is obtained by charge integration. By sweeping through a range of M/e, the QMS can show the relative concentration of various ions in the gas. A sample mass spectrum is shown in fig. 5.15. Identifying the signals with the atomic masses of the components yields the composition of the gas.

5.5.1 Ionization

The gas atoms or molecules lose electrons in the analyzing chamber through bombardment by energetic electrons and form positive ions. Depending on the energy of the incident electrons and the ionization potential of the atoms, multiply charged ions can form. Also, molecules can break down into ionized components. Because of this, there can be signals at several different values of M/e which all come from the same gas. Since the quadrupole filters particles by their M/e ratio, a doubly ionized

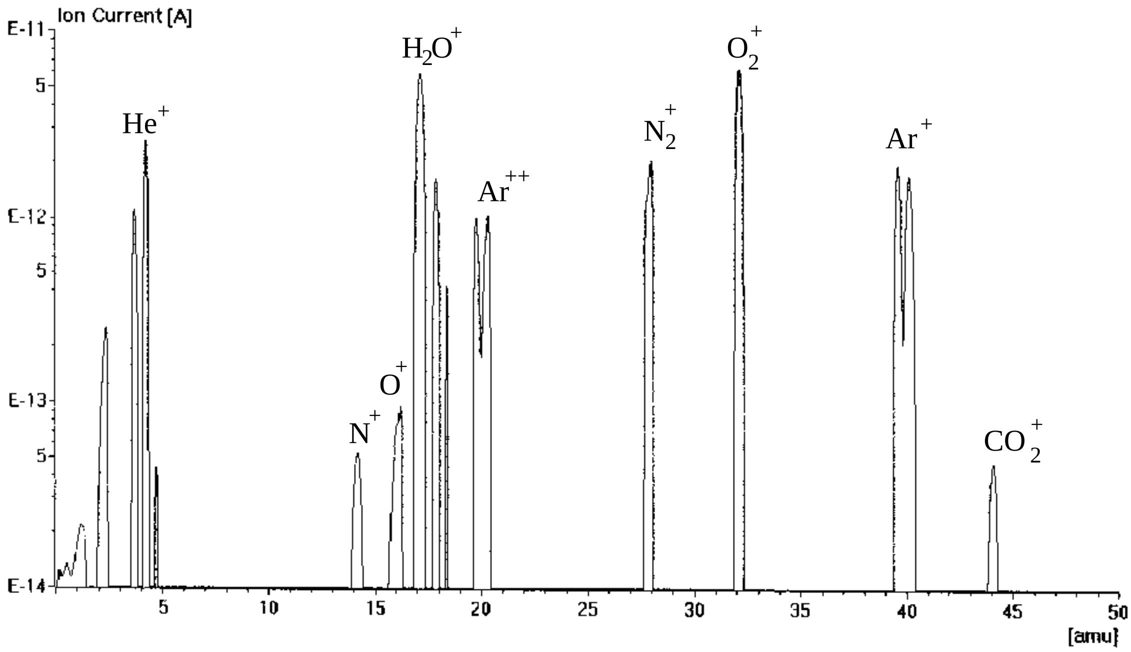

Figure 5.15: Mass spectrum for a gas mixture of He, Ar, N_2, and O_2.

particle will appear to have a mass of 1/2 its true value. Also, given that there can be several isotopes for one element, the mass spectrum can show several peaks even for the singly ionized, unbroken molecule. Fortunately, for a particular electron ionization energy, the mass spectrum for a species is well defined.[49] The probabilities for breakdown and ionization of a molecule are constant at a set electron energy. The natural abundances of isotopes are also constant. This results in a mass spectrum in which the ratio of the heights of the mass peaks will be the same for various measurements of the same gas. Sample spectra for pure gases are given numerically in table 5.1. Also, the height of the peaks scales linearly with the percentage of that gas in the mixture. Because of these properties of the mass spectrum, the concentrations of various gases within a mixture can be determined by analyzing the size of the ion currents at various mass settings. However, it can be seen in table 5.1 that different gases can have readings at the same mass value. In particular, this is the case with CO_2 where each of the main mass values overlaps with other gases.

Table 5.1: Relative peak heights for mass spectra of gases in HERMES. This does not provide sizes of all the possible peaks for a gas, just those with a size above 1% of the tallest peak. The heights are given relative to the largest peak for each gas.[49]

Gas	Ion	M/e (amu)	Relative height (%)	Gas	Ion	M/e (amu)	Relative height (%)
Xe	$^{136}Xe^+$	136	42.4	CH_4	CH_4^+	16	100
	$^{134}Xe^+$	134	50.0		CH_3^+	15	85.0
	$^{132}Xe^+$	132	97.8		CH_2^+	14	16.0
	$^{131}Xe^+$	131	88.0		CH^+	13	7.8
	$^{130}Xe^+$	130	22.8		C^+	12	3.0
	$^{129}Xe^+$	129	100	CO_2	CO_2^+	44	100
	$^{128}Xe^+$	128	13.0		CO^+	28	13.0
	$^{136}Xe^{++}$	68	26.1		CO_2^{++}	22	2.1
	$^{134}Xe^{++}$	67	31.5		O^+	16	16.0
	$^{132}Xe^{++}$	66	76.1		C^+	12	9.7
	$^{129}Xe^{++}$	64.5	77.2	N_2	N_2^+	28	100
	$^{136}Xe^{+++}$	45.3	7.6		N^+	14	14.0
	$^{134}Xe^{+++}$	44.7	9.0	O_2	O_2^+	32	100
	$^{132}Xe^{+++}$	44.0	32.6		O^+	16	18.0
	$^{129}Xe^{+++}$	43.0	25.0	H_2O	H_2O^+	18	100
Ar	$^{40}Ar^+$	40	100		HO^+	17	26.0
	$^{40}Ar^{++}$	20	22.6		O^+	16	1.8

A study was performed on the QMS using a lower electron ionization energy. The normal energy is 100 eV, but this can be changed to 70 or 40 eV. Since the ionization potentials for Xe^+, Xe^{2+} and Xe^{3+} are 12.1, 33, and 66 eV respectively,[50] reducing the electron energy to 70 eV should significantly reduce the amount of Xe^{3+} produced. A comparison of figs. 5.16 and 5.17 shows that this is indeed the case. By using the 70 eV ionization energy, virtually all of the 44 amu signal would come from CO_2. Given that the 70 eV ionization energy produced the desired reduction of the Xe^{3+} ions, the 40 eV ionization energy was not investigated since the mass resolution at that energy is poor.

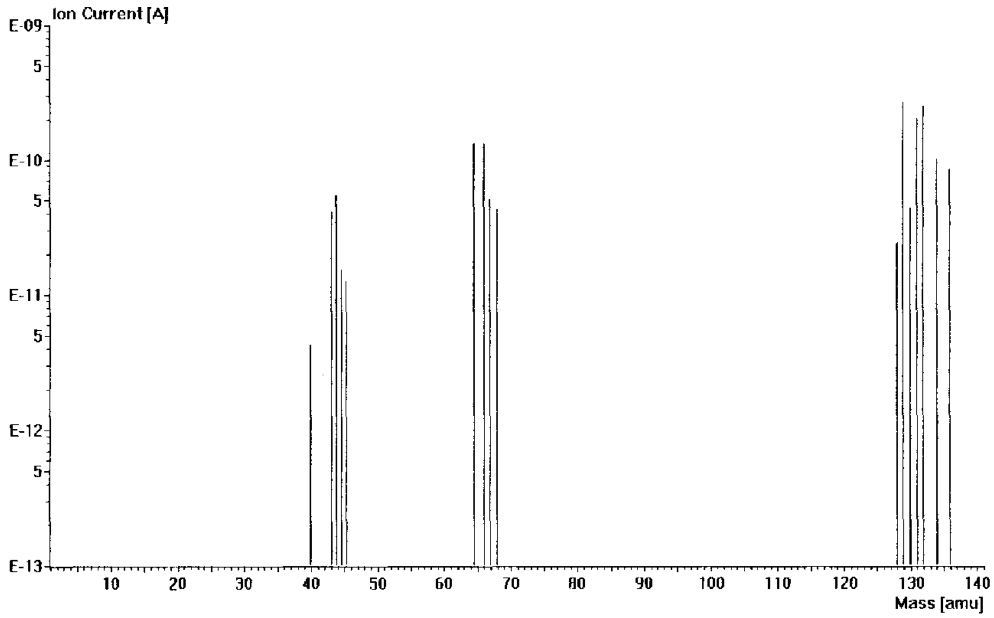

Figure 5.16: Xe mass spectrum at 100 eV electron energy. The reading at 40 amu is due to residual argon. The data was collected using a filter which finds the top of the peak.

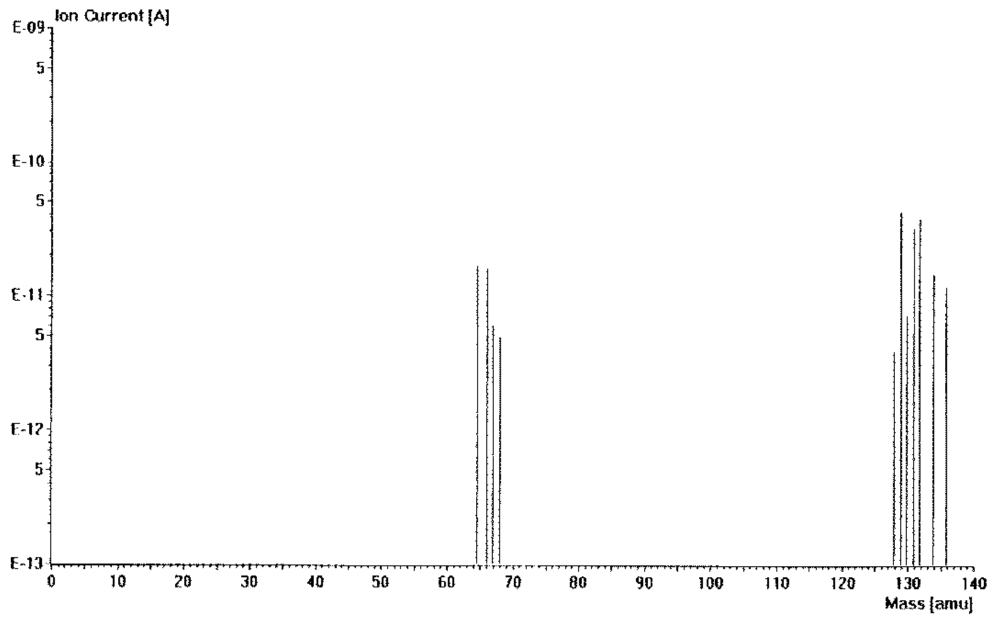

Figure 5.17: Xe mass spectrum at 70 eV electron energy.

It was quickly noticed that there was a significant pressure dependence in the concentration readings at 70 eV. The ion currents at 100 eV have also shown a dependence on pressure; however, it is uniform for all the peaks, and the concentration values are not affected. At 70 eV, the dependence is not uniform, and the concentrations changed with pressure. While not fully understood, this effect is likely due to space charge effects. Because of this pressure dependence, it was decided that the electron energy should be 100 eV.

5.5.2 Quadrupole Filter

The quadrupole filter consists of two pairs of cylindrical electrodes separated by a distance $2r_o$. A DC voltage $2U$ and alternating voltage $2V\cos\omega t$ are applied between adjacent pairs of rods. If the axis of the quadrupole is aligned along the z-axis, the

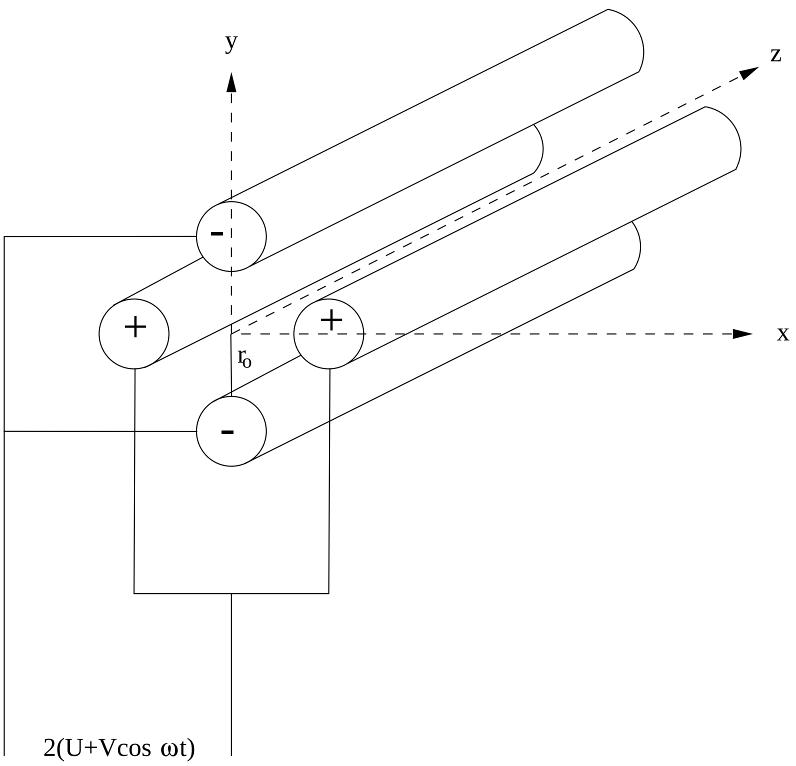

Figure 5.18: Schematic drawing of a quadrupole mass filter.

potential is

$$\Phi(x, y, t) = -(U + V \cos \omega t) \frac{x^2 - y^2}{r_o^2}. \tag{5.7}$$

This yields an electric field which depends linearly on the coordinates:

$$\overrightarrow{E}(t) = -(U + V \cos \omega t) \frac{2(\overrightarrow{x} - \overrightarrow{y})}{r_o^2}. \tag{5.8}$$

An ion of specific charge e/M traveling parallel to the z-axis would have the following equations of motion:

$$\begin{aligned} \ddot{x} + \frac{2e}{Mr_o^2}(U + V \cos \omega t)x &= 0, \\ \ddot{y} - \frac{2e}{Mr_o^2}(U + V \cos \omega t) &= 0, \\ \ddot{z} &= 0. \end{aligned} \tag{5.9}$$

It follows that:

$$\dot{z} = const. \tag{5.10}$$

Making the substitutions:

$$\begin{aligned} \omega t &= 2\zeta, \\ \frac{8eU}{Mr_o^2\omega^2} &= a, \\ \frac{4eV}{Mr_o^2\omega^2} &= q, \end{aligned}$$

yields Mathieu differential equations:

$$\frac{d^2x}{d\zeta^2} + (a + 2q \cos 2\zeta)x = 0, \tag{5.11}$$

$$\frac{d^2y}{d\zeta^2} - (a + 2q \cos 2\zeta)y = 0. \tag{5.12}$$

Mathieu functions have regions of instability where the solutions increase exponentially with ωt. The stability diagram in fig. 5.19 shows values of a and q for which the

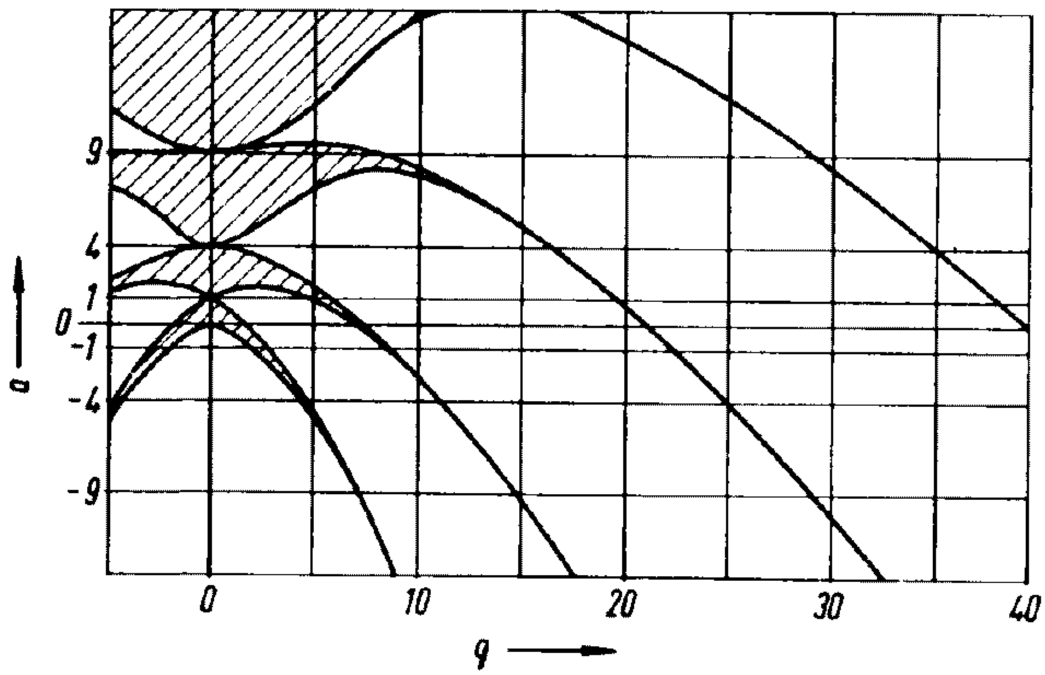

Figure 5.19: Stability diagram for the Mathieu functions. The shaded areas indicate regions of stability.

solutions are stable. For a given field, only the specific charge on the ion affects their values. Ions traveling along an unstable path will quickly collide with the electrodes. Only those ions traveling the stable path will traverse the quadrupoles. However, this path must be stable in both the x and y directions. The Mathieu equation of motion for x is simply that of y with a replaced by $-a$. Thus, to achieve stability in both axes, the points (q, a) and $(q, -a)$ must both lie in the stable region. The only region where this is possible is the lowest region in fig. 5.19 which is expanded in fig. 5.20.

For a given frequency ω and given voltages U and V, the value $a/q = 2U/V$ is independent of the mass M. Thus, all ions in the stability diagram regardless of mass lie on this line. For $U/V = 0.17$, it passes through the apex of the stable region and only one value of M is stable. This value then depends only on the geometry of the

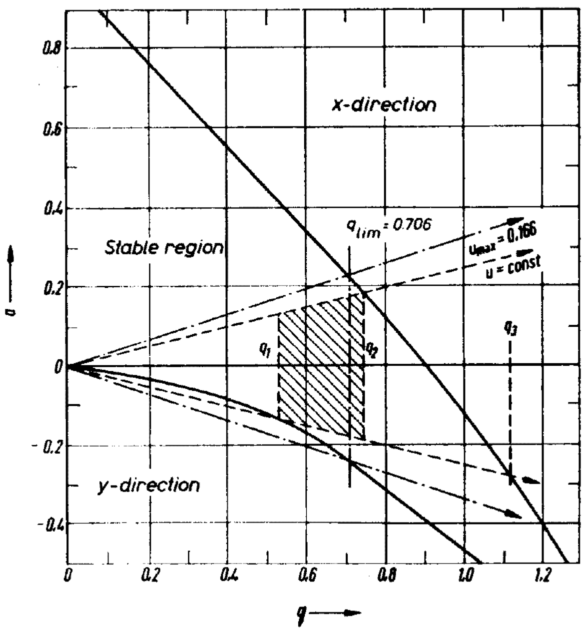

Figure 5.20: Lowest stability region for Mathieu functions. The shaded area indicates where a and $-a$ are both stable.

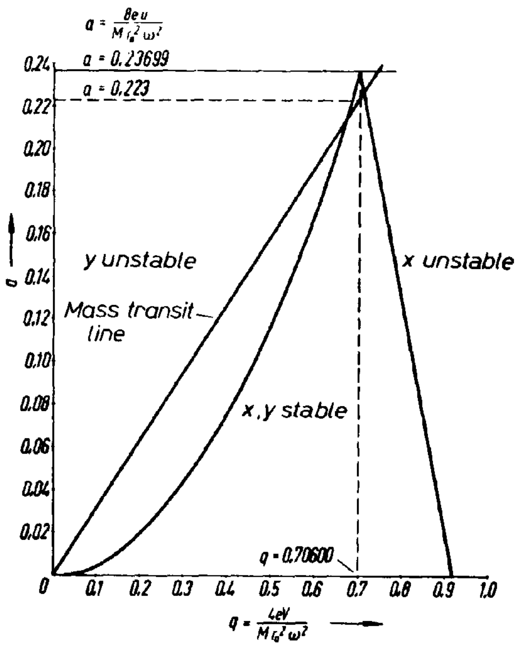

Figure 5.21: The lowest region of stability shown with the lower line reflected about the q-axis to show the region of xy stability.

field, the frequency ω and the amplitude of the alternating voltage V:

$$M = \frac{4eV}{q_o \omega^2 r_o^2} = \frac{5.7eV}{\omega^2 r_o^2} \tag{5.13}$$

where $q_o = 0.706$. By ramping through a range of voltages U and V, different masses can be measured.

5.5.3 Concentration

The QMS includes software which can analyze the ion currents, and using calibration values, calculate the concentrations of gases in the sample. The calibration of the system involves establishing a matrix which contains the mass peaks to be measured and the gas to which each peak corresponds. At each mass for a particular gas, the matrix contains a value which corresponds to the relative height of that peak with respect to the others. The matrix only contains relative values, and therefore, the user fixes the value of one point – usually at 1.0 – and all other values in the matrix are determined relative to it. The analysis module uses a least squares fit to determine the concentrations of gases. The matrix is calibrated using a gas mixture in which the concentrations are precisely known. These are input to the system, and the mass spectrum is measured. An automatic routine generates the matrix values. When properly calibrated, the QMS can measure concentrations down to less than 1 part per million.

The calibration of the matrix becomes complicated by the fact that several different gases can produce a signal at the same mass. This can lead to a false interpretation of the gases present in the sample. For example, table 5.1 shows that CO_2 is a particular problem. The main mass values for CO_2 are at 44, 28, and 16, and each of these overlaps with other gases. The spectrometer can correctly interpret the gases present even with a mass overlap, provided that the matrix has been properly calibrated for each gas with that mass value. In order to do this, the calibration gas must be selected such that the signal at each mass can be attributed to only one gas in the mixture. Because of this, HERMES had to carefully select a set of several premeasured mixtures

Table 5.2: Gas mixtures used for calibrating the HERMES mass spectrometer.

Gas 1	Gas 2	Gas 3
Ar 5%	Ar 5%	Ar 5%
Xe 90%	He 88%	He 94%
CH_4 5%	CF_4 5%	CO_2 1%
	N_2 1%	
	O_2 1%	

Table 5.3: Calibration matrix for QMS.

	Xe	CH_4	CF_4	O_2	CO_2	N_2	Ar	He
4								0.6341
15		0.5862						
16		0.6664			0.1376			
22					0.004227			
28					0.09348	1.144		
32				0.7898				
40							1	
44	0.078				0.623			
50			0.03701					
69			0.3131					
129	0.2891							
131	0.2043							
132	0.2487							

in order to fully calibrate the matrix for the various gases encountered in the system, and they are listed in table 5.2. These gases were specifically mixed for this purpose, and their concentrations have been determined to 3 significant digits. Because the matrix contains relative values, there must be a gas common to all calibration mixtures to be used as the reference. In the case of HERMES, argon is selected as the common gas. This is because none of the peaks in the Ar spectrum are the same as those of the other gases. Three different mixtures are necessary because CO_2, CH_4, and O_2 each have contributions at 16 amu. The concentration of water in the system is not measured because of the difficulty in producing a calibration gas with an accurately known concentration of H_2O.

The QMS is equipped with analog and digital outputs. The analog outputs are used to send the concentration data to the slow control system. This way, the QMS data can be saved along with the other gas system parameters and sent to the main HERMES slow control system. Also, this enables the system to activate an alarm when the impurity level passes a certain threshold. The digital outputs allow the QMS to directly operate a set of solenoid valves which change the gas that reaches the spectrometer. The calibration gases are permanently connected to the system so that the QMS can be quickly calibrated. Also, the system allows other gases to be analyzed by the spectrometer such as the gas from the drift chambers in the HERMES tracking system.

Figure 5.22 shows typical data on the composition of the gas mixture over several days. The CH_4 level appears to fluctuate by $\pm 1\%$ which leads to gain fluctuations

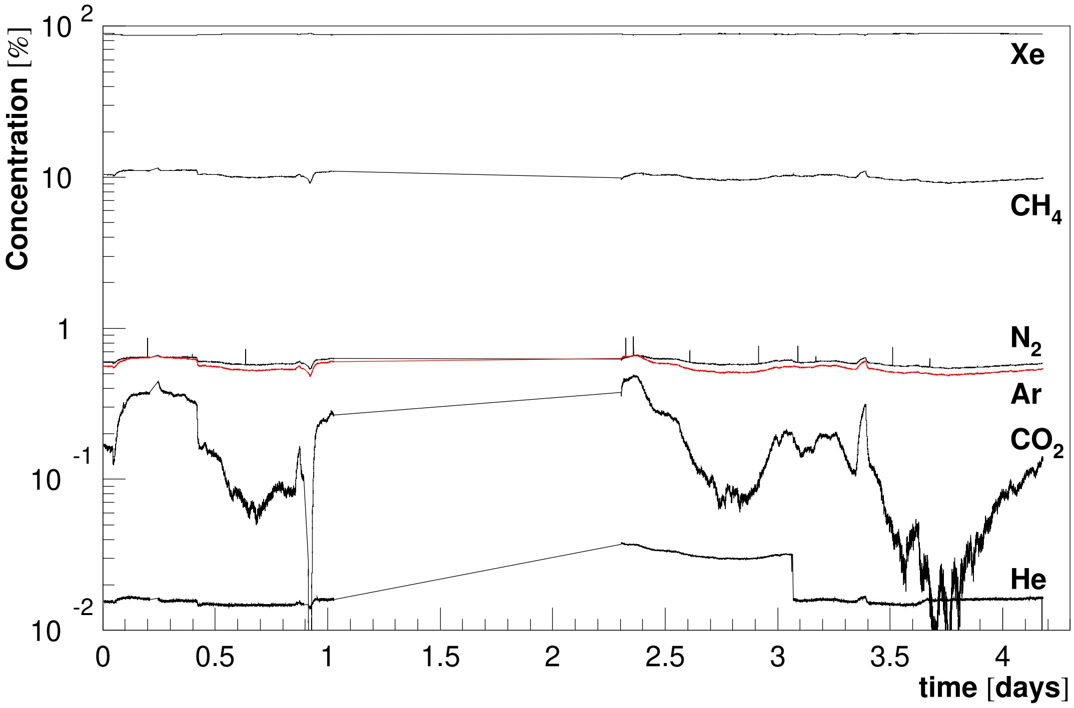

Figure 5.22: Gas concentrations over several days during the run period. The straight lines during the second day indicate that the QMS was not recording.

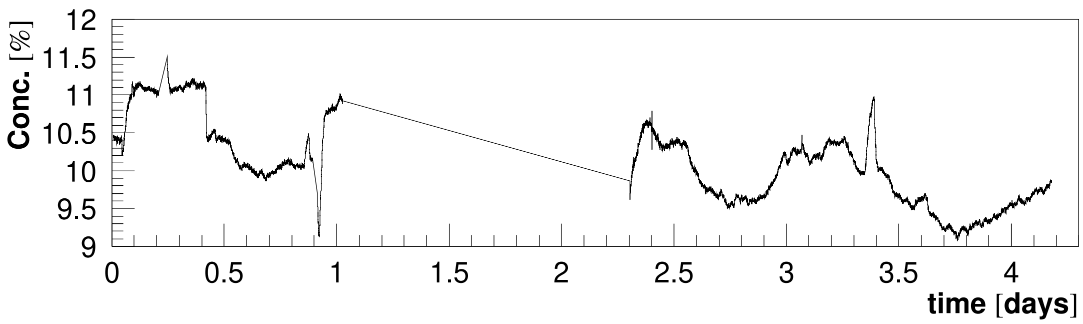

Figure 5.23: Expansion of fig. 5.22 to show the CH_4 concentration.

of up to 10%. Unfortunately, the data are not entirely accurate. A temperature dependence was discovered in the QMS. As the ambient temperature increased, the readings decreased. In fig. 5.23, this effect can be seen as the concentration reaches a local minimum each evening. However, this does not account for the overall decrease in the CH_4 concentration. These data indicate that the goal of CH_4 stability to $\pm 0.1\%$ was likely not achieved. However, the stability of the CH_4 concentration proved good enough for the operation of the TRD.

5.6 Purification

Because of the need for Xe recirculation, the gas needs to be purified in order that the contaminants are held to a minimal level. There are two types of purification units in the gas system: the membrane gas separator (MGS) and molecular sieves.

5.6.1 Membrane Gas Separator

The MGS consists of a series of thin walled capillaries running through the center of a larger pipe. The gas flows through the capillaries and can diffuse through the membrane walls. The capillaries are used to maximize the surface area of the walls.

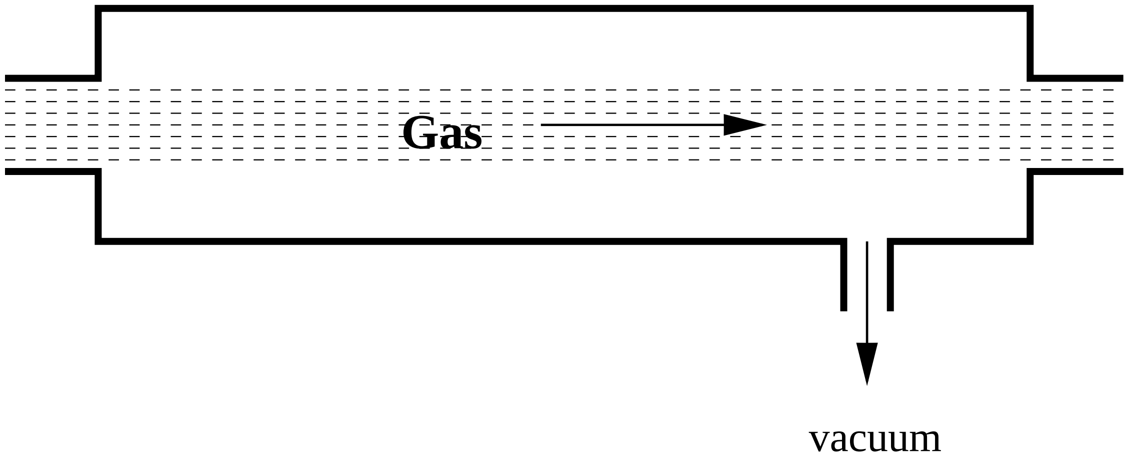

Figure 5.24: Schematic drawing of the membrane gas separator.

When a vacuum is created in the outer pipe, the large differential pressure causes the gas to diffuse much more rapidly. Gases with higher permeabilities pass through the walls more easily and are removed. When the contaminants have a higher permeability than the main gases, this system is an effective tool for purification.

The main use of the MGS is during the initial change of gas from CO_2 to Xe/CH_4 in the system. This change must be done in closed loop operation in order to prevent Xe losses. The amount of a gas removed by the MGS is proportional to its concentration. Thus, when the system is filled with CO_2, it is removed readily. When the concentration of CO_2 reaches a few percent, the MGS is no longer effective because not only is the MGS drawing only a small amount of CO_2, it is also drawing in an appreciable amount of Xe and CH_4. Thus, the relative concentration of Xe to CO_2 reaches an equilibrium level.

Figure 5.25 shows the data taken during the gas change for the TRD. The information on the graph is rather complicated because several activities are occuring which affect the readings. First, as the CO_2 is drawn out of the system, the pressure is restored with Xe/CH_4. Fresh gas is added to the system when the pressure drops below a certain threshold until the pressure rises to an upper setpoint. The input lines to the QMS are located fairly close to the gas supply lines, and when fresh gas is being

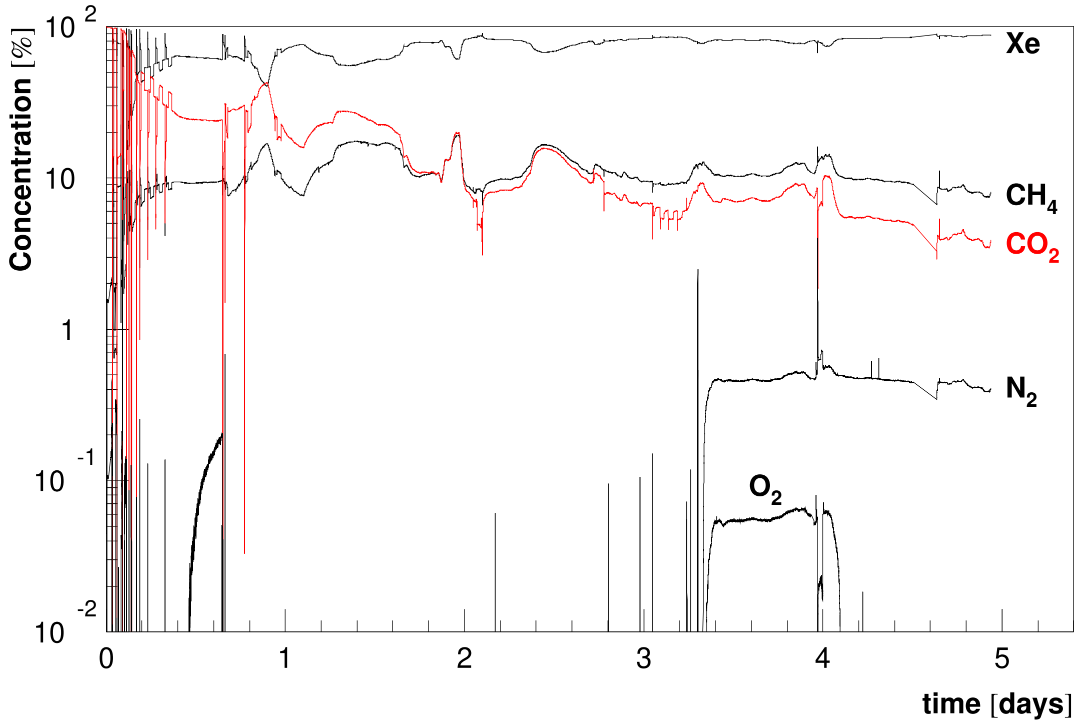

Figure 5.25: Gas concentrations during the change from CO_2 to Xe/CH_4. A complete description of this plot is provided in the text.

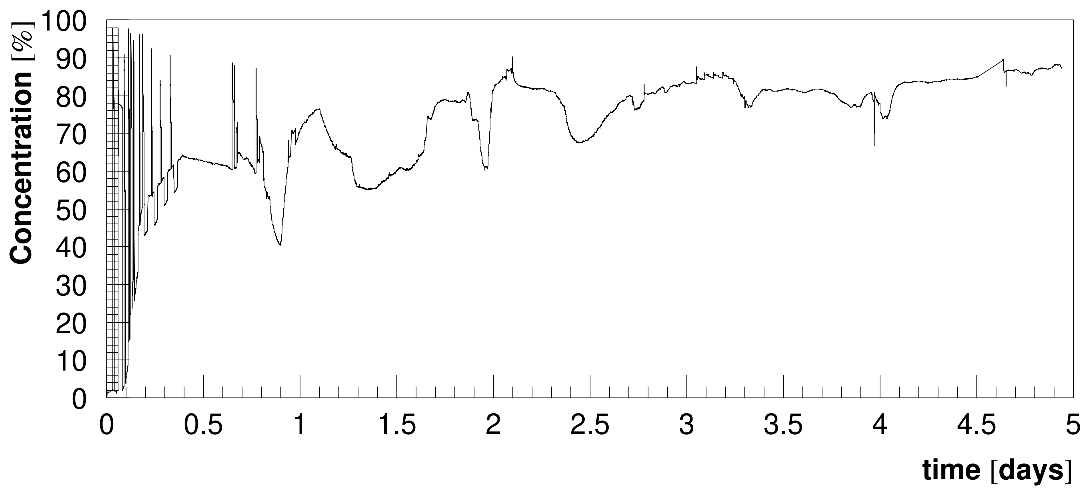

Figure 5.26: Xe trace isolated from fig. 5.25.

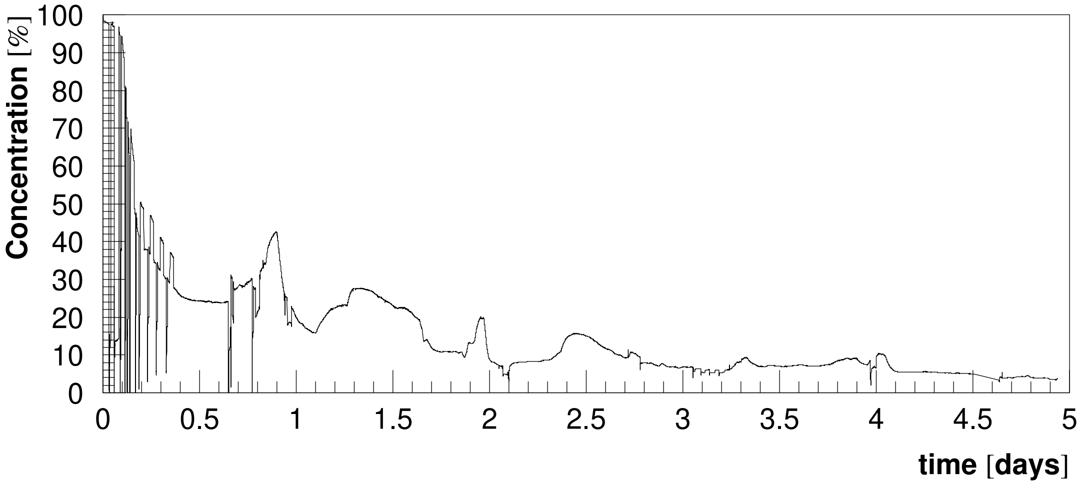

Figure 5.27: CO_2 trace isolated from fig. 5.25.

added to the system, it flows into the QMS input lines. The spikes in the first day on the graph are a result of the concentration readings switching between the actual gas in the system and the pure gas being added periodically. Second, the pump on the MGS was found to overheat when used to pull large amounts of gas for extended periods. Thus, the MGS could only be operated periodically until the CO_2 level had dropped to the point that the pump was only drawing a small amount. The small periodic fluctuations seen in the first 12 hours come from the periodic operation of the MGS. After about 5 days, the CO_2 concentration remained level at approximately 5%. At this point the MGS was shut off and the sieves were added to remove the remaining CO_2.

5.6.2 Sieves

The sieves are materials which selectively remove certain gases. They consist of porous pellets of absorbent or reactive material several mm in diameter. As the gas mixture passes through the material, certain gases bond to the surface and are removed from the gas system. The sieves are very effective at removing various gases until they

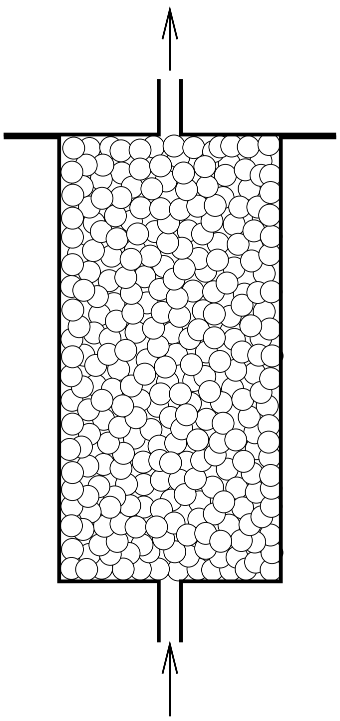

Figure 5.28: Cross section of a container containing sieve material.

become saturated. After this point, that gas will pass through while others continue to be absorbed. Due to the fact that the sieves can hold a large amount of O_2, H_2, and CO_2, these gases are purified from the system. There are several types of sieves used in or tested for the system referred to by their commercial names: R-311, 3 Å, 4 Å, and 13x.

The R-311 sieve is an activated copper material made by BASF Inc. It is mostly copper with catalysts added to improve its reactivity. It is very efficient in removing oxygen from the system through the oxidation reaction:

$$Cu \; + \; \frac{1}{2}O_2 \; \longrightarrow \; CuO \tag{5.14}$$

The 3 Å, 4 Å, and 13x sieves are made by Union Carbide Corporation. They are crystalline alumino-silicates known as "Zeolites." The chemical structure of each is similar, and they are shown in table 5.4 They are activated for absorption by

Table 5.4: Chemical formula and pore diameter of molecular sieves.

Sieve	Formula	Pore
3 Å	$K_{12}[(AlO_2)_{23}(SiO_2)_{12}]\cdot 27H_2O$	3 Å
4 Å	$Na_{12}[(AlO_2)_{23}(SiO_2)_{12}]\cdot 27H_2O$	4 Å
13x	$Na_{35}[(AlO_2)_{86}(SiO_2)_{106}]\cdot 276H_2O$	10 Å

removing their water of hydration, which is the large number of H_2O molecules bound to the main crystal. Small cavities are formed in the crystal structure which are interconnected by pours of a fixed diameter. The sieves absorb molecules selectively depending on their molecular size since the molecules must be able to pass through the pores in order to be absorbed. Furthermore, the sieves are particularly absorbent to water and to polar or polarisable molecules.[51]

The R-311 and the 3 and 4 Å sieves were studied to find out their capacity to trap the various gases in the system. The sieves were first purged by flowing N_2. Unless a molecule is strongly bound to the surface, a flow of gas can knock it loose. The output flow was measured and the gas was analyzed with the QMS. Once the output flow from the sieves showed pure N_2, the gas being tested was flowed into them at a constant rate. The output flows of both gases were determined from the flow and QMS data. Once the input and output essentially agreed, the sieves were considered saturated, and the output flows were integrated to determine the total amount of gas absorbed. Sample results are shown in figs. 5.29 and 5.30. Notice that although the R-311 is designed to remove oxygen, the other gases can also be absorbed. When the sieves were purged with N_2 for the next test, the results were also recorded to determine the amount of gas exiting the sieves. Fig. 5.31 shows that the flowing nitrogen through the system can remove the absorbed gas. This shows that the molecules can be knocked off the surface and are not bonded chemically to the sieves. The exception to this is O_2 which must be removed through a reduction reaction. The data are summarized in table 5.5. Data of this sort were not collected for the 13x sieve because its use was not anticipated at the time of these tests. Because of the data on the amount of CO_2 absorbed by the 4 Å sieve, a mixture of 4 Å and R-311 was chosen for the purifiers.

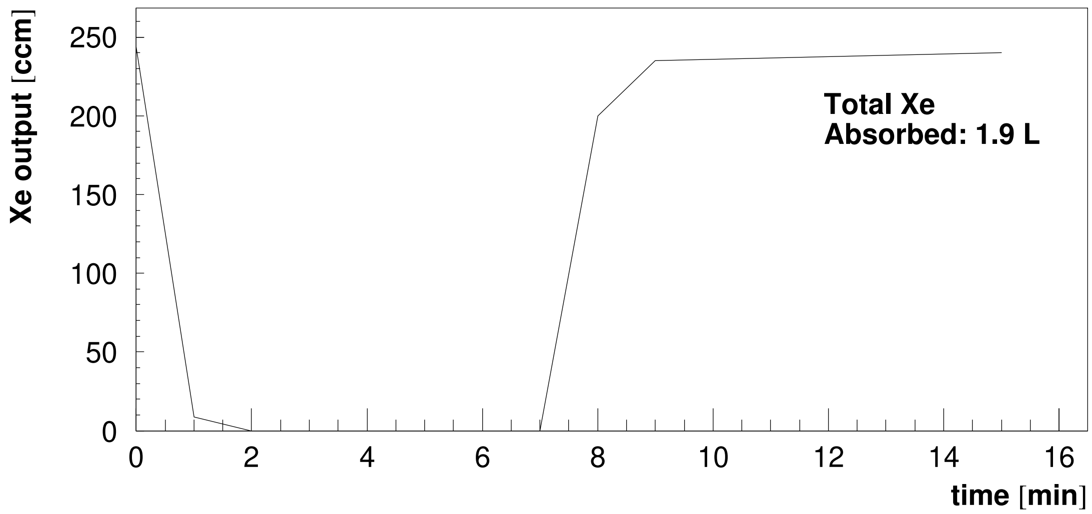

Figure 5.29: Output flow of Xe from a clean R-311 sieve.

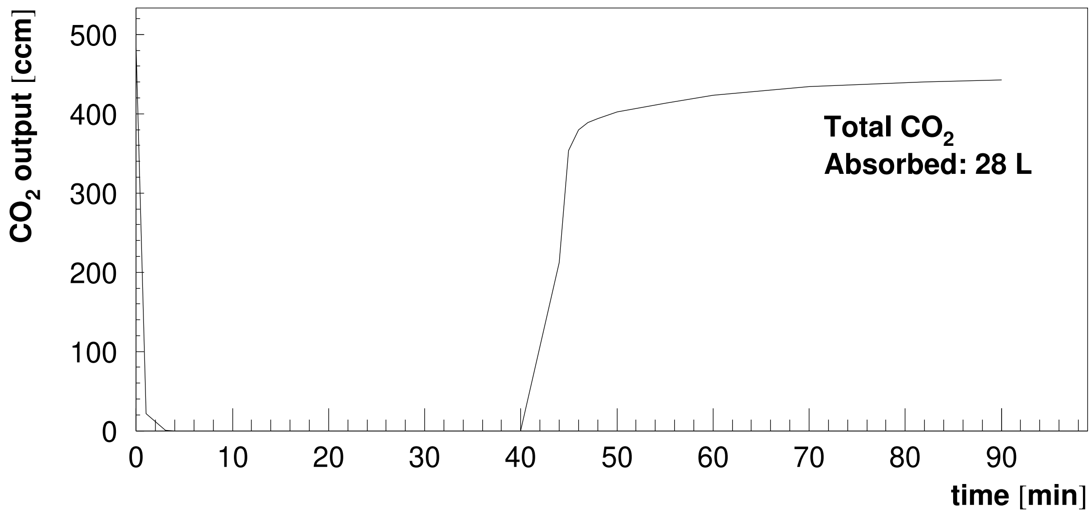

Figure 5.30: Output flow rate of CO_2 from a clean R-311 sieve.

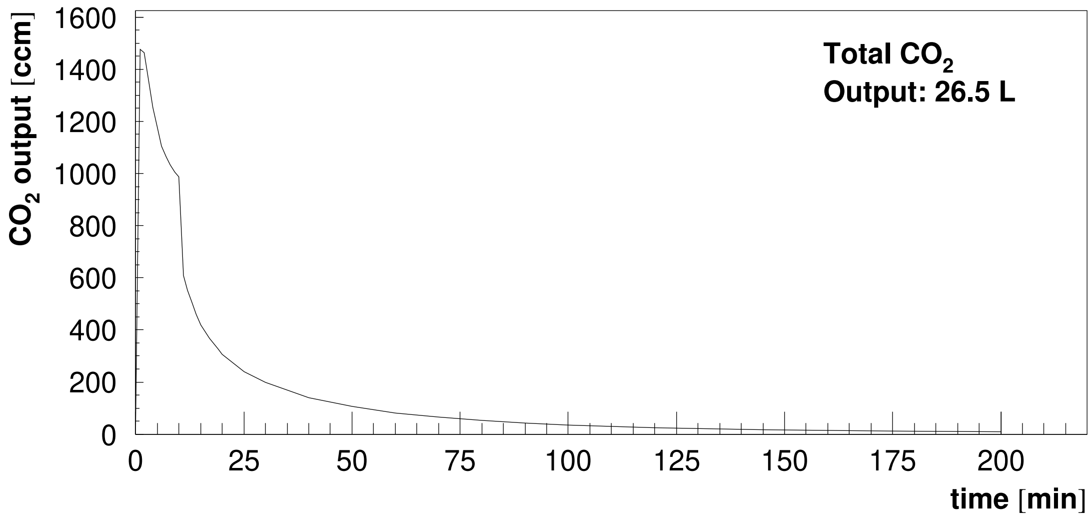

Figure 5.31: Output flow of CO_2 as N_2 is flowed into R-311 sieve saturated with CO_2.

Table 5.5: Litres of gas absorbed per litre of sieve.

Gas	R-311	4 Å	3 Å
Ar		0.8	1.4
CF_4	3	0.8	2
CH_4	2	10	1.4
CO_2	14	53	1.4
H_2O		150	
N_2	1.4	1	1
O_2	5		
Xe	3.8	1.4	1.2

During the main gas fill, a problem was encountered. When the sieves were added to the system, the CO_2 level was less than 5%, and instead of dropping sharply as expected, the concentration showed only a small decrease. However, a test was conducted at TRIUMF which showed that that CO_2 could be removed from a gas mixture when the initial concentration was 1%. An explanation for this discrepancy is that the CO_2 molecules are bound weakly to the 4 Å sieve and can be knocked out

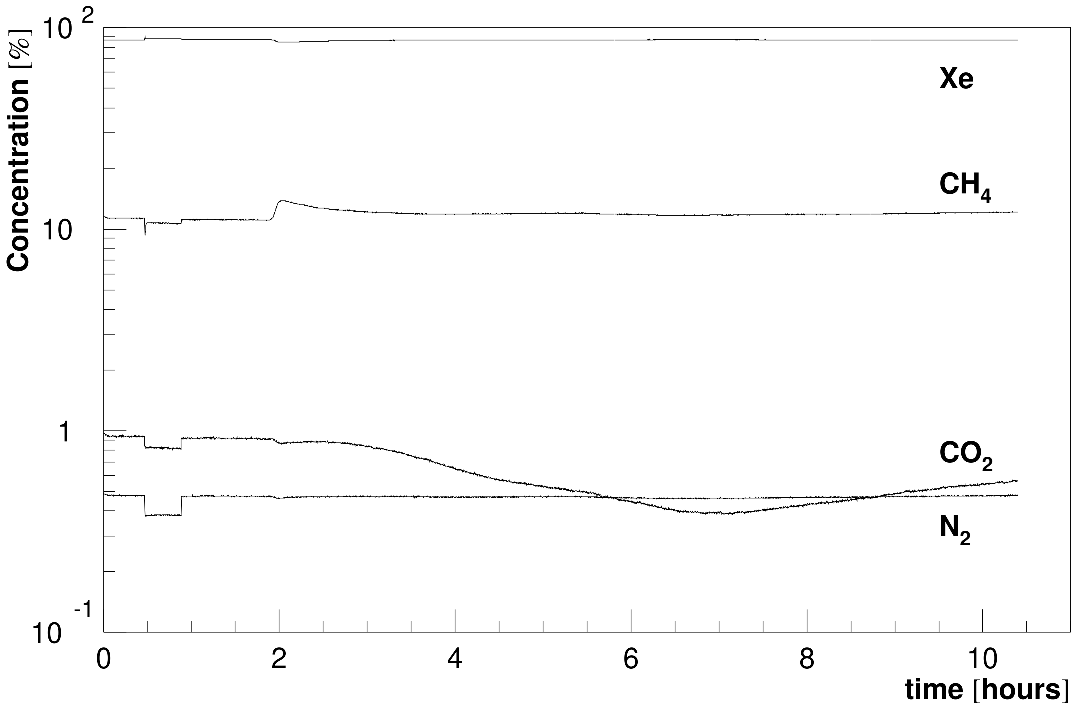

Figure 5.32: Gas concentrations during the latter stages of Xe/CH_4 fill. The sieves containing R-311 and 13x were added into the system at approximately the third hour, and they became saturated after 3-4 hours.

by a high gas flow. The flow for the test was less than 1 L/min, whereas the flow through the sieves in the gas system is approximately 10 L/min. Thus, the steady state CO_2 concentration is much higher in the gas system. Because of this problem, the 13x sieve was chosen as an alternative since it absorbs CO_2 more strongly and it had been used successfully in the Zeus experiment.[52,53] A new sieve mixture was chosen consisting of 1 L each of R-311 and 13x. Once it was added into the system, the CO_2 concentration dropped significantly as can be seen in fig. 5.32.

The process of regenerating the sieves is reasonably simple. Once saturated, they are removed from the gas system and placed in a regenerating unit located in the gas house. The container is heated to 150°C and N_2 gas is flowed through the system to remove the trapped gases. The heating allows the trapped molecules to be knocked

Table 5.6: Diffusion rates of impurities and saturation times for R-311 sieve.

Gas	Rate (mL/day)	Time (days)
CO_2	1440	14
H_2O	10	10^4
O_2	12	625

from the surface more easily. A condenser at the output on the bottom of the container allows the amount of water released to be measured. When the water has been removed from the system, 5% of H_2 is added to the gas in order to reduce the R-311 according to the reaction:

$$CuO + H_2 \longrightarrow Cu + H_2O \tag{5.15}$$

This reaction is strongly exothermic, and therefore the hydrogen is heavily diluted in order that the reaction does not cause the sieves to overheat. The water released is collected at the condenser and also serves to show when the reaction is complete. Once the sieves have been fully regenerated, the N_2 gas is pumped out while it is still hot. After this, the system is cooled and filled with the Xe/CH_4 90/10 mixture in order to saturate these gases before it is returned to the gas system. This way, once it is added back into the gas lines, it can continue to absorb the impurities without affecting the Xe/CH_4 concentrations.

The frequency of regeneration depends on the rates of diffusion into the detector and the capacity of the sieves. The limiting rate is clearly the CO_2 since this can diffuse directly from the gaps into the detector. The original plan was to use the membrane separator to maintain the CO_2 at a low level while the sieve would be used only for water and oxygen. However, the loss of a a few mL/min Xe through the MGS adds up to approximately 10 L per day. Compared to the amount of Xe lost through absorption in the sieves and through their regeneration, the economical solution is clear. The MGS is left out of the gas lines during normal operation and the entire purification is done by the sieves. It is during the gas change that the roles are reversed because of the MGS can readily remove CO_2 when it is in high concentration, and the sieves would become saturated too quickly to be practical.

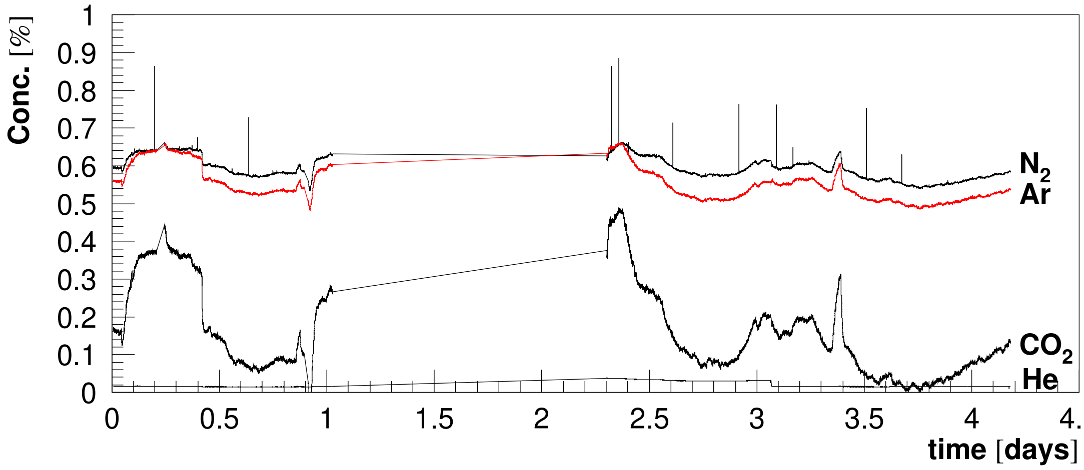

Figure 5.33: Expanded view of fig. 5.22 showing impurity levels.

Figure 5.33 shows the impurity levels over several days. The range of CO_2 concentration is approximately $0.2 \pm 0.2\%$. This just satisfies the 1% gain stability requirement. The CO_2 fluctuations are significantly larger than that of the other impurities because it diffuses into the detectors at a much higher rate due to the CO_2 in the gaps. Also, given that the QMS is located in the return line of the system, the gas is analyzed before it enters the sieves. Thus, the actual CO_2 contamination in the gas entering the detectors could be much smaller than the QMS measurement. The oxygen level does not show up on the graph because its signal is below the range of the QMS. Thus, it is removed very efficiently by the sieves.

5.6.3 Nitrogen and Argon Removal

Nitrogen and argon are difficult gases to remove from the system. They are not removed by the membrane separator, and are absorbed very poorly in the sieves. Thus, they are not removed from the system by the current purification units, and a third type of purifier was proposed in order to remove them. This purifier utilizes the differences in the boiling points between Xe and N_2/Ar. The gas mixture flows

Table 5.7: Melting and boiling points of system gases.[54]

gas	m.p. (K)	b.p. (K)
Xe	161.4	165.15
CH_4	90.69	111.67
N_2	63.15	77.35
Ar	83.85	87.25

through a pipe which is cooled to approximately 163 K. At this temperature, the Xe condenses and flows down into a separate section where it is heated and returned to the gas system. The N_2 and Ar remain in the gaseous state and continue to flow through the pipe where they are exhausted. The problem with this system is that Xe will be lost due to its vapour pressure. Also, if the temperature is too close to the freezing point, Xe snow will form on the walls and could clog the system.

Fortunately, the flush gaps remove most of the N_2 before it diffuses into the chambers. N_2 was calculated to be entering the chambers at a rate of 2.4 mL/day which is sufficiently low that the level won't exceed 0.2% after a year. The rate at which Ar enters the chambers was also found to be small. Thus, the cryo-separator was left out of the design. Unfortunately, the permeation rates turned out to be higher than expected. However, the chamber gas is slowly lost due to a small leak in the gas system. This leak comes primarily from the gas drawn into the QMS for analysis. Because of this, the N_2 and Ar levels reach an equilibrium of approximately 0.5% as shown on fig. 5.33. This value, while higher than desired, remains steady within 0.1% and therefore does not cause fluctuations in the gain greater than 1%. Thus, overall the purification of the system gas meets the gain stability requirement.

5.7 Slow Control System

The gas system is quite complicated, and it is designed to run without an expert on site. Although the bubblers can protect the chambers from extreme over or underpressure, activation of the bubblers can cost a lot in time and money. If air is drawn into the detectors to correct a large underpressure, the gas becomes strongly contaminated and the N_2 can't be removed using the present purification units. Thus, the system must be highly reliable and able to react to any deviations from normal operation before a larger problem can occur. For these reasons, an industrial programmable logic control (PLC) system was purchased from the Allen Bradley company to provide the slow control for the entire gas system.

The PLC is the heart of the Allen Bradley system. It processes the data and provides instruction to the output modules. It is designed to operate independently and without interface from the user or an external computer. Because the constant operation of the gas system is very important in order to protect the detectors and prevent serious delay, the system is connected to the emergency power supply in the experimental hall.

Virtually all components of the gas system are connected to the PLC. The status of various components are read into the PLC through analog and digital input modules. These data are used in the control program which evaluates the status of the system and can make changes where appropriate. Signals for controlling system components are then sent through digital or analog output modules.

The readings from the analog input come from items such as flow meters, pressure transducers, and the mass spectrometer. The values sent to the analog input are not the actual readings. They are DC voltages which are based on the value as a fraction of the full scale reading of the unit. The actual reading is then calculated in the program. For example, the mass flow controllers have a 0-5 V input/output. If a 2.5 V signal were sent to the PLC, it would indicate a flow of one half of its maximum. The principle is the same with the analog output.

The programming language used by the PLC is called *ladder logic*. In this type of program, the PLC runs through a continuous cycle. It reads all the input registers, executes the program sequences, then sends signals to the output registers. The system operates with a frequency of several cycles per second. The name 'ladder logic' comes from the ladder-like appearance of the program structure. A sample is shown in fig. 5.34. Each line, or rung, of the program represents a boolean condition. If the condition on the left side of the rung is true, the program will execute the instructions on the right side of the rung and the drop to the next one.

The PID controllers run independently of the PLC. They provide the fast response and control of the pressure in the chambers. The purpose of the PLC is to coordinate the functioning of all the equipment so that the system operates smoothly and efficiently.

Included in the programming are a number of software interlocks which protect the system and the detectors from erroneous conditions. For example, if the pressure in a single chamber exceeds a given threshold, that chamber will be isolated from the system by closing valves at the input and return of the module. An alarm will also be activated to indicate that the operator must take steps to rectify the situation. Another example is that when the mass spectrometer is measuring other samples, such as a calibration gas, it cannot be set into the main gas loop, thus preventing other gases from entering the system. The goal of the interlocks is both to prevent an operator mistake from upsetting the system, and to allow the system to operate without an expert present to monitor it.

Computers can be added to the Allen Bradley system in order to communicate with the PLC. They are required in order to view and change the status of the system and to program the ladder logic. However, the PLC is designed to operate independently of any external computers. The software communicates any user input to the PLC where it is interpreted in the next ladder logic cycle. This includes changing flow rates, adjusting the gas mixture, toggling the position of valves, etc. Graphical user interfaces have been written to provide an efficient way to monitor and adjust the conditions of the system. A sample screen is shown in fig. 5.35.

```
                                            Tue Aug 2, 1994   Page 56
Program Listing Report          PLC-5/20    File GASPLC            Rung 5:0

Rung 5:0
connects qms to the chamber gas
| I:032 I:032 I:032                                                 O:032  |
+--] [---]/[---]/[-------------------------------------------------+-(L)-+-+
|    03    04    05                                                |   11| |
|                                                                  |O:032| |
|                                                                  +-(L)-+ |
|                                                                  |   12| |
|                                                                  |O:032| |
|                                                                  +-(L)-+ |
|                                                                      13  |
Rung 5:1
turns the membrane gas separator on/off
| I:032                                                             O:032  |
+--] [---------------------------------------------------------------+-(L)-+-+
|    02                                                            |   14| |
|                                                                  |O:032| |
|                                                                  +-(L)-+ |
|                                                                  |   15| |
|                                                                  |O:032| |
|                                                                  +-(L)-+ |
|                                                                  |   16| |
|                                                                  |O:032| |
|                                                                  +-(L)-+ |
|                                                                      17  |
Rung 5:2
| I:032 I:032 I:032 I:032                                           O:033  |
+--] [---] [---]/[---]/[-------------------------------------------+-(L)-+-+
|    02    04    03    05                                          |   00| |
|                                                                  |O:033| |
|                                                                  +-(L)-+ |
|                                                                  |   01| |
|                                                                  |O:033| |
|                                                                  +-(L)-+ |
|                                                                      02  |
Rung 5:3
| I:032 I:032 I:032                                                 O:033  |
+--] [---]/[---]/[-------------------------------------------------+-(L)-+-+
|    05    03    04                                                |   05| |
|                                                                  |O:033| |
|                                                                  +-(L)-+ |
|                                                                  |   06| |
|                                                                  |O:033| |
|                                                                  +-(L)-+ |
|                                                                      07  |
Rung 5:4
| I:032                                                             O:032  |
+--]/[-------------------------------------------------------------+-(U)-+-+
|    03                                                            |   11| |
|                                                                  |O:032| |
|                                                                  +-(U)-+ |
|                                                                  |   12| |
|                                                                  |O:032| |
|                                                                  +-(U)-+ |
|                                                                      13  |
```

Figure 5.34: A portion of the ladder logic program.

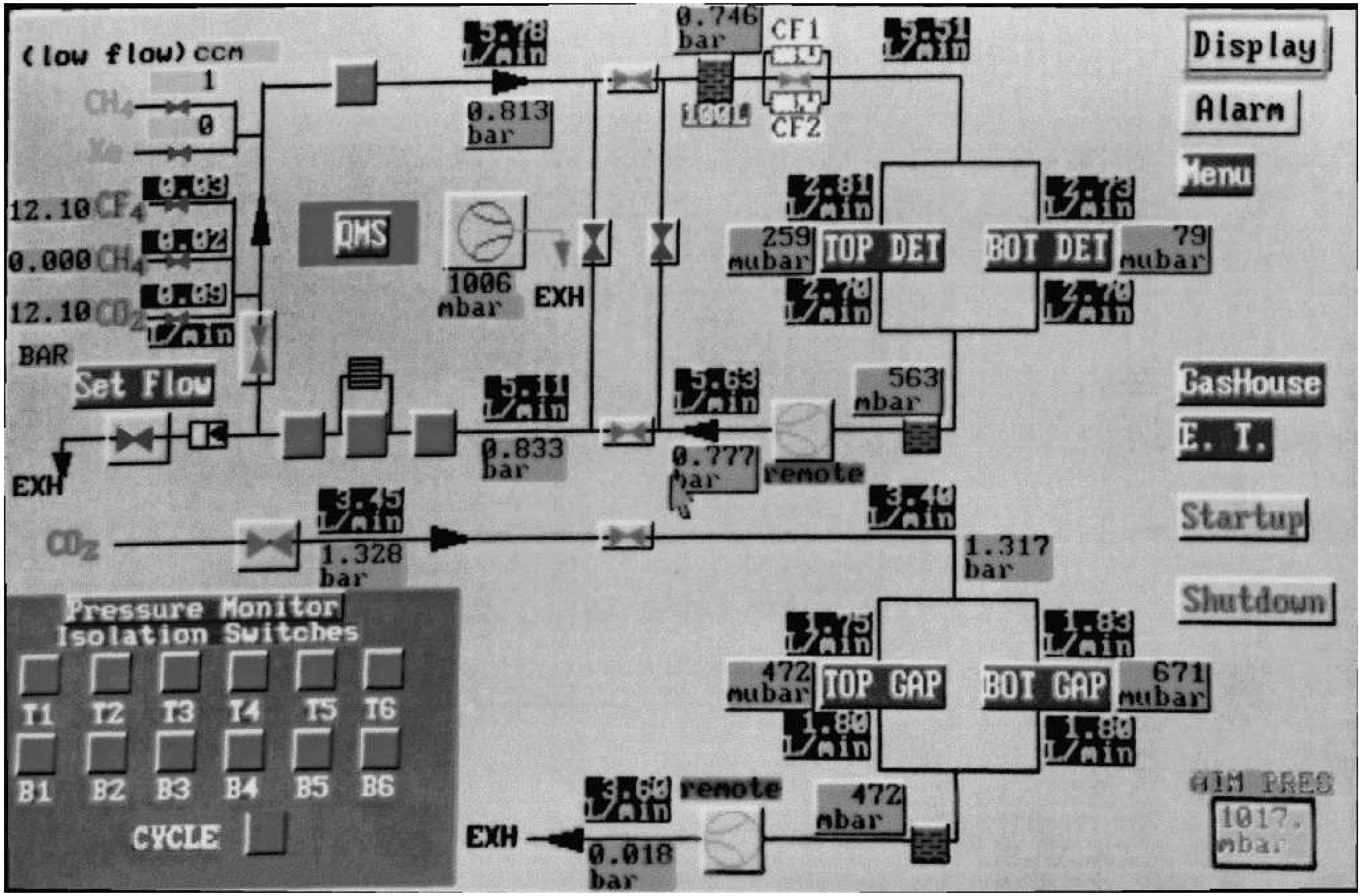

Figure 5.35: The main control screen of the gas system GUI. The values are the current readings of pressure and flow around the system.

The PLC and the associated input/output modules are located in the racks on the electronics trailer. The main computer is in the terminal room in the gas house. There is also a computer at the electronics trailer which performs the same functions.

The computer also enables the data to be saved to disk. The data logger routine allows the user to select certain values to be saved at regular intervals. Several of these routines can be operating simultaneously. This allows the user to select a smaller set of values to be saved frequently while other values which change slowly can be logged over longer periods. The problem which was evident in fig. 5.8 is related to this logging routine. The pressure measurement changed modules every 10 seconds, and the data logger saved these readings every two minutes. Thus, it should save the values at exactly the same point in the cycle. However, given that the timing of the measurements is controlled by the PLC and the timing of the data logger is controlled by the computer, there could be a small discrepancy in the frequencies.

The PLC also has a coprocessor which is used to link the gas system with the HERMES slow control system. Data from the PLC are sent to the coprocessor and uploaded through ethernet to the HERMES network. The HERMES slow control program does not have capabilities to change the gas system; it can only monitor. However, this connection allows the gas system data to be saved to tape along with the slow control data from other aspects of the TRD such as the voltage and temperature.

5.8 Other Considerations

5.8.1 Valves

The route the gas takes through the gas system is controlled by an extensive array of valves; most of which are solenoid valves which can be activated electronically. This allows them to be set by the control system. For example, a valve has been placed at the output of any mass flow controller to prevent any spurious flow through the controller when it is shut off. Also, the position of the QMS can be changed with the touch of a button.

There are sets of valves which can isolate or bypass various parts of the system. Valves at the input to each module allow any individual gas volume to be isolated from the pressure control while the other chambers remain in the system. The gas house and the electronics trailer can be separated from each other and independent recirculation loops can be established on both parts of the system. The gas system can operate with the gas house out of the loop; however, this removes the QMS and the gas supply from the system.

There are also manual valves at key places in the system. They are located at the input to each half of the TRD and after the 12 return lines are recombined in both the detector and gap systems. This allows for a complete isolation of the modules which cannot be changed by the computer. There are valves at the input and output of the electronics trailer to completely isolate it from the gas house. The QMS can also be shut out of the system manually.

Depending on the orientation of the solenoid, the state of the valve when the power is off can be either open or closed. All solenoid valves in the system have been selected such that in the event of a power shutdown, the valves will be in the safest position for the detector. This also means that under normal operating conditions, most valves will not be drawing power. The manual valves remain open during normal operation.

5.8.2 Turbulent Flow

An experiment was conducted at TRIUMF to determine the proper configuration of the gas inlet and outlet in each module. There were two main objectives for the experiment. The first was to determine whether the flow pattern in the module would effectively circulate fresh gas to all regions. If turbulence within the module caused nodes to form in certain areas, there could be regions where impurities diffusing through the foils build up to unacceptable levels. The second objective was to determine the configuration needed during a change to a different type of gas. Given the density of Xe, it should logically be input at the bottom of the chamber and the CO_2 removed from the top. It was unclear whether this same configuration would effectively work for the inverse operation, replacing Xe with CO_2, or whether the CO_2 would rise too quickly to the top of the chamber where it would be exhausted, leaving a layer of Xe/CH_4 on the bottom of the chamber. This operation is required during a shutdown of HERMES for safety reasons due to the flammability of Xe/CH_4.

A roughly 1/6 model of the chamber was built using the same 4:1 ratio of width to height with the sides being approximately 16 cm x 64 cm. The thickness of the model was not considered to be critical. The pipe fittings on the full-scale chambers are located on the top. In order to input the gas at the bottom of the chamber, a pipe runs down the side of the interior of the chamber. This same design was used in the model. The model was built using two large sheets of plexiglass separated by 1.9 cm square plexiglass rods. The system was sealed using a silicone sealant.

In order to see the flow patterns, smoke was added to the input gas. This was done using a small tube of crystals which absorb water from the air and form a sulphuric acid smoke. This type of product is used to test the patterns of airflow in a clean room or from an air conditioning unit. Gas was flowed into the chamber at a constant rate between 10–40 ccm. After a period of one or two hours the flow patterns were examined. The assumption was that if any stable patterns would form, they would be visible after a couple of hours. Watching the flow of smoke through the model showed that there didn't seem to be any nodes forming. The air seemed to be mixing well throughout the chamber. Surprisingly, the flow at the centre of the chamber was non-uniform across its thickness; the air appeared to have different flow directions over the 1.9 cm thickness of the model. The conclusion of this part of the study was that there should be no problems with mixing gas. New gas should reach all parts of the chamber, and any impurities from diffusion through the foils should be flushed out.

The second part of the test consisted of using a mass flow controller on both the input and output lines of the model. The smoke was not used for these studies. The measurements utilized the properties of the readout of a mass flow meter. These readings differ with different gases; for example, while N_2 flowing at 100 ccm will read

100 ccm, Xe flowing at the same rate will read 73 ccm. A number of properties such as viscosity and heat capacity contribute to the differences in reading for different gases. In order to compensate for this, tables of 'gas factors' are provided with the unit. By multiplying the reading by the appropriate gas factor, a proper reading of the flow can be obtained. The readout unit can be calibrated with the gas factor for any particular gas such that the value of the reading is the actual flow rate. When using a mixture of gases, the gas factors are added inversely:[47]

$$\frac{1}{F_{tot}} = \frac{\%A}{F_A} + \frac{\%B}{F_B} \tag{5.16}$$

For the test, gas was flowed into the model at a constant rate between 15–50 ccm, and the uncorrected output flow reading was recorded. Knowing that the output flow should be the same as the input, and using the gas factors, the composition of the output gas could be determined. This method works when switching from one pure gas to another where an exact solution can be found to the equations.

As a dense gas, CF_4 was chosen, and He or N_2 was used for a lighter gas. It was assumed that if a heavy gas was input at the bottom of the chamber and removed at the top, there would be no problem in the filling. The heavy gas would build up from the bottom and push out the lighter gas as the level rose. It was hoped that the same configuration would allow a light gas to push out a heavy one. The test was to determine if there was enough turbulent mixing of the gases that all of the original heavy gas would exit the chamber. The results of the study are shown in fig. 5.36

Integrating the output flow of CF_4 shows the amount that was removed from the chamber during the 2-3 hour test period. These results are summarized in table 5.8. Given that the volume of the model was approximately 2 L, the results show that except at low flow, the gas was fully changed. From these results, it was concluded that Xe could be both filled and removed without having to change the position of the input and output of the gas. These results were later confirmed on the real chambers.

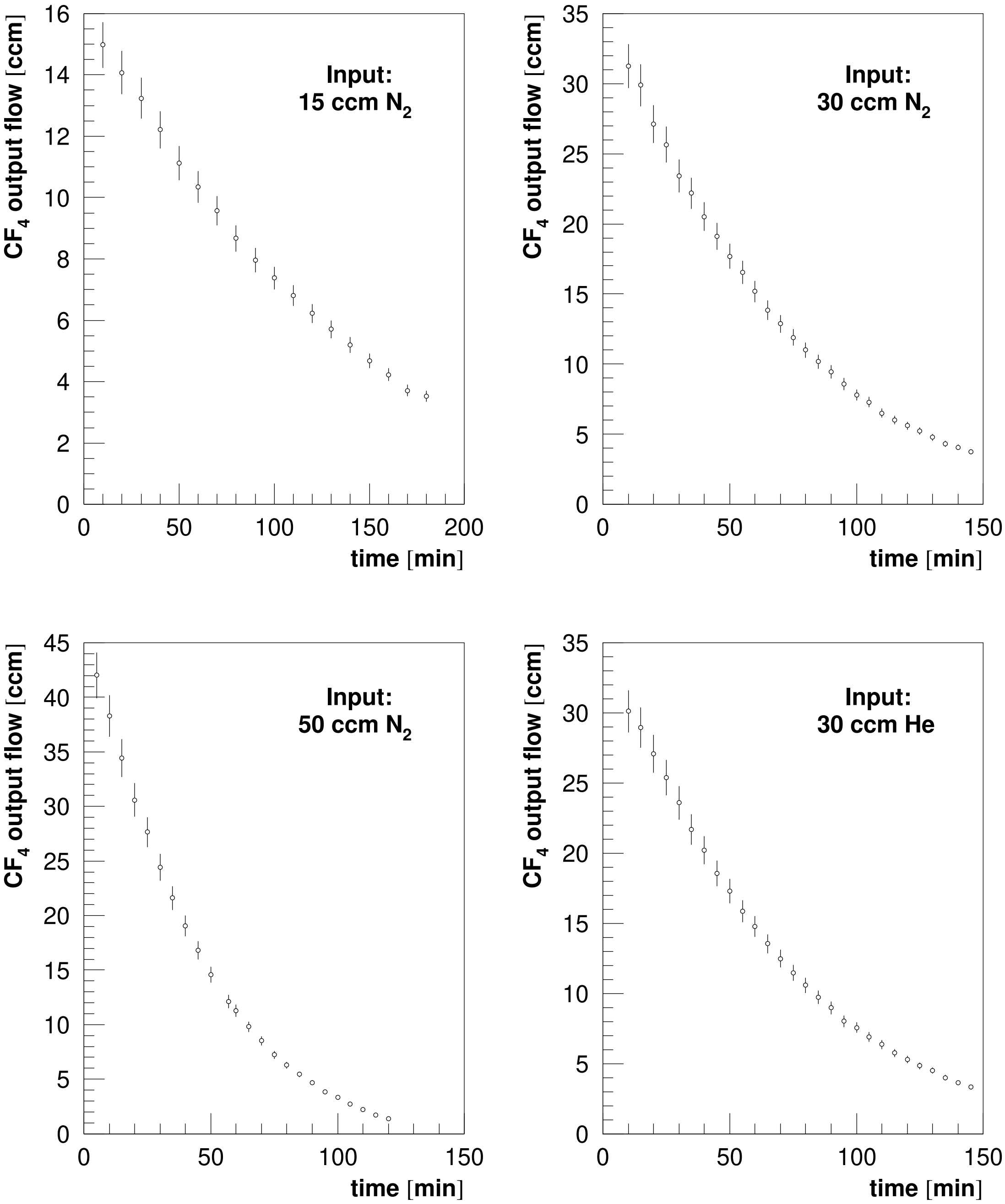

Figure 5.36: Output flow rates of CF_4 from the model when lighter gases are input at various flows.

Table 5.8: Total amount of CF_4 flushed out using a less dense gas.

gas	flow rate (ccm)	output of CF_4 (mL)
N_2	15	1290
N_2	30	1790
N_2	50	2050
He	30	1950

5.8.3 Flammable Gas Safety

The mixture Xe/CH_4 90/10% is regarded as a flammable gas. Therefore, it is necessary to take precautions in the event that there is a major gas leak. The facts that Xe is a dense gas and that the mixture does not separate are utilized in keeping the gas contained. All racks and gas lines containing the gas mixture are surrounded by 30 cm tall walls. Gas leaking from a pipe will fall and be held within these walls. Located within the containment tub are gas sniffers. These will activate a warning alarm if a low level of the gas is detected. In the cases where there is a large leak of gas detected, the general building evacuation alarm will be sounded. Fresh air is pumped into the tubs to dilute the gas to a level where it is non-flammable. The rooms in the gas house which contain flammable gases both in pure and mixed form are extensively grounded. Also, in the case of a gas alarm, the power in the gas house is shut off. This is to prevent any electrical sparks from igniting the gas. The power supplies to the gas system and the PLC on the electronics trailer remain powered in order to keep the gas system operational.

5.9 Gas Recovery

During the HERA beam shutdown in the winter, it is no longer necessary to have the Xe/CH_4 mixture in the gas system. In fact, its removal is necessary because safety regulations prevent any major work to be done around the detectors when they contain flammable gas. However, the Xe is too expensive to simply exhaust, so it is recovered. An extra compression pump is located in the gas house which pumps the gas into storage tanks at a pressure of about 7 bar. This process is done in two main steps.

First, the chambers are isolated from the rest of the system. The gas in the main buffer and the lines is pumped into the storage tanks. This gas is pure Xe/CH_4 and as much as possible is recovered by evacuating the lines. Given that the pump is a compression pump which is not designed to produce a high vacuum, it begins to draw in traces of air when the absolute pressure reaches approximately 0.2 bar. This problem was anticipated, and an oxygen analyzer was placed at the input to the storage tank. When the O_2 level begins to rise, the tank is closed.

At this point, the supply lines are restored to normal pressure with CO_2. Once the supply lines have reached the operating pressure, the chambers are reintegrated into the system. The gas flowing out of the chambers is pumped into the storage tank. The pressure inside the chambers is maintained by flowing in CO_2 which produces a gradual contamination of the stored gas. In order to reduce this, the gas flows through the membrane separator before entering the tank. Using this method, approximately 60% of the Xe/CH_4 is recovered and the maximum contamination is held to about 15%. The gas mixture left in the system contains about 30% xenon which allows the system to operate under non-flammable conditions during the beam shutdown period.

The storage tanks are directly connected to the main gas supply lines in the gas house. This allows the gas from the storage bottles to be returned to the system using the same method as the pure gas. The only difference being that the gas mixing routine would not be required. The CO_2 in the system and in the storage tanks is readily removed using the membrane separator.

5.10 TRD Results

The requirements of 1% gain stability in the different aspects of the gas control is to limit the total gain fluctuation. Corrections can be made in the analysis of the data to produce the desired pion rejection factor as long as the net fluctuation is fairly small. Fig. 5.37 shows the gain of the HERMES TRD for different data taking runs. The total fluctuation is approximately 10%. This is sufficiently low that the 100:1 pion rejection is achieved using software corrections. In fact, as can be seen in fig. 5.38,[45] the performance of the TRD exceeds its goal, and the average PRF integrated over all momenta is 127.8 ± 3.4.

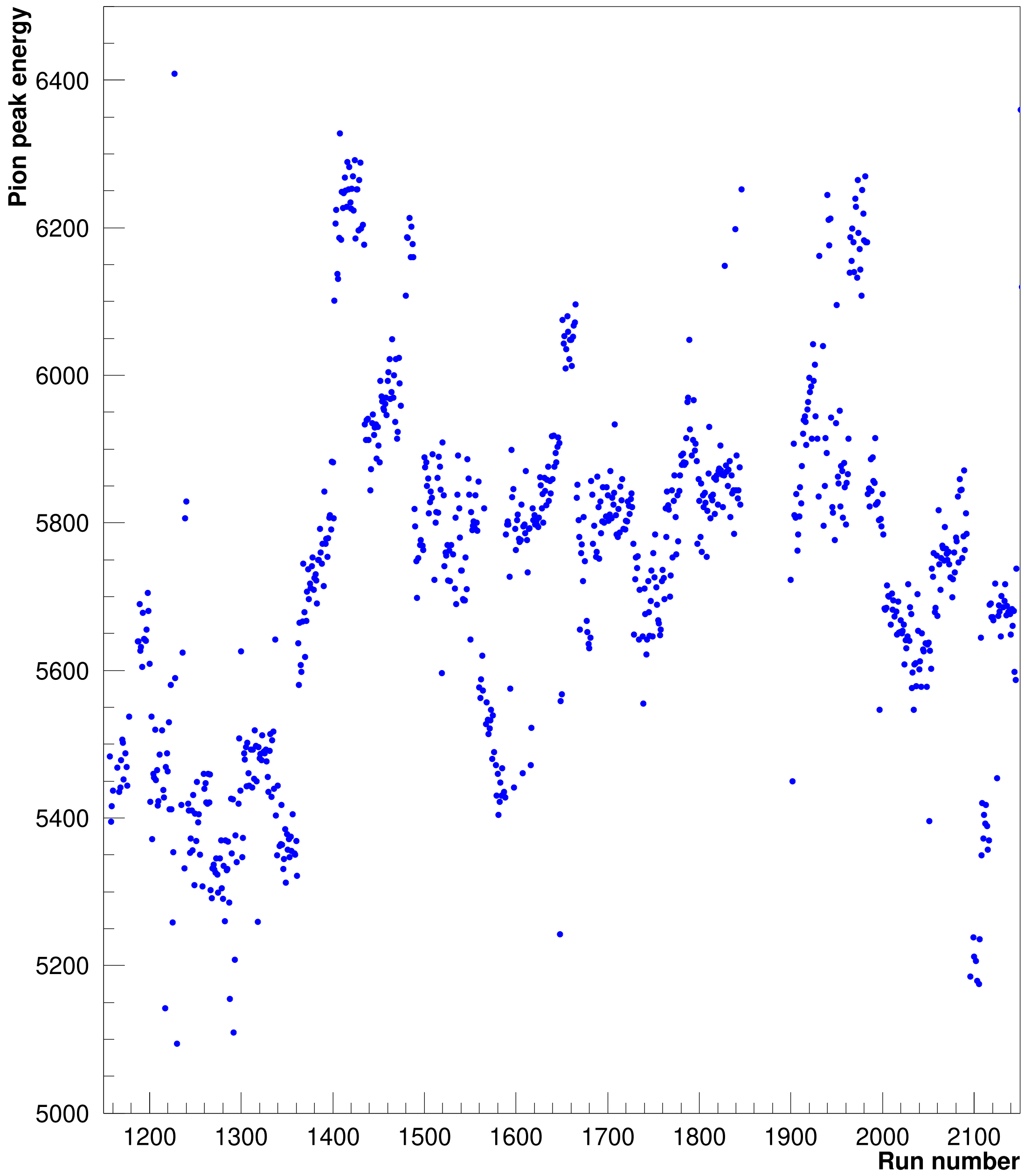

Figure 5.37: Gain fluctuations in the HERMES TRD. The value of the gain is determined by the energy deposited in the pion dE/dx peak. These data are taken from the TRD analysis for different data taking runs. Only runs for which software corrections have been applied are included here.

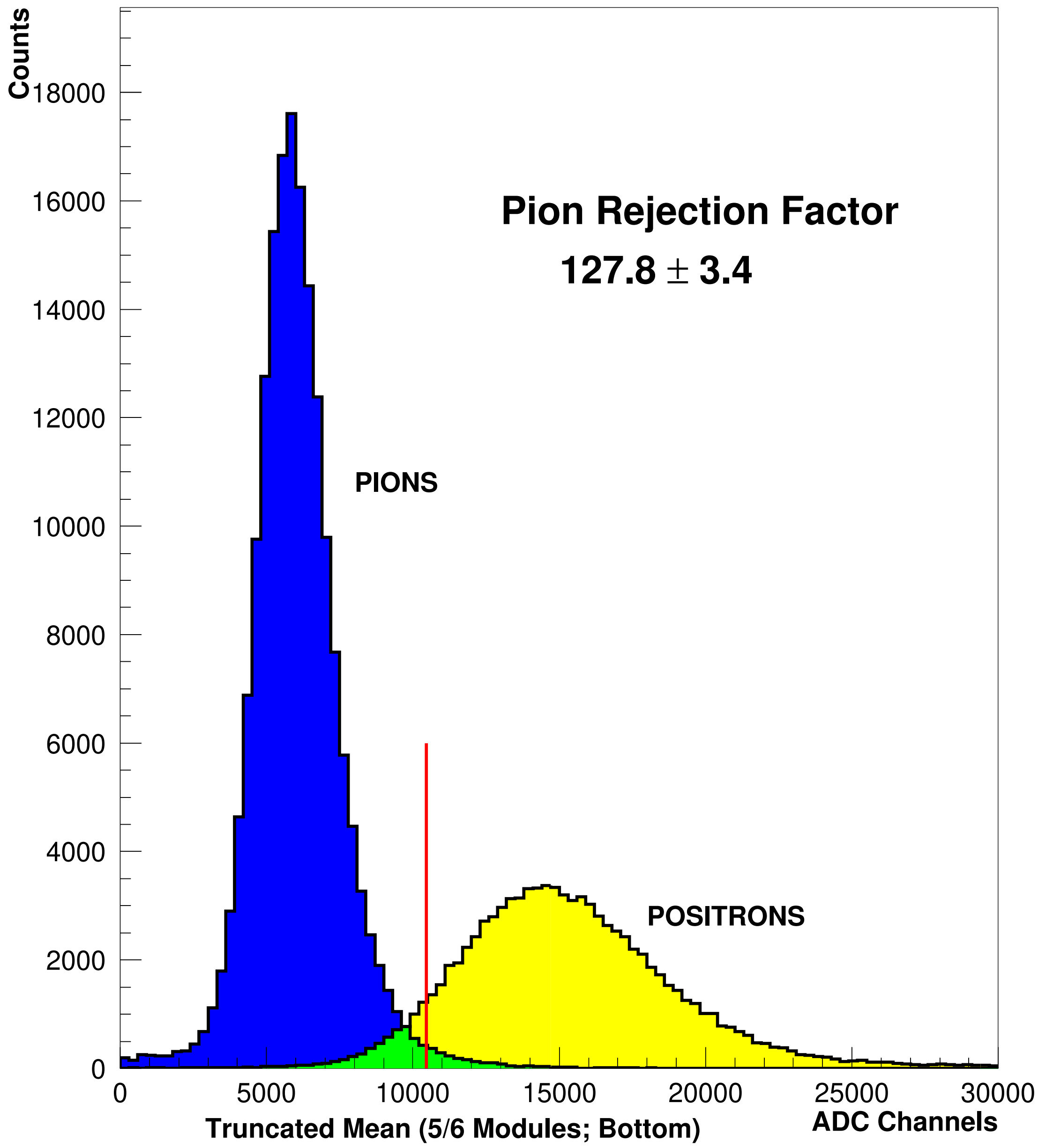

Figure 5.38: The average pion rejection factor of the HERMES TRD.[45] The vertical line indicates the position of the cut.

Chapter 6

Conclusion

The objective of the HERMES experiment is to provide a detailed study of the spin structure of the nucleon. It began data taking in August 1995, and will produce accurate measurements of $g_{1,2}$ for both the neutron and the proton. Also, HERMES is the only current experiment which measures the semi-inclusive hadron asymmetry in coincidence with the scattered positron. This is possible because of the extensive particle identification and the large acceptance of the HERMES spectrometer. Semi-inclusive measurements provide a decomposition of the spin structure into valence and sea quark components.

The transition radiation detector is an important component of the particle identification. It distinguishes between positrons and hadrons by detecting an X-ray in coincidence with the positrons. The method used to distinguish between the radiating and non-radiating particles is to apply a cut on the energy deposited in the detector. In order to obtain the required 100:1 pion rejection using this method, the gain of the TRD must remain constant to high accuracy.

Many factors can affect the gain of the detector, and these must be controlled as much as possible. In particular, the distance between the cathode foils must be controlled to within 10 μm to keep the gain fluctuation below 1%. This requires that the differential pressure across the cathode foils be constant to one part in 10^5. Also, the gain can be affected at the 1% level by changes in the Xe/CH_4 ratio or impurity levels as small as 0.2%. Thus, the accurate control of the gas in the detector is critical in maintaining a constant gain.

A sophisticated gas system for the HERMES TRD was designed and built at TRIUMF. The design of the TRD calls for two stacks of six modules, one above and one below the beamline. Each module must be supplied with an identical mixture of Xe/CH_4 and have very accurate pressure control. Because of the expense of using Xe, the gas must be recycled. Therefore, purification is necessary to prevent build-up of contaminants in the gas.

The differential pressure control is provided by PID controllers. They provide the fast and accurate control required to maintain the differential pressure stable to better than 10 μbar. They can track the atmospheric pressure accurately even though the fluctuations are 4 orders of magnitude larger. Even during periods of high atmospheric activity, the differential pressure across the cathode foils has remained accurate even to ± 3 μbar.

The gas concentrations are measured by a quadrupole mass spectrometer. The ratio of Xe to CH_4 needs to remain constant at 90:10 to within $\pm 0.15\%$. While the QMS indicated that the CH_4 concentration fluctuated between 9 - 12%, there is an ambient temperature dependence which reduces the confidence in these readings. It would appear from the data that the concentration remains fairly steady but doesn't reach the 1% gain stability level. However, due to the decreased confidence in the QMS readings, the actual level of fluctuation is uncertain.

Flush gaps surrounding the chamber significantly reduce the amount of air which diffuses through the foils into the system. Impurities in the chamber gas are removed by molecular sieves which are very effective at removing H_2O, O_2, and CO_2. The concentration of O_2 is held below 100 ppm, and the CO_2 level is kept at 0.2 $\pm 0.2\%$. The sieves do not remove N_2 or Ar, but since these impurities build up very slowly, no means for removing them has been utilized. They build up to about 0.5% before the small amount gas leakage produces an equilibrium level. While these impurity levels exceed the goal of less than 0.1%, they remain constant to ±0.1%. Thus, the impurity levels meet the 1% gain stability requirement.

The procedure for initially changing the gas in the system from CO_2 to Xe/CH_4 was successful. The CO_2 can be removed to a level of a few percent using a membrane gas separator while the system is in a recirculation loop. The CO_2 is then reduced to less than 0.5% using the molecular sieves.

The strict requirements on gain stability in the gas system have enabled the detector to achieve to desired pion rejection factor of 100:1 for 90% electron efficiency. While it is not necessary for the gain to be stable at the 1% level, this condition is applied to the different aspects of the gas system so that the total variation is small. The total gain variation is approximately 10%, and the momentum integrated pion rejection factor for the HERMES TRD is 127.8 ± 3.4.

Appendix A

Definition of Symbols

The following is a list of the abbreviations for the parts in the schematic diagrams of the gas system shown in figs. 5.6 and 5.7.

BB	Glass bubbler
BU	Buffer volume
BP	Bellows pump
CF	Chemical filter (sieve)
DP	Diaphram pump
FC	Mass flow controller
FL	Particle filter
FM	Mass flow meter
FR	Flow Rotameter
MS	Membrane separator
PA	Absolute pressure transducer

PD	Differential pressure transducer
PR	Mechanical pressure regulator
QM	Quadrupole mass spectrometer
RP	Rotary pump (vacuum)
SM	Static mixer
ST	Storage tank
VA	Automatic (solenoid) valve
VC	Check valve
VN	Needle valve
VM	Manual valve

Appendix B

Contribution to HERMES

Because of the large size of high energy physics collaborations, it is often difficult to distinguish the contributions of an individual to the total project. For this reason, I am including a description of the work to which I personally contributed.

I joined HERMES in Sept. 1993 when I worked on the construction of the TRD gas system until its completion in the summer of 1994. I was also taking courses concurrently with this work. The task I was given in the fall of 1993 was to test the flow of gases in a model chamber as described in section 5.8.2. The quadrupole mass spectrometer arrived in early 1994, and my work was focussed on its use to run tests on the purification equipment. Because of this work, I became the local expert on the QMS.

The construction of the gas system was completed in the summer. I helped with the He leak testing. The entire gas system was shipped to DESY in Sept. '94 along with 6 of the detector modules. After this I helped with the construction of the remaining detector modules which were shipped to DESY in November.

I went to DESY three times during my work on the gas system. The first trip was in September '94 for one week during a HERMES collaboration meeting in order to learn more about the HERMES physics program. The next trip was Jan/Feb. '95 for eight weeks. The TRD and gas system were installed and the plumbing between them was almost complete at this time. I spent this period on the commissioning of the gas system. Much of this time was spent working on the mass spectrometer. I worked on the calibration of the QMS and on the program which sent the concentration data to the Allen Bradley system. I returned to DESY in March to collect data from the gas filling procedure. During this time I also worked on enabling the HERMES slow control system to read the gas system parameters from the PLC coprocessor.

Bibliography

[1] E. Rutherford, Phil. Mag. **21** (1911) 669.

[2] SLAC-MIT: M. Briedenbach *et al.*, Phys. Rev. Lett. **23** (1969) 935,
SLAC-MIT: E.D. Bloom *et al.*, Phys. Rev. **33** (1974) 1406.

[3] M. Gell-Mann, Phys. Lett. **8** (1964) 214,
G. Zweig, CERN report TH401, TH412 (1964).

[4] EMC: J. Ashman *et al.*, Nuclear Phys. **B328** (1989) 1

[5] SMC: B. Adeva *et al.*, Phys. Lett. **B302** (1993) 533

[6] E142 Collaboration: P.L. Anthony *et al.*, Phys. Rev. Lett. **71** (1993) 959

[7] E143 Collaboration: K. Abe *et al.*, Phys. Rev. Lett. **74** (1995) 346

[8] HERMES Collaboration, *Technical Design Report*, DESY-PRC 93/06 (1993)

[9] F. Halzen and A. Martin, *Quarks and Leptons*, John Wiley & Sons, 1984

[10] M. Vetterli, *Deep Inelastic Lepton Scattering*
Lecture notes, TRIUMF Summer Institute, 1993 (unpublished)

[11] L. Klostermann, *The Spin Dependent Structure Function g_1 of the Deuteron and the Proton*, PhD thesis, Technical University Delft, Netherlands. 1995

[12] E.Hughes, *Polarized Lepton-Nucleon Scattering* SLAC-PUB-6439 (1994).

[13] D.H. Perkins, *Introduction to High Energy Physics*, Addison-Wesley, 1987

[14] NMC: P. Amadruz *et al.*, Phys. Lett. **B295** (1992) 159.

[15] W. Wandzura and F. Wilczek, Phys. Lett. **B172** (1977) 195;
E.V. Shuriak and A.F. Vainshtein, Nucl. Phys. **B201** (1982) 142

[16] J.D. Bjorken, Phys. Rev. **148** (1966) 1457

[17] J. Ellis and R. Jaffee, Phys. Rev. **D9** (1974) 1444

[18] H. Ebenhoh *et al.*, Z. Physik **241** (1971) 473

[19] E80 Collaboration: M.J. Algurd *et al.*,
Phys. Rev. Lett. **37** (1976) 1261; **41** (1978) 70
E130 Collaboration: G. Baum *et al.*, Phys. Rev. Lett. **51** (1983) 1135
SLAC-Yale Collaboration: G. Baum *et al.*, Phys. Rev. Lett. **45** (1980) 2000

[20] SMC: D. Adams *et al.*, Phys. Lett. **B329** (1994) 399

[21] E143 Collaboration: K. Abe *et al.*, Phys. Rev. Lett. **75** (1995) 25

[22] R.L. Jaffe and A. Manohar, Phys. Lett. **B223** (1989) 218

[23] P. Hoodbhoy, R.L. Jaffe and A. Manohar, Nucl. Phys. **B312** (1989) 571;
R.L. Jaffe and A. Manohar, Nucl. Phys. **B321** (1989) 343

[24] H. Burkhardt and W.N. Cottingham, Ann. Phys. (NY) **56** (1976) 453

[25] J.P. Albenese *et al.*, Phys. Lett. **B144** (1984) 302

[26] L.L. Frankfurt, Phys. Lett. **B230** (1989) 141

[27] F.E. Close and R.G. Milner, Phys. Rev. **D44** (1991) 3691

[28] M. Düren, *The HERMES Experiment: From the Design to the First Results*, DESY HERMES-95-02 (1995)

[29] H.E. Jackson, *Sea-Quark Flavour Asymmetry in HERMES*, Argonne National Lab., PHY-7076-ME-92 (1992)

[30] E.L. Berger *Semi-Inclusive Inelastic Electron Scattering From Nuclei*, ANL-HEP-PR-87-45 (1987)

[31] V.L. Ginzberg and I.M. Franck, Soviet Phys. JETP **16** (1946) 15

[32] J. Doostens *et al.*, Phys. Rev. Lett. **19** (1967) 541
S. Prunster *et al.*, Phys. Lett. **B18** (1968) 47

[33] G.M. Garibian, Zh. Eksp. Teor. Fiz. **33** (1957) 1043
[Sov. Phys. JETP **6** (1958) 1079]
G.M. Garibian, Zh. Eksp. Teor. Fiz. **37** (1959) 527
[Sov. Phys. JETP **10** (1960) 372]

[34] F. Harris *et al.*, Nuc. Inst. and Meth. **107** (1973) 413
M.L. Cherry, D. Müller, and T.A. Prince, Nuc. Inst. and Meth. **115** (1974) 141

[35] J.D. Jackson, *Classical Electrodynamics* 2nd Ed. John Wiley & Sons, 1975

[36] B. Dolgoshein, Nuc. Inst. Meth. **A326** (1993) 434

[37] X. Artru, G.B. Yodh and G. Mennessier, Phys. Rev. **D12** (1975) 1289

[38] M. Vetterli, *Transition Radiation Detectors*
Lecture notes, TRIUMF Summer Institute, 1995 (unpublished)

[39] F. Sauli, *Principles of Operation of Multiwire Proportional and Drift Chambers*, CERN 77-09 (1977)

[40] G. Charpak *et al.*, Nucl. Inst. and Meth. **62** (1968) 235.

[41] J. Emerson, *Modelling of the HERMES Transition Radiation Detector*
M.Sc. Thesis, SFU. 1995

[42] J.F. Detoeuf *et.al.*, Nucl. Inst. and Meth. **A265** (1988) 157.

[43] M. Weissbluth, *Atoms and Molecules*, Academic Press, 1978

[44] C.A. Miller, private communication

[45] R. Kaiser, presented to Western Regional Nuclear & Particle Physics Conference, Lake Louise (1996) unpublished.

[46] TRIUMF gas properties tests, to be published

[47] R. Openshaw, private communication

[48] C.L. Phillips and R.D. Harbour, *Feedback Control Systems*, Prentice Hall, 1988

[49] *Partialdruckmessung in der Vakuumtechnik*, Balzers Spectrometer Manual

[50] F.H. Field and J.L. Franklin, *Electron Impact Phenomena* Academic Press, 1957

[51] *Molecular Sieve Safety Bulletin for Processors*, Union Carbide.

[52] M.J. Kueckes, private communication

[53] TRD ZEUS Group, V. Beitzel *et al.*, Nuc. Inst. and Meth. **A323** (1992) 135.

[54] D.R. Lide ed., *Handbook of Chemistry and Physics*, vol. 74, CRC Press, (1993)